DIPARTIMENTO DI ASTRONOMIA
E SCIENZA DELLO SPAZIO
UNIVERSITÀ DEGLI STUDI DI FIRENZE

Ph. D. Course in Astronomy
VIII cycle: 1992 – 1995

RADIO EMISSION FROM BINARY SYSTEMS IN ACTIVE AND QUIESCENT PHASES

Elena Franciosini

Supervisor: Prof. Franca Chiuderi Drago

INDEX

INTRODUCTION

In the past twenty years several classes of stars of late spectral type have been discovered as sources of radio emission; among them, those showing the stronger emission, and that have therefore been studied more extensively, are the classes of the RS CVn and Algol-type systems, so called from the names of their prototypes. These systems are close binaries with orbital periods of a few days showing a strong activity over the whole spectrum, from X-rays to radio wavelenghts, which is very similar to the solar case (spots, chromospheric active regions, X-ray and radio emitting coronae, flares) but on much greater scales. The origin of this high degree of activity, generally associated with the cooler, more evolved star, is attributed to the presence of strong magnetic fields, generated by the dynamo mechanism which is very efficient in these systems due to the presence of deep convection zones and to the rapid rotation induced by tidal forces, that tend to syncronize the rotational and orbital periods of the stars.

The radio emission of these systems is highly variable, and is characterized by low-activity (quiescent) periods, with flux densities of a few mJy, and by flares with typical flux densities of $100 - 200$ mJy, rising up to 1 Jy for the most intense events. Although these systems have been extensively studied in the past, until a few years ago the only available data were sporadic observations, generally made at a single frequency, expecially in the case of the quiescent component; in the past few years however many multifrequency observations of both the flux density and polarization have become available, and long-term monitoring programs of these systems have been started, allowing a better understanding of the radio emission properties in the active and quiescent phases.

These properties will be described in Chapt. 1.

The characteristics of the observed radio emission (high brightness temperature and circular polarization) suggest that it is due to gyrosynchrotron emission from a non-thermal distribution of mildly-relativistic electrons; thermal bremsstrahlung from the coronal plasma would give in fact flux densities several orders of magnitude lower than the observed ones. This mechanism is able to successfully reproduce both the flare spectra, assuming an inhomogeneous source, such as a magnetic loop (Klein & Chiuderi Drago 1987), and the quiescent spectra in the assumption of a homogeneous source with a magnetic field ~ 10 G (Chiuderi Drago & Franciosini 1993). The existence of a strong correlation between the radio and X-ray luminosities, recently found also for other types of stars (Güdel & Benz 1993; Benz & Güdel 1994), led some authors to propose an alternative interpretation for the quiescent component, assuming that the emission in both frequency bands is due to the same distribution of thermal particles (Drake et al. 1989, 1992); however, in this hypothesis the magnetic field configuration must be very different from the dipolar field reproducing the flaring emission (Chiuderi Drago & Franciosini 1993). In the non-thermal case, on the contrary, the low values of the magnetic field needed to reproduce the quiescent spectra are compatible with a source located at the loop top, and moreover they are in agreement with the observed lifetime of the quiescent component (Massi & Chiuderi Drago 1992).

Several VLBI observations have shown that, while the emission in active phases arises from a compact component (core) of stellar size, during quiescent phases the emission is associated with an extended halo, with dimensions of the order of the binary separation; sometimes an intermediate structure, where both components are present, is observed (see for example Mutel et al. 1985; Lestrade et al. 1988; Massi et al. 1988). This suggests the idea of a continuous evolution of the radio emission from active to quiescent phases: the quiescent component would be the residual emission from the distribution of electrons that are injected in the source at the flare onset and have then lost their energy due to collisions with thermal electrons and to the emission of synchrotron radiation.

A variation of the emission with time is observed also during the initial phases of flares, when the flux density increases due to the acceleration of new particles in the source. Recent observations made at the Effelsberg radiotelescope allowed to obtain some spectra that are clearly associated with this initial phase (Torricelli Ciamponi et al. 1995); moreover, VLBI observations have shown that also the source structure varies, increasing its dimensions during the rising phase (Trigilio et al. 1995).

At the light of these observations, in this thesis we have developed a quantitative model of the time evolution of the radio emission during the decay and rising phases of flares. In the first case, considered in Chapt. 2, we have computed the emission from a population of electrons that is accelerated in the source at the time $t = 0$ and then undergoes energy losses. The temporal variation of the distribution causes a variation of the spectrum, which changes its shape from a typical flaring spectrum to a typical quiescent one. It will be shown that the predictions of the model are in very good agreement with the observations, in particular it is possible to reproduce the evolution of the source structure from core-halo to halo as the flux density decreases. In Chapt. 3 the initial rising phase of the flare is considered, adding to the equation describing the evolution of the energy distribution a term representing the injection of new energetic particles in the source, and the results are compared with the spectra observed at Effelsberg. The increase in the number of relativistic particles in the loop during this phase makes the emission increase with time, and, as it will be shown, causes an apparent increase of the source size, in agreement with VLBI observations.

Recent observations of some RS CVn and Algol systems, extended over several consecutive orbital periods, have shown that the stellar rotation can modify the observed radiation by inducing a modulation which can be interpreted assuming that the radiation arises in sources located near the stellar equator, that are partly or completely occulted as the star rotates. This modulation is much more evident during periods of strong activity, when the emission comes from compact regions of stellar size near the photosphere. In some cases peaks of emission are observed always at the same orbital phase (Elias et al.

1995; Feldman et al. 1978); Elias et al. (1995) also found a correlation between the maximum radio emission and the minimum in the optical light curve. This suggests that the emission, in analogy with the solar case, comes from small coronal active regions located above the photospheric spots. We have studied the effect of stellar rotation computing the emission from an equatorial dipolar loop anchored on the stellar surface. Two different cases have been considered: in the first case it is assumed that the emission is constant in time, while in the second one we consider the decay of a flaring event occurring in the loop at a given time. The results of the model are discussed and compared with observations in Chapt. 4. The rotation of magnetic loops where flares are taking place is able to reproduce very well the observations, in particular the radio light curve of UX Ari observed by Elias et al. (1995) and the series of outbursts observed on the system HR 1099 in February 1978 (Feldman et al. 1978).

A very important characteristic of the radio emission is the circular polarization, which in the stellar case is nearly the only diagnostic of the magnetic fields present in the coronae of these systems. The principal property of the observed polarization is the reversal of its sense which occurs generally at frequencies between 1.4 and 5 GHz, independently of the spectral shape: it is in fact observed both with positive spectral indexes, characteristic of the flaring emission, and with flat or decreasing spectra during quiescent phases. The current interpretation of the polarization reversal is the transition of the source from optically thin to optically thick, however the gyrosynchrotron models predict that this should happen in a part of the spectrum where the spectral index is positive. The only way to obtain a reversal with flat spectra is to consider ad-hoc models consisting of more components with suitable parameters (Mutel et al. 1987), or it is necessary to assume that the density of relativistic electrons increases strongly with the distance from the star (Morris et al. 1990; Jones et al. 1994). In Chapt. 5 we shall show some observations of a highly variable and polarized emission at 1.4 GHz, which can be attributed to a coherent emission process. This component is polarized in the opposite sense with respect to the high-frequency emission and shows a slow variation on long timescales which, at low signal-to-noise ratios, could be mistaken for incoherent emission, such as

gyrosynchrotron emission. We propose that this coherent component is always present, although not always distinguishable, and that the polarization reversal observed at low frequencies is due to this component and is not a property of gyrosynchrotron emission itself. Moreover, it will be noted that there is a discrepancy between the current gyrosynchrotron models and the polarization trend at high frequencies.

CHAPTER 1

PROPERTIES OF RS CVn AND ALGOL-TYPE BINARY SYSTEMS

§ 1.1 General characteristics of RS CVn systems

Close binary systems of the RS Canum Venaticorum (RS CVn) type, according to the original definition by Hall (1976), are binaries with orbital periods between 1 and 14 days showing, outside eclipse, a strong emission in the CaII H and K lines, much stronger than generally observed in single stars of the same spectral type; the primary component is a main-sequence star or a subgiant (luminosity class V or IV) of spectral type F or G, while the secondary, which is cooler and usually more massive and evolved, is typically a K subgiant (in most cases K0 IV). There are two other related classes, still characterized by the presence of emission in the H and K lines: the short-period RS CVns, with $P_{\rm orb} < 1^{\rm d}$ and a F–G V–IV primary, and the long-period RS CVns, with $P_{\rm orb} > 14^{\rm d}$ and a subgiant or giant component of spectral type G–K. As noted by Linsky (1984), a better subdivision between the two classes of RS CVn and long-period RS CVn stars is given by $P_{\rm orb} = 20^{\rm d}$, since, due to the effect of tidal forces acting reciprocally on the two components, subgiant stars in systems with $P_{\rm orb} < 20^{\rm d}$ rotate synchronously (i.e. with $P_{\rm rot} \simeq P_{\rm orb}$). In long-period binaries on the contrary this synchronization is not present.

In most cases the two stars have nearly the same mass of the order of $1 - 1.5\,M_{\odot}$; evolutionary studies indicate than one or both components have already left the main sequence and have developed convective envelopes (Popper

& Ulrich 1977). Generally these systems are detached, i.e. neither component is sufficiently evolved to fill its Roche lobe; there are however some cases of semidetached systems, such as HR 5110 and RT Lac (Hall 1989; Welty & Ramsey 1995).

The emission in the CaII H and K lines is generally associated with the cooler star, which is the most active of the two components, although also the companion often shows a certain degree of activity, expecially if the two stars have similar spectral types. Besides the CaII lines, these systems show a strong activity over the whole spectrum, from X-rays to radio wavelengths, which is very similar to the solar activity (spots, chromospheric active regions, X-ray and radio emitting coronae, flares), but on much greater scales. This activity is attributed to the presence of strong magnetic fields generated by the dynamo mechanism, due to the interaction of weak pre-existing fields with the convective motions of the outer layers of the star and with differential rotation; since this mechanism depends on the velocity of these motions, it is very efficient in RS CVn systems because these stars rotate very rapidly due to orbital synchronization. This explains also why the cooler star is generally more active: being the more massive one, it is also more evolved, therefore it has a larger radius than the other component and is thus rotating faster.

One of the main characteristics of RS CVn systems is a quasi-sinusoidal modulation of the photometric light curve, with a period similar to the orbital one and amplitude of $0.01 - 0.4$ mag (Catalano 1983; Vogt 1983). In analogy with the solar activity, this distorsion has been interpreted as due to the presence of spots or spot groups obscuring a great part of the visible hemisphere of the star; this assumption can also explain the irregular variations observed in the light curve as changes in the size and position of the spots. Their distribution on the stellar surface has been derived by reproducing the photometric light curves with simplified models (Dorren et al. 1981; Rodonò et al. 1986; Elias et al. 1995), or by analyzing the distorsions induced by the rotation of the spots on the line profiles using the Doppler Imaging method, which allows the calculation of a detailed map of the stellar surface (Vogt & Penrod 1983; Gondoin 1986; Strassmeier et al. 1991; Vogt & Hatzes 1991; Donati et al. 1992). All these

studies indicate the presence of large spots or spot groups, $\sim 500-1300$ K cooler than the photosphere, that cover up to $30-40$ % of the stellar surface and can be present also at high latitudes, contrary to the solar case. In most cases a polar spot is observed, which persists for several years, together with one or more spots at lower latitudes, often near the equator and generally smaller and with a shorter lifetime (of the order of a few months). Photometric observations over several years suggests the possibility of an activity cycle, with periodic variations of the light curve amplitude and therefore of the spotted area, on timescales of the order of $15-20$ years (e.g. Rodonò et al. 1995).

The Doppler Imaging method has been applied also to spectra in the Stokes parameter V, in order to obtain magnetic maps of the stellar surface (Donati et al. 1990, 1992), finding fields of the order of 300 G associated with the polar spot and of $\sim 700-1000$ G near the equator, and covering about 18 % of the stellar surface. These results agree with previous measurements of extended fields of $600-1000$ G, obtained from the study of the Zeeman broadening of spectral lines (Giampapa et al. 1983; Gondoin et al. 1985). Due to the lack of resolution of these methods, these values are in reality underestimated, since they are mean values over the spotted area, and it is possible that the effective magnetic field inside the spot umbra could be higher, of the order of some kG.

RS CVn systems show a strong chromospheric activity indicated by occasional emission in the Hα line (which is always present in the case of the most active systems like HR 1099, UX Ari e II Peg), and by the presence in the ultraviolet spectrum of several emission lines originating in the chromosphere and in the transition region between chromosphere and corona, with fluxes one or two orders of magnitude greater than the typical values for the quiet Sun. The emission increases further during flares, reaching intensities up to 1000 times those observed in the strongest solar flares (Simon et al. 1980). The observations have also evidenced a modulation of the line intensities with the rotational period (Bopp & Talcott 1978; Little-Marenin et al. 1986; Rodonò et al. 1987; Drake et al. 1995), which can be interpreted, in analogy with the solar case, as due to the presence of chromospheric active regions, located on the cool component, that are more or less visible depending on orbital phase. Moreover

in many cases the lines are stronger at the minimum of the photometric light curve (Gondoin 1986; Rodonò et al. 1987; Huenemorder et al. 1990), implying that active regions are located above the spot groups, as on the Sun.

Another important property of RS CVn systems is the presence of strong X-ray emission, with luminosities $L_{\rm X} \sim 10^{29} - 10^{31}$ erg sec^{-1} (about $10^2 - 10^4$ times that of the quiet Sun), indicating the presence of a corona which emits thermically at temperatures of the order of 10^7 K. Besides the quiescent emission, strong long-lasting (several hours or days) flares are observed, with luminosities $L_{\rm X} \sim 10^{32}$ erg sec^{-1} and energies $E_{\rm X} \sim 10^{34} - 10^{37}$ erg, i.e. up to 10^5 times the energy of the strongest solar flares (Pallavicini 1995). Spectroscopic observations performed with the Einstein satellite (Swank et al. 1981) and more recently with ROSAT (Dempsey et al. 1993) have shown that the coronal plasma is composed by at least two components: a "cool" component with temperature $T = 1 - 3 \times 10^6$ K and luminosity of $10^{30} - 10^{31}$ erg sec^{-1}, and a "hot" component with $T = 1 - 4 \times 10^7$ K and luminosity of $2 \times 10^{29} - 7 \times 10^{31}$ erg sec^{-1}. While for the low-temperature component the values are very similar for the entire group of observed systems, those relative to the higher temperature component are more variable from one system to the other; the same is true for the emission measures ($EM = \int n_{\rm e}^2 \, {\rm d}V$), that are of the order of $10^{52} - 10^{53}$ cm^{-3} for the cool component and vary between 2×10^{52} and 3×10^{54} cm^{-3} for the hot component.

The high temperature of the coronal plasma requires a confinement mechanism, since for $T \gtrsim 10^7$ K the gravitational field alone is not able to confine the gas. This mechanism is provided by magnetic fields, that are, as we said before, very strong in these systems and are responsible for the observed activity. In the assumption that the coronal plasma is contained in magnetic loops, as on the Sun, Swank et al. (1981) found that for the cool component the source has stellar dimensions and is probably confined in small loops covering the stellar surface, while the source associated with the hot component is extended over the whole binary system. This situation, which is common to the radio emission as we will see, implies the existence of a very extended magnetosphere in common to both stars. Theoretical calculations, developed assuming that both

components of the system possess a global dipolar magnetic field and that the more active star has bipolar spot groups as on the Sun, show that it is possible to have magnetic loops both anchored on the active star or interconnecting the two components (Uchida & Sakurai 1983).

The hypothesis that the two components at different temperatures are confined in loops of different size is confirmed by observations of the eclipsing system AR Lac performed with the EXOSAT satellite during a complete orbital cycle, in two different energy bands between 0.05 and 2 keV and between 1 and 30 keV (White et al. 1990a). The observations show a reduction of the low-energy X-ray emission during eclipses, which is not observed in the more energetic band: this implies that the cool component (which emits at lower energies) must be confined in small loops of stellar size, while the hot one, which is not eclipsed, must be contained in loops extended over the binary system.

§ 1.2 Radio emission of RS CVn systems

One of the fundamental characteristics of RS CVn systems is the presence of a strong continuum radio emission at centimeter wavelengths, with luminosity between 10^{14} and 10^{18} erg sec^{-1} Hz^{-1}, many orders of magnitude higher than observed on the Sun and on single late-type stars. The emission is highly variable and is characterized by periods of activity when strong flares are observed, with flux densities generally of the order of a few hundred mJy, but that can reach values up to ~ 1 Jy. These events have typical timescales of the order of a few hours, with a decay slower than the rising phase, and can occur for several days: an example is the series of outbursts observed in February 1978 on the system HR 1099 (Feldman et al. 1978), which occurred over the nine days of observation with a mean frequency of one per day (Fig. 1.1).

Active periods are separated by periods of low activity, when the emission is much weaker, generally of the order of a few mJy (i.e. one or two orders of magnitude lower than flares). A comparison between the radio emission and the mean variation of the optical light curve over a period of several years seems to indicate that the strongest flares have a greater probability to occur near the

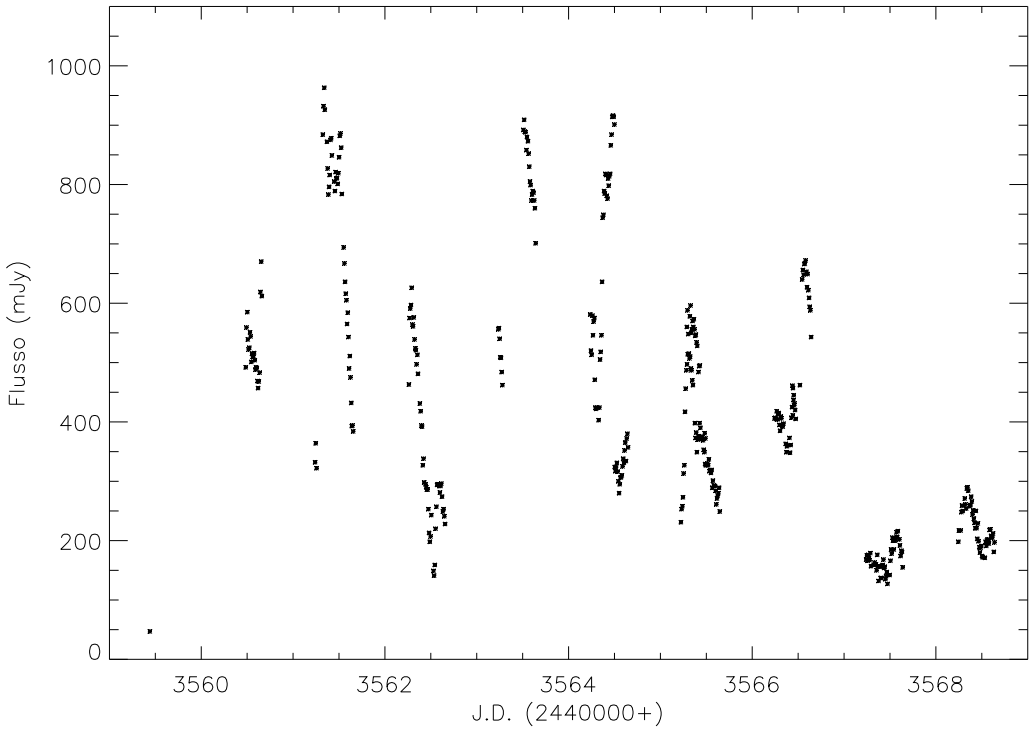

Fig. 1.1 Radio light curve of HR 1099 at 10.5 GHz during the February 1978 flare (Feldman et al. 1978).

minimum of the optical luminosity, i.e. at the time of maximum coverage of the stellar surface with spots, while near the optical maximum generally only quiescent emission or moderate flares are observed (Umana et al. 1995).

Although the radio emission from RS CVn systems has been extensively observed since their discovery, in most cases the observations have been sporadic and limited to a single frequency (typically 5 GHz), expecially for the quiescent emission which was often comparable or lower than the sensitivity limit of the radiotelescopes being used. Only during the past few years have reliable multiwavelength observations of both intensity and polarization become available in the literature, especially for the most active systems UX Ari, HR 1099 and HR 5110 (Pallavicini et al. 1985; Willson & Lang 1987; White et al. 1990b; Massi & Chiuderi Drago 1992; Umana et al. 1993; Su et al. 1993; Fox et al. 1994; Jones et al. 1994). These observations are in agreement with the results

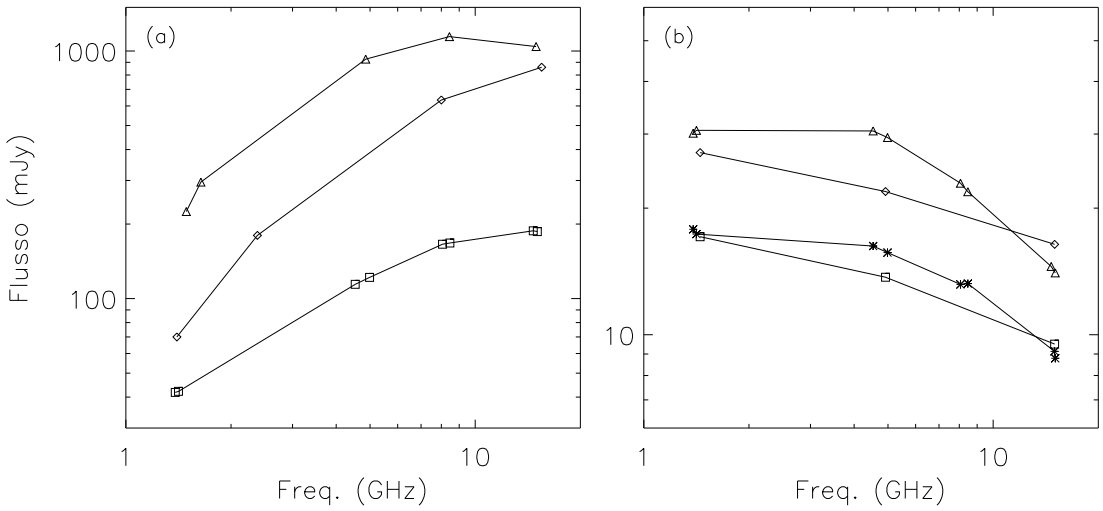

Fig. 1.2 Spectra of the flaring (a) and quiescent (b) emission. Data are from Feldman et al. (1978), Pallavicini et al. (1985), Su et al. (1993) and White & Franciosini (1995).

of a statistical study of the spectrum and polarization properties performed by Mutel et al. (1987), who observed a sample of RS CVn systems at 1.4, 4.9 and 15 GHz during a period of three years and compared their results with the few previously published data.

The general properties of the radio emission deduced from the observations can be summarized as follows: during strong flares the spectrum has a positive spectral index $\alpha \simeq 1$ (defined as $F_\nu \propto \nu^\alpha$) up to $8-15$ GHz, while for moderate flares generally there is a peak at lower frequencies and the spectrum is flatter. Typical quiescent spectra are instead flat, with $\alpha \lesssim 0$ between 1.4 and 15 GHz. In some cases very similar values of α have been observed during different low-level activity periods (Pallavicini et al. 1985; Massi & Chiuderi Drago 1992). Some examples of flaring and quiescent spectra are shown in Fig. 1.2.

Mutel et al. (1987) have shown that there is a very good correlation between the spectral index measured between 1.4 and 5 GHz, and the ratio of the radio luminosity at 5 GHz to the mean luminosity, $\log(L_{\rm R}/\langle L_{\rm R}\rangle)$, in the sense that α decreases, going from positive to negative values, as the luminosity decreases (Fig. 1.3a). This correlation is confirmed by an analysis of other recent

observations, reported in Tab. 1.1, as it can be seen in Fig. 1.3b.

The emission is circularly polarized, with a degree of polarization π_c anticorrelated with the flux density: while the quiescent component can reach values of π_c up to 40 %, flares are generally unpolarized or weakly polarized ($\pi_c \lesssim 10$ %). No evidence for significant linear polarization has been reported: this is presumably because, even if there were significant linear polarization intrinsic to the source, the large Faraday rotation during the propagation of the radiation through the stellar corona and the lack of spatial resolution would destroy it completely.

Non-eclipsing systems, such as HR 1099, HR 5110 and UX Ari, often show a reversal in the sense of circular polarization between 1.4 and 5 GHz (HR 5110 has always been found to be unpolarized at 1.5 GHz); moreover, for the best studied objects the sense of polarization at a given frequency has been observed to be nearly always the same over more than 15 years. Generally at frequencies above 5 GHz the sense is right-hand (Stokes parameter $V > 0$) for HR 1099 and HR 5110, and left-hand ($V < 0$) for UX Ari.

The presence of circular polarization and high brightness temperatures ($T_b = 10^8 - 10^9$ K for the quiescent component and $T_b \gtrsim 10^{10}$ K for flares) has generally been interpreted as due to gyrosynchrotron emission from mildly-relativistic electrons (e.g. Owen et al. 1976; Kuijpers & van der Hulst 1985). Thermal bremsstrahlung must in fact be excluded, since, in order to reproduce the observed flux densities, it requires values of temperature and emission measure several orders of magnitude higher than those obtained from X-ray observations (Borghi & Chiuderi Drago 1985; Kuijpers & van der Hulst 1985). The assumption of gyrosynchrotron emission from a non-thermal (power-law) distribution of mildly-relativistic electrons (Lorentz factor $\gamma = 1 - 10$) can reproduce the spectrum of the 1978 flare on HR 1099, assuming that the emission originates in an inhomogeneous source, with a uniform magnetic field of ~ 100 G and a decreasing electron density (Borghi & Chiuderi Drago 1985), or with a uniform density and a magnetic field consisting of an arcade of dipolar loops anchored on the active star or connecting the two components (Klein & Chiuderi Drago 1987).

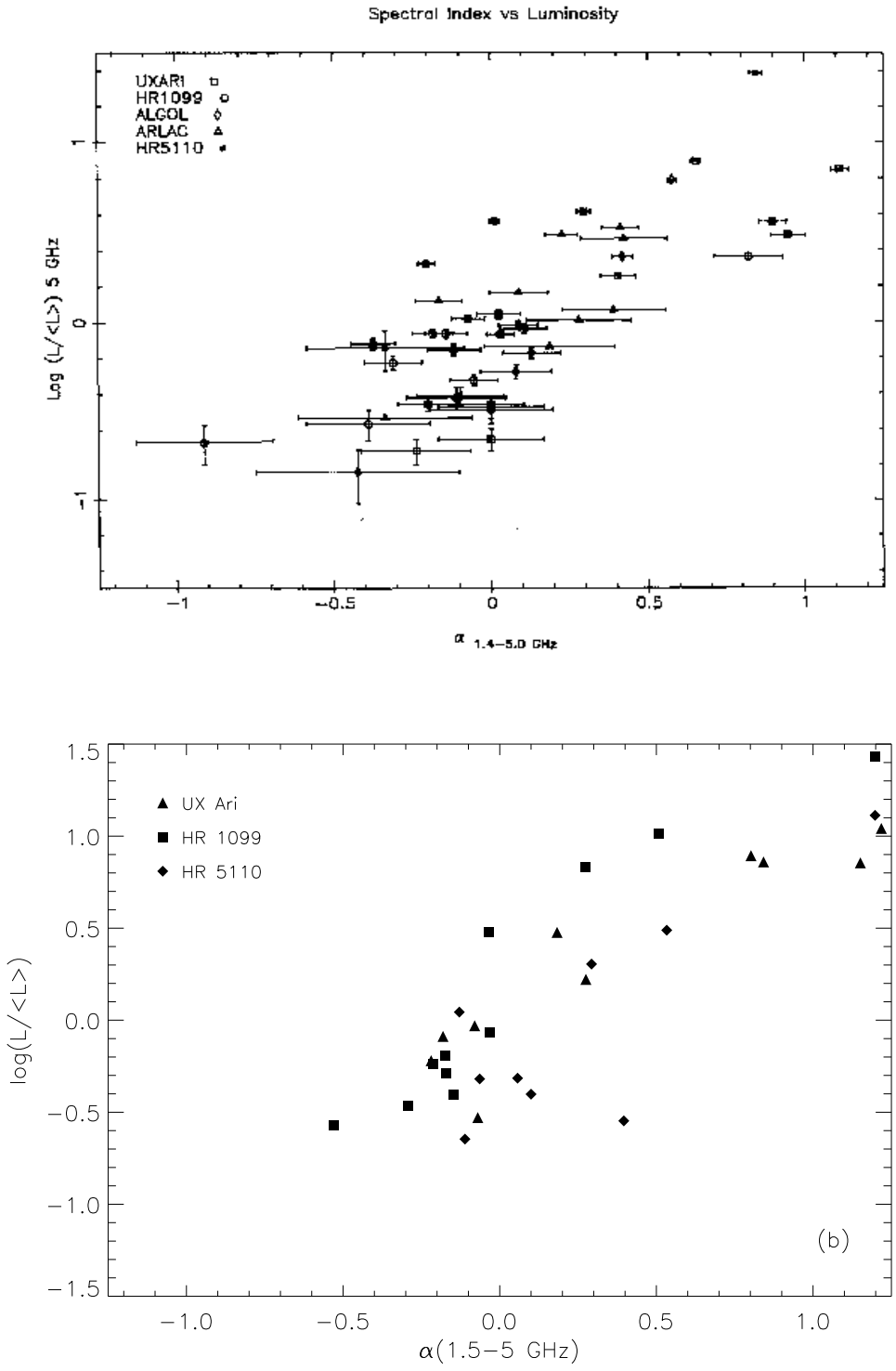

Fig. 1.3 Correlation between the spectral index α(1.4-5 GHz) and $\log(L_{\rm R}/\langle L_{\rm R}\rangle)$. (a) Relation found by Mutel et al. (1987); (b) relation obtained with the data in Table 1.1.

Tab. 1.1 Radio observations of RS CVn systems added to the Mutel et al. (1987) correlation in Fig. 1.3b

Stella	Dist. (pc)	α(1.4-5)	$L_{5\ \mathrm{GHz}}$ (erg/s Hz)	Data	Ref
UX Ari	50	− 0.181	$4.08\ 10^{16}$	12/01/84	1
		− 0.219	$3.01\ 10^{16}$	29/01/84	1
		0.183	$1.50\ 10^{17}$	23/03/84	1
		1.151	$3.58\ 10^{17}$	10/06/85	2
		1.825	$8.05\ 10^{17}$	10/06/85	2
		0.275	$8.34\ 10^{16}$	25/01/89	4
		− 0.070	$1.48\ 10^{16}$	9/08/90	6
		1.218	$5.51\ 10^{17}$	5/07/93	7
		0.802	$3.92\ 10^{17}$	22/12/93	7
		0.842	$3.62\ 10^{17}$	23/04/94	7
		− 0.080	$4.67\ 10^{16}$	13/08/94	7
HR 1099	35	− 0.174	$3.20\ 10^{16}$	12/01/84	1
		− 0.171	$2.57\ 10^{16}$	29/01/84	1
		− 0.293	$1.72\ 10^{16}$	10/06/85	2
		1.199	$1.35\ 10^{18}$	9/10/88	3
		0.507	$5.18\ 10^{17}$	15/10/88	3
		0.272	$3.41\ 10^{17}$	21/10/88	3
		− 0.529	$1.34\ 10^{16}$	25/01/89	4
		− 0.036	$1.50\ 10^{17}$	5/07/93	7
		− 0.214	$2.88\ 10^{16}$	1/12/93	7
		− 0.147	$1.96\ 10^{16}$	23/04/94	7
		− 0.031	$4.30\ 10^{16}$	13/08/94	7
HR 5110	52	− 0.129	$5.54\ 10^{16}$	9/06/85	2
		− 0.111	$1.13\ 10^{16}$	25/01/89	4
		0.057	$2.42\ 10^{16}$	26/01/89	4
		0.293	$1.01\ 10^{17}$	18/02/89	5
		0.533	$1.54\ 10^{17}$	6/03/89	5
		0.396	$1.42\ 10^{16}$	18/06/93	7
		1.198	$6.49\ 10^{17}$	18/12/93	7
		0.100	$1.98\ 10^{16}$	8/04/94	7
		− 0.064	$2.40\ 10^{16}$	10/06/94	7

1 - Pallavicini et al. (1985)
2 - Willson & Lang (1987)
3 - Su et al. (1993)
4 - White et al. (1990b)
5 - Umana et al. (1993)
6 - Fox et al. (1994)
7 - White & Franciosini (1995)

The interpretation of the quiescent component has been more controversial, also because of the limited spectral data available until a few years ago. From the analysis of a sample of 122 RS CVn systems Drake et al. (1989, 1992) found a correlation between the X-ray luminosity $L_{\rm X}$ and the radio luminosity at 6 cm L_6, described by the relation $L_6/L_{\rm bol} \propto (L_{\rm X}/L_{\rm bol})^{1.13}$, where $L_{\rm bol}$ is the bolometric luminosity of the system. This correlation led the above authors to suggest the hypothesis that the quiescent emission is due to gyrosynchrotron radiation from the same population of thermal electrons responsible for the hot X-ray component. Using the observed values of the X-ray and 6-cm radio flux for UX Ari, Drake et al. estimate that the source should possess a magnetic field $B \sim 200$ G, which is in agreement with the values deduced from flare spectra. However a uniform magnetic field is not able to reproduce the flat quiescent spectrum, since thermal gyrosynchrotron emission gives a spectral index $\alpha = +2$ in the optically thick case and $\alpha = -8$ in the optically thin case, while the observed one is generally between -0.9 and $+0.1$ (Mutel et al. 1987). Numerical calculations have shown that the only way to reproduce the quiescent spectrum in the thermal case is to assume that the magnetic field decreases with distance from the active star as r^{-1} (Chiuderi Drago & Franciosini 1993). Although a similar trend might be plausible in the presence of interaction between the magnetic fields of the two components, it seems rather unlikely that the magnetic configuration during quiescent phases is so different from that of a dipolar field, which reproduces very well not only the flaring spectrum of HR 1099, but also the structure of active regions in the solar corona. On the contrary, a non-thermal distribution of electrons, described by a power-law, can reproduce very well the flat spectrum of the quiescent emission in the assumption of a homogeneous source with a magnetic field of the order of 10 G (Chiuderi Drago & Franciosini 1993), as long as sufficiently energetic electrons ($\gamma_{\rm max} \gtrsim 50$) are present. Magnetic fields of this order of magnitude are compatible with the observation that the quiescent emission has a lifetime of at least two days (Massi & Chiuderi Drago 1992) and suggest that the source is located at the top of the magnetic loops.

In two recent papers, Güdel & Benz (1993) and Benz & Güdel (1994) have

shown that the correlation between radio and X-ray luminosity is not limited to RS CVn systems only, but is valid for several classes of late-type (F to M) stars with coronal magnetic activity, extending with nearly the same slope over five orders of magnitude, independently of age, spectral type, binarity, rotation and photospheric and chromospheric activity; moreover, this correlation also holds for solar flares. According to the above authors such correlation can be explained assuming a common mechanism of energy release, during which part of the energy goes into heating of the corona, generating the X-ray emission, and part goes into acceleration of the particles responsible for the radio emission.

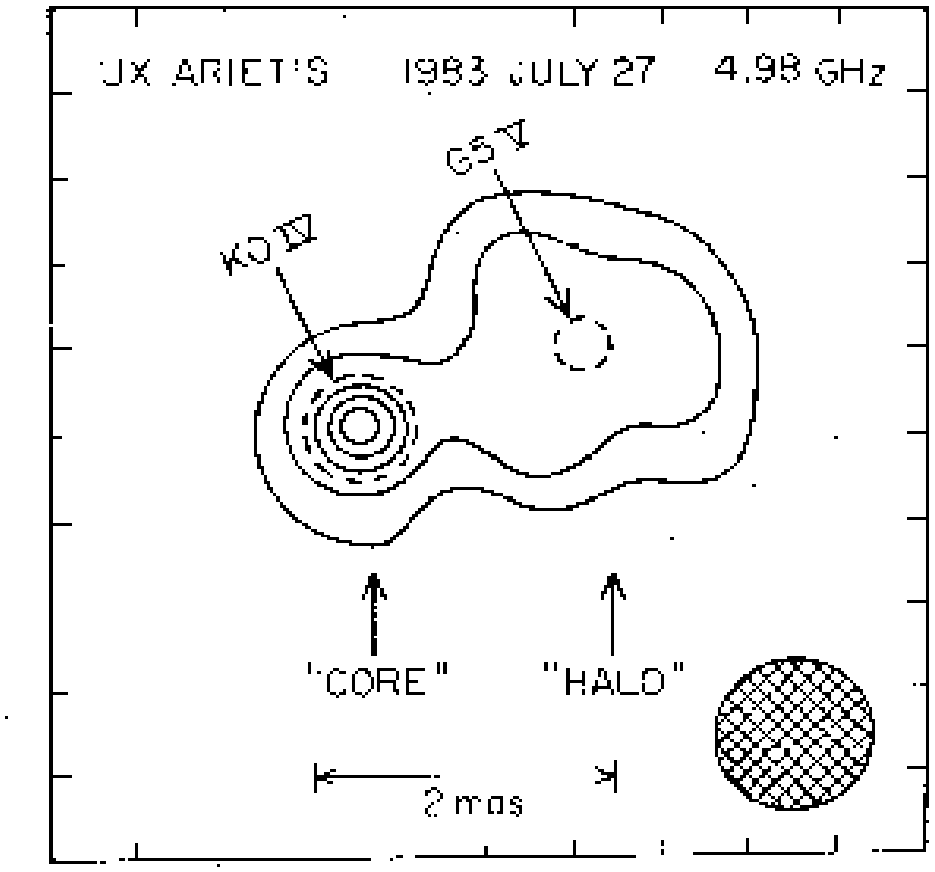

Fig. 1.4 VLBI map of UX Ari at 4.98 GHz (Mutel et al. 1985).

The hypothesis that the quiescent component is due to non-thermal emission like flares is confirmed by several VLBI observations of RS CVn systems (Mutel et al. 1984, 1985; Lestrade et al. 1984a, 1984b; Little-Marenin et al. 1986; Massi et al. 1988; Trigilio et al. 1993, 1995). These observations have shown that, while flares are generally associated with a compact bright source (core) of size comparable to the stellar radius, the quiescent component arises from an extended halo, whose dimensions are of the order of the binary separation; sometimes, as in the case of an observation of UX Ari (Mutel et al. 1985), a core-halo structure is observed, where both components are present (Fig. 1.4). The existence of these three possible structures of the radio source (core only, core-halo and halo only) suggested to Mutel et al. (1985) that they could represent three different phases of the decay of a flaring event: in this hypothesis, the core originates at the flare onset, due to the acceleration of particles in a compact active region with high magnetic field, which is initially optically thick. The source then expands outwards in regions of lower field strength, becoming optically thin and giving the core-halo structure. The core then disappears rapidly, due to the higher efficiency of energy losses, leaving only the halo which decays more slowly; in this scenario the quiescent emission would originate during the decay of the halo and would therefore be the last residual of the flaring event.

More recent VLBI observations (Lestrade et al. 1988; Trigilio et al. 1993, 1995) performed during the rising phase of flares however indicated that the source maintained a constant size (comparable to the binary system separation) while the flux density rose, and the same was true during the initial phases of the decay, with a slight decrease of the source size towards the end of the flare. This implies that there is not an expansion of the source, as suggested by Mutel et al. (1985), but the variations of the flux density and optical depth are rather due to variations in the number of emitting particles in the source.

In some cases, at frequencies below 3 GHz, a highly-variable and highly-polarized emission has been observed, with $\pi_c \gtrsim 50 - 70$ % (Brown & Crane 1978; Gibson et al. 1978; Mutel & Weisberg 1978; Fix et al. 1980; Simon et al. 1985; Lestrade et al. 1988). The rapid variability, together with the

high brightness temperature ($> 10^9$ K) and polarization are not consistent with the gyrosynchrotron mechanism, and have generally been interpreted as due to coherent outbursts.

§ 1.3 Characteristics of Algol-type systems

Algol-type binaries are often considered together with RS CVns since they show an X-ray and radio emission with similar characteristics as RS CVn systems, in spite of being physically different; moreover, there are some systems with intermediate characteristics (such as HR 5110, RT Lac, AR Mon) that are sometimes classified as RS CVn, sometimes as Algols.

Algol-type systems are close eclipsing binaries consisting of a main-sequence primary of spectral type B–A, and a subgiant or giant secondary of spectral type G–K which fills its Roche lobe and is therefore transferring mass on the companion. The cool secondary components of these systems, being rapidly-rotating convective stars, should show all the characteristics of chromospheric and photospheric activity observed in RS CVn systems (Hall 1989). However the study of these properties is difficult because of the higher luminosity of the primary and the emission from the circumstellar material, that dominate the blue and ultraviolet region of the spectrum, making the contribution of the secondary hardly distinguishable. Nevertheless, in some systems a weak emission in the central part of the CaII H and K lines, attributable to the cool star, has been observed; moreover, UV observations have shown the presence of emission lines with fluxes comparable to those of RS CVns mostly originating from the secondary (Guinan & Giménez 1993). In addition, observations of the Algol light curve in the infrared at 1.2 μm, where the contribution of the cool star is higher, have shown variations of the depth of the minima during both eclipses and evidence of a photometric wave with amplitude of $\sim 0.05 - 0.1$ mag, indicating the presence of spots on the secondary component (Richards 1990).

Like RS CVn systems, Algol-type binaries show an X-ray emission with luminosity $L_{\rm X} \sim 10^{30} - 10^{31}$ erg sec^{-1}, characterized by strong long-duration

flares and by a quiescent emission, whose spectrum is compatible with two thermal components at different temperatures ($T_{\rm cool} \sim 1-6\times10^6$ K and $T_{\rm hot} \sim 2-5\times10^7$ K); the emission is attributed to coronal plasma contained in magnetic loops around the K star.

The properties of the radio emission are also similar to those of RS CVn systems: the mean luminosity of Algol-type systems at 6 cm is $\langle L_{\rm R} \rangle = 2\times10^{16}$ erg sec^{-1} Hz^{-1} and the radio emission is characterized by flares and by a quiescent component of the order of a few mJy with a flat spectrum (Umana et al. 1993), consistent with gyrosynchrotron emission. Contrary to RS CVn systems, however, the emission is generally unpolarized or very weakly polarized, even during quiescent periods. VLBI observations of Algol have shown that the emitting region has dimensions comparable to the binary system (Mutel et al. 1985; Lestrade et al. 1988; Massi et al. 1988) and that during flares a *core-halo* structure is present, similar to that of UX Ari (Mutel et al. 1985). Moreover, in the case of Algol a highly-variable and polarized emission has also been observed, indicative of coherent emission processes (Lestrade et al. 1988).

CHAPTER 2

TIME EVOLUTION OF THE RADIO EMISSION

§ 2.1 Introduction

As mentioned in Chapt. 1, VLBI observations of RS CVn systems have shown that the source has a variable structure, with the emission concentrated in a compact and very bright region (*core*) during strong flares, and extended over the entire binary system (*halo*) during quiescent phases; at intermediate flux levels often a *core-halo* structure is observed, where both components are present (Mutel et al. 1985; Lestrade et al. 1988). Based on these characteristics, Mutel et al. (1985) proposed in a qualitative way that the quiescent component might constitute the final phase of the decay of a flaring event. According to the above authors, in fact, this component is due to the emission from the fraction of electrons of the initial distribution that remained trapped in regions of low density and magnetic field, where synchrotron and collision energy losses are less efficient, and that therefore can radiate longer. This hypothesis is in agreement with the UX Ari observations by Massi & Chiuderi Drago (1992), who showed that the quiescent flux density remained constant, within the measurement errors, for at least two consecutive days, implying a maximum magnetic field of 30 G in the source; moreover, theoretical calculations of gyrosynchrotron models indicate that in order to reproduce the quiescent spectra a magnetic field of $B \sim 10$ G is required (Chiuderi Drago & Franciosini 1993).

In this chapter we will propose a quantitative model that takes these obser-

vations into account. We will assume that electrons are accelerated impulsively at the flare onset ($t = 0$) with a power-law energy distribution that reproduces the flare spectrum, and that they are then subject to energy losses by collisions with the electrons of the thermal plasma and by emission of synchrotron radiation. The variation with time of the particle distribution modifies consequently the spectrum of the emitted radiation; as we will see, preliminary calculations performed in the assumption of a homogeneous source show that, for a magnetic field of the order of 5 G, the computed spectrum $5-6$ days after the flare onset is in very good agreement with the spectra of the quiescent emission. The predictions of this model on the lifetime of the quiescent emission agree with the observations, that indicate that the frequency of low- and medium-intensity flares ($50-200$ mJy) in these systems is sufficiently high (Neidhöfer et al. 1993; Torricelli Ciamponi et al. 1995; Umana et al. 1995; Trigilio et al. 1996; Massi et al. 1996), confirming the hypothesis that electrons are accelerated during flares. This result motivated us to improve the model, introducing a more realistic source structure, with a dipolar magnetic field, and taking into account, in the calculation of the evolution of the distribution and of the spectrum, both the electrons escaping into the loss-cone and the influence of the thermal coronal plasma through free-free emission and absorption and the Razin effect. As we will see, this model reproduces very well the spectral characteristics of RS CVn systems, as well as the evolution of the source structure.

§ 2.2 Time evolution of the energy distribution and of the spectrum: general equations

The time evolution of an isotropic and homogeneous energy distribution $N(\gamma, t)$ is described in general by the following equation (Melrose & Brown 1976; Melrose 1980):

$$\frac{\partial N(\gamma,t)}{\partial t} + \frac{\partial}{\partial \gamma}\left[N(\gamma,t)\,\frac{\mathrm{d}\gamma}{\mathrm{d}t}\right] = Q(\gamma,t) - \nu_L\, N(\gamma,t)\,, \qquad (2.1)$$

where $\mathrm{d}\gamma/\mathrm{d}t$ represents the energy variation of the electrons as a consequence of losses or gains, assumed to depend only on γ ($\mathrm{d}\gamma/\mathrm{d}t = \varphi(\gamma)$), $Q(\gamma, t)$ is

the source function describing the density of electrons that are injected in the source at time t per unit time and energy band, while $\nu_L\, N(\gamma, t)$ represents the density of electrons that are removed from the region, again per unit time and energy band. The general solution of Eq. (2.1) is given by (Melrose & Brown 1976):

$$\begin{aligned} N(\gamma, t) = & \frac{\mathrm{d}\gamma_\circ}{\mathrm{d}\gamma}\, N(\gamma_\circ, 0)\, \mathrm{e}^{\,[H(\gamma) - H(\gamma_\circ)]} + \\ & + \frac{1}{|\varphi(\gamma)|} \int_\gamma^{\gamma_\circ} \mathrm{d}\gamma^{\,\prime}\, \mathrm{e}^{\,[H(\gamma) - H(\gamma^{\,\prime})]}\, Q\,[\gamma^{\,\prime}, t - h(\gamma^{\,\prime}) + h(\gamma)]\,, \end{aligned} \tag{2.2}$$

where $N(\gamma_\circ, 0)$ is the distribution at the initial time $t = 0$, with $\gamma_\circ = \gamma\,(t = 0)$, and:

$$h(\gamma) = \int_1^\gamma \frac{\mathrm{d}\gamma^{\,\prime}}{|\,\varphi(\gamma^{\,\prime})\,|} \quad ; \quad H(\gamma) = \int_1^\gamma \frac{\nu_L}{|\,\varphi(\gamma^{\,\prime})\,|}\, \mathrm{d}\gamma^{\,\prime}\,. \tag{2.3}$$

The relationship between $\gamma_\circ$ and γ can be derived by integrating the equation:

$$\frac{\mathrm{d}\gamma}{\mathrm{d}t} = \varphi(\gamma)\,. \tag{2.4}$$

There are several factors contributing to the decrease of the electron energy; in a magnetized plasma the most important mechanisms are Coulomb collisions with thermal electrons, bremsstrahlung, emission of synchrotron radiation and inverse Compton effect (Petrosian 1985; Pacholczyk 1970). However in our case only losses by Coulomb collisions and synchrotron radiation are important, while the other two mechanisms are generally negligible. In a fully ionized plasma collision and synchrotron losses are described by the following relations (Petrosian 1985):

$$\begin{aligned} \dot{\gamma}_C &= -\,6 \times 10^{-13}\, n_\mathrm{e} \\ \dot{\gamma}_S &= -\,1.3 \times 10^{-9}\, B^2 \gamma^2 \end{aligned} \tag{2.5}$$

where n_e is the thermal plasma density, B is the magnetic field in the source, and we have taken for synchrotron losses a mean value over the electron pitch angle (angle between velocity and magnetic field).

The relative importance of these processes depends on energy: collision losses dominate for low values of γ, while synchrotron losses are more important at high energies. Therefore, collision losses have the effect of reducing

the number of low-energy electrons, flattening the distribution, while radiative losses strongly reduce the number of energetic electrons, causing a sharp cutoff at a given value of γ which depends on time. As a result, if both effects are present after some time one obtains a flatter distribution with a lower maximum energy with respect to the initial one.

Using Eq. (2.5), Eq. (2.4) becomes:

$$-\frac{\mathrm{d}\gamma}{\mathrm{d}t} = \alpha + \eta\gamma^2 \,, \tag{2.6}$$

with $\alpha = 6 \times 10^{-13}\, n_\mathrm{e}$ and $\eta = 1.3 \times 10^{-9}\, B^2$, from which we obtain:

$$\gamma(t) = \frac{A\gamma_\circ - \tan A\alpha t}{A\,(1 + A\gamma_\circ \tan A\alpha t)} \,, \tag{2.7}$$

where $A = \sqrt{\eta/\alpha}$.

The time evolution of the spectrum can be obtained by substituting, at any time t, the energy distribution $N(\gamma, t)$ derived from Eq. (2.2) in the expressions for the gyrosynchrotron emissivity and absorption coefficient, and then computing the intensity by solving the transfer equation. Approximate expressions for the emissivity j_ν and the absorption coefficient k_ν in a plasma, valid for $\nu/\nu_\mathrm{b} \geq 3-4$, where ν_b is the gyrofrequency, have been derived by Klein (1987) extending the method developed by Petrosian (1981) for emission in a vacuum. In the case of an isotropic energy distribution $N(\gamma)$ they can be written as:

$$\begin{aligned} j_\nu &= \frac{\mathrm{e}^2\nu}{2\,c}\sqrt{\frac{\pi\,\nu_\mathrm{b}}{\nu}}\int_1^\infty \mathrm{d}\gamma\; Y_\circ(\gamma,\theta)\,N(\gamma) \\ k_\nu &= \frac{-\,\mathrm{e}^2}{2\,m_\mathrm{e}\,c\,n\,\nu}\sqrt{\frac{\pi\,\nu_\mathrm{b}}{\nu}}\int_1^\infty \mathrm{d}\gamma\; Y_\circ(\gamma,\theta)\,\left[\frac{\mathrm{d}N(\gamma)}{\mathrm{d}\gamma} - \frac{N(\gamma)\,(2\gamma^2-1)}{\gamma\,(\gamma^2-1)}\right] \end{aligned} \tag{2.8}$$

where θ is the angle between the magnetic field and the line of sight, and:

$$Y_\circ(\gamma,\theta) = \frac{Z_\circ^{2s_\circ}}{\gamma^{1/2}\varepsilon^3\,(1+t_\circ^2)^{1/4}}\,\frac{[-\,a(t_\circ,s_\circ)\,b(t_\circ,s_\circ)\,(1+t_\circ^2) + a_\theta\cos\theta]^2}{n\sin\theta\,(1+a_\theta^2)\,a^2(t_\circ,s_\circ)} \,, \tag{2.9}$$

where $\varepsilon = 1/\sqrt{1-n^2\beta^2}$, $t_\circ = \varepsilon\, n\, \beta \sin\theta$ and $\beta = \sqrt{\gamma^2-1}/\gamma$. The quantities

$Z_\circ$, $s_\circ$, $a(t_\circ, s_\circ)$ and $b(t_\circ, s_\circ)$ are given by:

$$\begin{aligned} Z_\circ &= \frac{t_\circ \, \mathrm{e}^{1/\sqrt{1+t_\circ^2}}}{1+\sqrt{1+t_\circ^2}} \, ; \\ s_\circ &= \frac{\gamma}{\varepsilon^2} \, \frac{\nu}{\nu_\mathrm{b}} \, (1+t_\circ^2) \, ; \\ a(t_\circ, s_\circ) &= \left[(1+t_\circ^2)^{-3/2} + \frac{0.503297}{s_\circ} \right]^{1/6} \, ; \\ b(t_\circ, s_\circ) &= \left[(1+t_\circ^2)^{-3/2} + \frac{1.193000}{s_\circ} \right]^{1/6} \left(1 - \frac{1}{5 \, s_\circ^{2/3}} \right) \, . \end{aligned} \tag{2.10}$$

The expressions of j_ν and k_ν in the two ordinary (+) and extraordinary (−) modes are obtained by substituting in Eq. (2.8) the corresponding values of the refraction index $n_\pm$ and of the polarization coefficients $a_{\theta\pm}$, that can be written as:

$$\begin{aligned} n_\pm^2 &= 1 - \frac{X}{1 + Y \, |\cos\theta| \, (-\xi \pm \sqrt{1+\xi^2})} \, , \\ a_{\theta\pm} &= \frac{\cos\theta}{|\cos\theta|} \, \frac{1}{-\xi \pm \sqrt{1+\xi^2}} \, , \end{aligned} \tag{2.11}$$

where:

$$X = \frac{\nu_\mathrm{p}^2}{\nu^2} \, ; \qquad Y = \frac{\nu_\mathrm{b}}{\nu} \, ; \qquad \xi = \frac{Y \, \sin^2\theta}{2 \, (1-X) \, |\cos\theta|} \tag{2.12}$$

(ν_p = plasma frequency).

In the assumption that the two modes of radiation propagate independently, it is possible to solve the transfer equation separately, obtaining the intensity in the ordinary and extraordinary modes, $I^\pm$, and then the total intensity $I = I^+ + I^-$ from which the flux density is derived.

§ 2.3 Time evolution in a homogeneous source

As a preliminary calculation, we consider the evolution of the emission from the halo only, which is assumed to consist of a cylindrical source of radius $L/2$ and height L, where L is equal to the binary separation ($L \simeq 1.2 \times 10^{12}$ cm), with a uniform magnetic field $B \leq 30$ G and a constant density of relativistic electrons. For simplicity we assume that the thermal coronal plasma influences

only the electron distribution through collisions, but we neglect the effect on the emitted radiation (free-free and Razin effect), considering the emission as if taking place in a vacuum ($n_{\pm} \simeq 1$).

We also assume that electrons are accelerated impulsively at the flare onset, corresponding to $t = 0$, and are then subject to energy losses only; in this case in Eq. (2.1) we have $Q(\gamma, t) = \nu_L = 0$ and Eq. (2.2) is reduced simply to:

$$N(\gamma, t) = N(\gamma_\circ, 0) \, \frac{\mathrm{d}\gamma_\circ}{\mathrm{d}\gamma} \, . \tag{2.13}$$

If the initial distribution is an isotropic power-law of the form:

$$N(\gamma_\circ, 0) = K \, (\gamma_\circ - 1)^{-\delta} \, , \tag{2.14}$$

with $\gamma_{\circ 1} \leq \gamma_\circ < \infty$ and $K = N_\circ \, (\delta - 1) \, (\gamma_{\circ 1} - 1)^{\delta - 1}$, where $N_\circ$ is the total number density of relativistic electrons at $t = 0$ ($N_\circ = \int_{\gamma_{\circ 1}}^{\infty} N(\gamma_\circ, 0) \, \mathrm{d}\gamma_\circ$), the distribution at a time t is given by:

$$N(\gamma, t) = K(1 + \tan^2 A\alpha t) A^{\delta} \, \frac{[A\gamma \, (1 + A \tan A\alpha t) - A + \tan A\alpha t]^{-\delta}}{(1 - A\gamma \tan A\alpha t)^{2-\delta}} \tag{2.15}$$

with $\gamma_1 \leq \gamma \leq \gamma_2$, where:

$$\gamma_1 = \frac{A\gamma_{\circ 1} - \tan A\alpha t}{A \, (1 + A\gamma_{\circ 1} \tan A\alpha t)} \, , \qquad \gamma_2 = \frac{1}{A \tan A\alpha t} \, . \tag{2.16}$$

The condition $\gamma_1, \, \gamma_2 > 1$ implies the existence of two characteristic times t_1 and t_2, given by:

$$t_1 = \frac{1}{A\alpha} \, \arctan \frac{A(\gamma_{\circ 1} - 1)}{1 + A^2 \, \gamma_{\circ 1}} \, , \qquad t_2 = \frac{1}{A\alpha} \, \arctan \frac{1}{A} \, . \tag{2.17}$$

For $t < t_1$, all particles of the initial distribution still have $\gamma > 1$ and therefore emit gyrosynchrotron radiation. For $t_1 \leq t < t_2$ the lower-energy electrons have been thermalized, giving $\gamma_1 = 1$; the number density of relativistic electrons decreases with time, becoming equal to zero for $t = t_2$, when also $\gamma_2 = 1$ and all particles have lost their energy. For $t \geq t_2$ there is no more emission from the source.

If we indicate with $N_{\rm R}(t)$ the total number density of relativistic electrons at time t:

$$N_{\rm R}(t) = \int_{\gamma_1(t)}^{\gamma_2(t)} N(\gamma, t)\, {\rm d}\gamma \ , \tag{2.18}$$

we obtain:

$$\frac{N_{\rm R}(t)}{N_\circ} = \begin{cases} 1 & t < t_1 \\ \left[\dfrac{A(1 - A\tan A\alpha t)(\gamma_{\circ 1} - 1)}{(1 + A^2)\tan A\alpha t}\right]^{\delta - 1} & t_1 \le t < t_2 \\ 0 & t \ge t_2 \ . \end{cases} \tag{2.19}$$

The time evolution of the energy distribution in the two cases $\delta = 2$ and $\delta = 3$, with $\gamma_{\circ 1} = 1.1$, is shown in Fig. 2.1 for a magnetic field $B = 10$ G and a thermal plasma density $n_{\rm e} = 10^8$ cm^{-3}. The decrease of the number of low-energy electrons due to collision losses causes a flattening of the distribution, which becomes nearly constant with a sharp cut-off near the upper limit γ_2. The value of γ_2 depends strongly on the magnetic field, decreasing rapidly with increasing B; moreover, the flattening at low energy is higher for higher values of $n_{\rm e}$ (Fig. 2.2).

The effect of the thermal plasma density and the magnetic field on the time evolution of $N_{\rm R}(t)/N_\circ$ is shown in Fig. 2.3. The number density of relativistic electrons falls off very rapidly in the first hours after the flare onset as a result of collisions, then the decrease depends on the magnetic field, being slower for lower values of B. If $B \gtrsim 20$ G the entire population is thermalized after two days; since the observations by Massi & Chiuderi Drago (1992) imply a lifetime of the quiescent component $\tau \gtrsim 2^{\rm d}$, it follows that it should come from regions where $B \le 10$ G.

Fig. 2.4 shows the time evolution of the spectrum in the case $\delta = 2$, $n_{\rm e} = 10^8$ cm^{-3}, for $B = 10$ G and $B = 5$ G, assuming $\theta = 45°$, a distance $d = 50$ pc (distance of UX Ari) and an initial column density $N_\circ L = 10^{17}$ cm^{-2}, in agreement with the values derived for flares. As it can be seen, the spectrum becomes optically thin in the frequency range of interest one or two days after the flare, and then it maintains nearly the same shape until there is a sufficient number of high energy electrons ($\gamma \ge 50$), that are necessary to keep

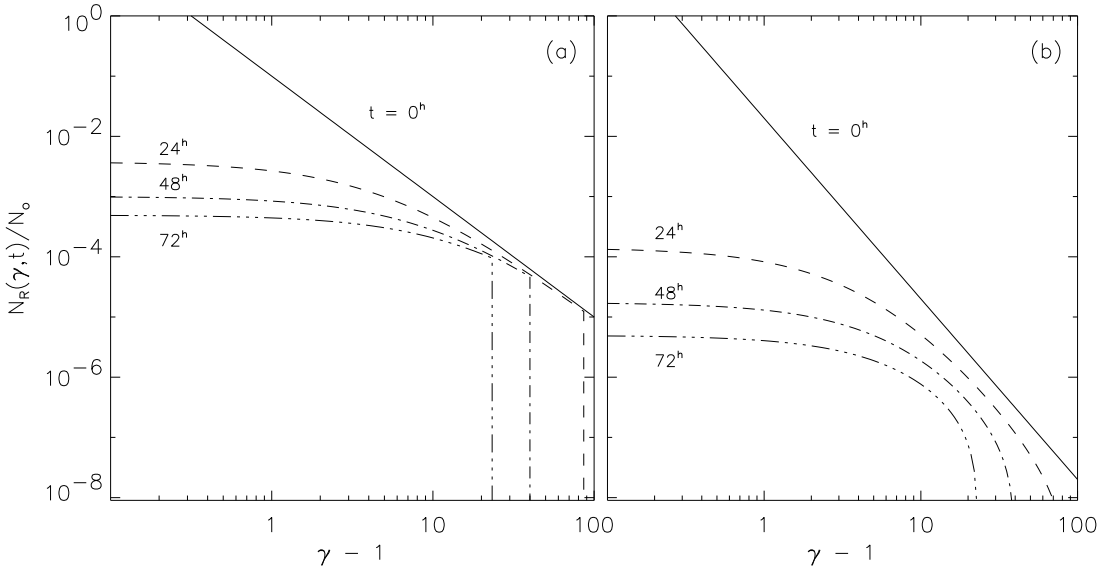

Fig. 2.1 Time evolution of the energy distribution for $\delta = 2$ (a) and $\delta = 3$ (b), in the case of a magnetic field $B = 10$ G and a thermal density $n_{\rm e} = 10^8$ cm^{-3}.

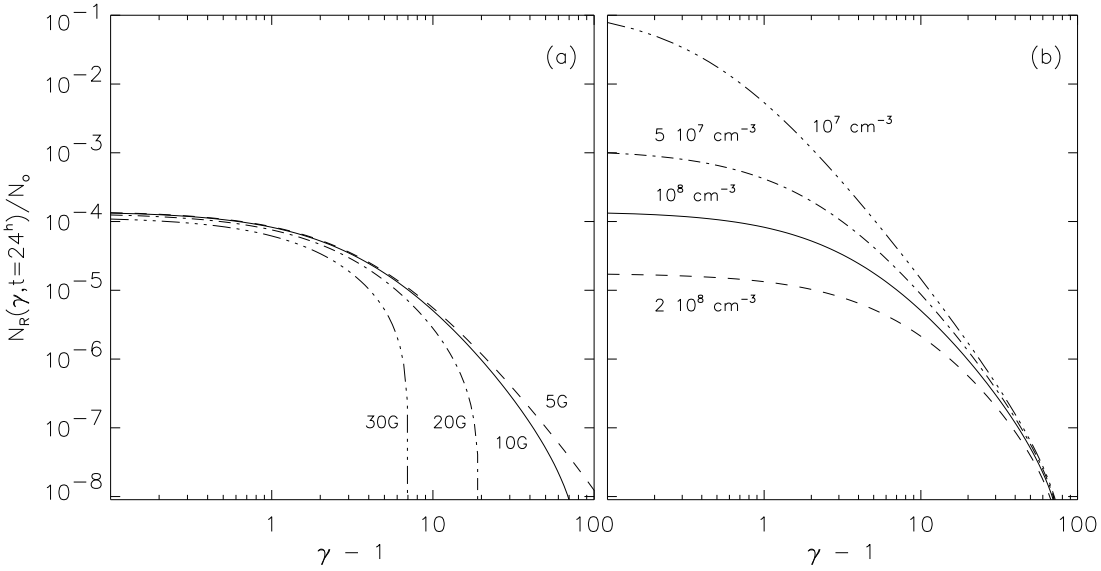

Fig. 2.2 Effect of the variation of B (a) and $n_{\rm e}$ (b) on the distribution for $t = 24^{\rm h}$ in the case $\delta = 3$. In both cases the solid curve corresponds to $B = 10$ G, $n_{\rm e} = 10^8$ cm^{-3}.

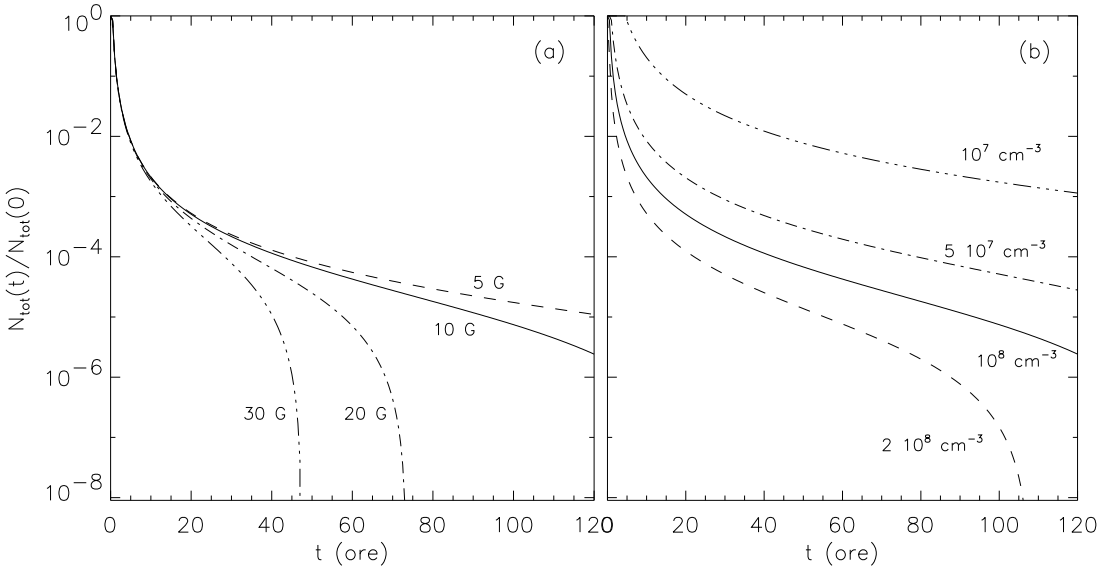

Fig. 2.3 Time evolution of the total number of relativistic particles, given by Eq. (2.19), in the case $\delta = 3$, for different values of the magnetic field (a) and thermal density (b). In both cases the solid curve corresponds to $B = 10$ G, $n_e = 10^8$ cm^{-3}.

the spectrum flat up to 15 GHz. When this is no longer true the slope at high frequencies increases. In the case $B = 5$ G the spectral shape remains almost the same for $5-6$ days after the flare onset and is in very good agreement with the slope of the observed quiescent spectra. Similar results are obtained with $\delta = 3$, although the spectrum is steeper and the flux density decreases more rapidly.

This simple model also predicts that the intensity of the emitted radiation from regions close to the star, where the field is higher ($B > 50 - 100$ G), dominates over the halo emission in the first hours after the flare onset, but decreases very rapidly, and after one or two days only the weak emission from the halo remains, in agreement with VLBI observations.

The validity of the model depends on the flaring rate in these systems, which must be at least of one event per week in order to maintain the quiescent emission. In order to determine the frequency of flares, a monitoring program of UX Ari at the Effelsberg radiotelescope was started in December 1992 (Neidhöfer et al. 1993; Torricelli Ciamponi et al. 1995; Massi et al. 1996);

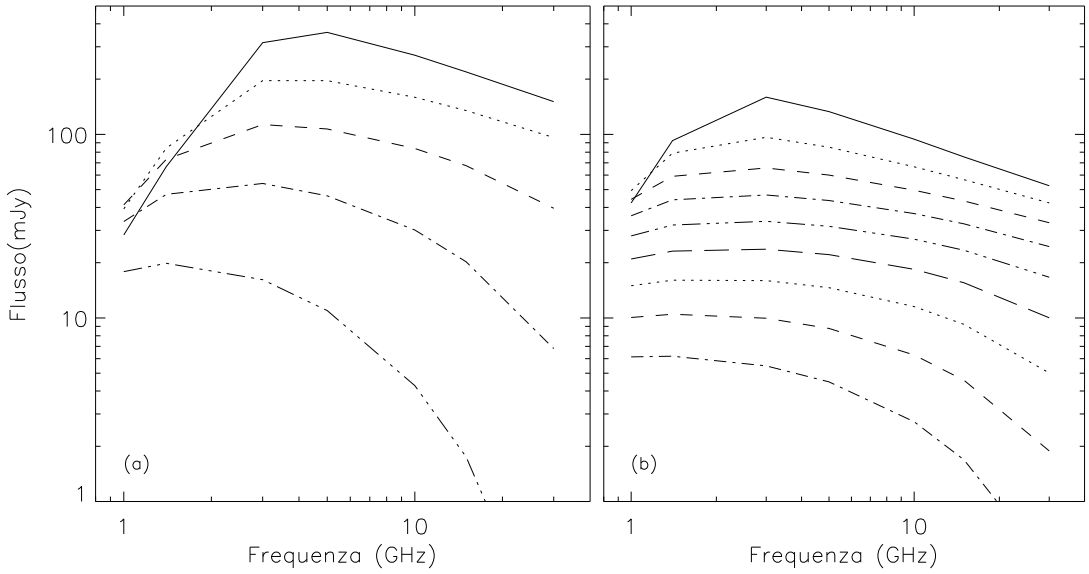

Fig. 2.4 Time evolution of the spectrum computed in the two cases $B = 10$ G (a) and $B = 5$ G (b), for $\delta = 2$, $n_e = 10^8$ cm^{-3}, $\theta = 45°$, and $N_o L = 10^{17}$ cm^{-2}. The spectrum for $t = 0$ is indicated with a solid line. The other spectra have been obtained, from top to bottom, at intervals of 1 day, from $t = 1^d$ to $t = 8^d$.

the observations are performed in the intervals between other scheduled observations, therefore they span a frequency range between 1.4 and 43 GHz, depending on the available receiver. These observations show that, although very strong flares ($F_\nu > 300$ mJy) are rather rare, medium- or low-energy flares (50 mJy $\leq F_\nu \leq 200$ mJy) are very often observed (Fig. 2.5). Similar results have been obtained during a monitoring program of HR 1099 at 5 GHz performed at the Noto radiotelescope since 1990 (Umana et al. 1995).

Since these observations confirm the assumption that electrons are accelerated episodically during flares, we decided to refine the model, including several effects that had been neglected in the simplified preliminary version. First, we will drop the assumption of a uniform magnetic field, assuming instead that the emission takes place in a magnetic loop; moreover, in the calculation of the distribution of relativistic electrons we will take into account also the particles leaving the source into the loss cone. We will then consider the influence of the coronal thermal plasma not only on the evolution of the particle distribution,

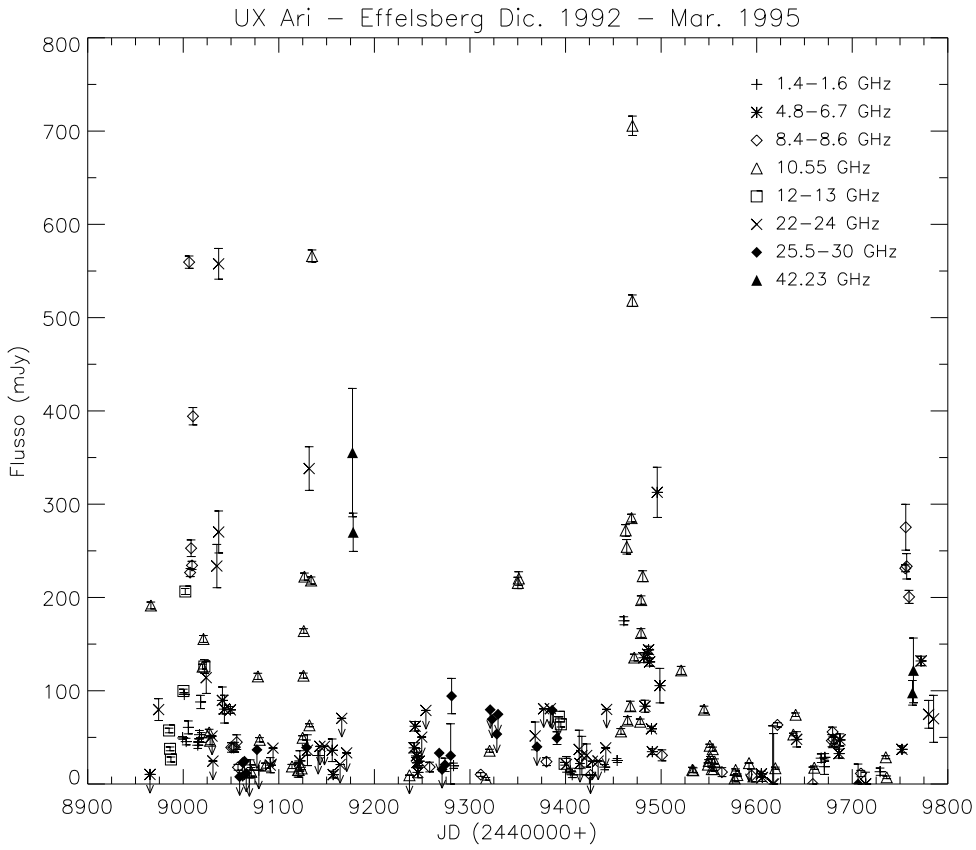

Fig. 2.5 Observations of UX Ari performed at the Effelsberg radiotelescope between December 1992 and March 1995 at variuos frequencies between 1.4 and 43 GHz (Neidöfer et al. 1993; Torricelli Ciamponi et al. 1995; Massi et al. 1996).

as in the preliminary model, but also on the emitted radiation, by including in the transfer equation both the thermal free-free emission and absorption and the Razin effect.

§ 2.4 Time evolution in a dipolar loop

We consider a source consisting of a magnetic loop which connects two starspots on the stellar surface. The loop is generated by a dipole lying on the plane of the sky and buried at a certain depth below the photosphere: the depth and the dipole strength are determined by imposing that the magnetic field in the centre of the spots is perpendicular to the stellar surface and has a given

value $B_{\max}$. In the following calculations we have adopted the value $B_{\max} =$ 1000 G, in agreement with observations (Giampapa et al. 1983; Gondoin et al. 1985; Donati et al. 1990, 1992). For the sake of simplicity, we assume that the loop is fixed on the plane of the sky, in spite of the stellar rotation; this is a very strong approximation, which we will drop later in Chapt. 4.

The studies on the starspot distribution on RS CVn systems (see Chapt. 1) show that typical spots have a radius $R_{\rm spot} \simeq 15^\circ - 25^\circ$, while their position varies greatly from one observation to the other. A variation of the angular separation of the spots causes a variation of the source surface and volume. Since the source is optically thin almost everywhere, except very close to the star, the only important geometrical parameter is its volume, which depends also on the starspot radius. In the following calculations we will consider an angular separation $\Theta = 60^\circ$ and $\Theta = 90^\circ$ between the centres of the two spots.

For the sake of simplicity and in order to reduce the computer time, we have assumed that the magnetic field varies only on the plane of the sky, and is constant along lines parallel to the line of sight. In the plane of the sky the loop is limited by the two lines of force passing through the borders of the starspots, while along the line of sight the source is assumed to have a triangular shape, as in the model by Klein & Chiuderi Drago (1987), with a semiaperture ϕ which is varied from $\phi = R_{\rm spot}$ to $\phi = 1.5\, R_{\rm spot}$, in order to have comparable sizes of the spots in the two directions. To avoid the problem due to the fact that the approximations (2.8) are not valid in a small interval around $\theta = 90^\circ$, we have considered a mean value $\theta = 85^\circ$ for the angle between the magnetic field and the line of sight. A sketch of the source structure on the plane of the sky is shown in Fig. 2.6.

The source volumes corresponding to our choice of the parameters are shown in Tab. 2.1. The spot radius has been limited to 20° because in the case $\Theta = 90^\circ$ a radius of 25° would give a loop surface one order of magnitude larger than the whole binary system, and in the case $\Theta = 60^\circ$ the spot separation would be too small in comparison to their sizes.

The total number density of relativistic electrons $N_{\rm tot} = N_\circ\, V$ has been chosen in order to reproduce a flux density of the order of $100 - 150$ mJy at

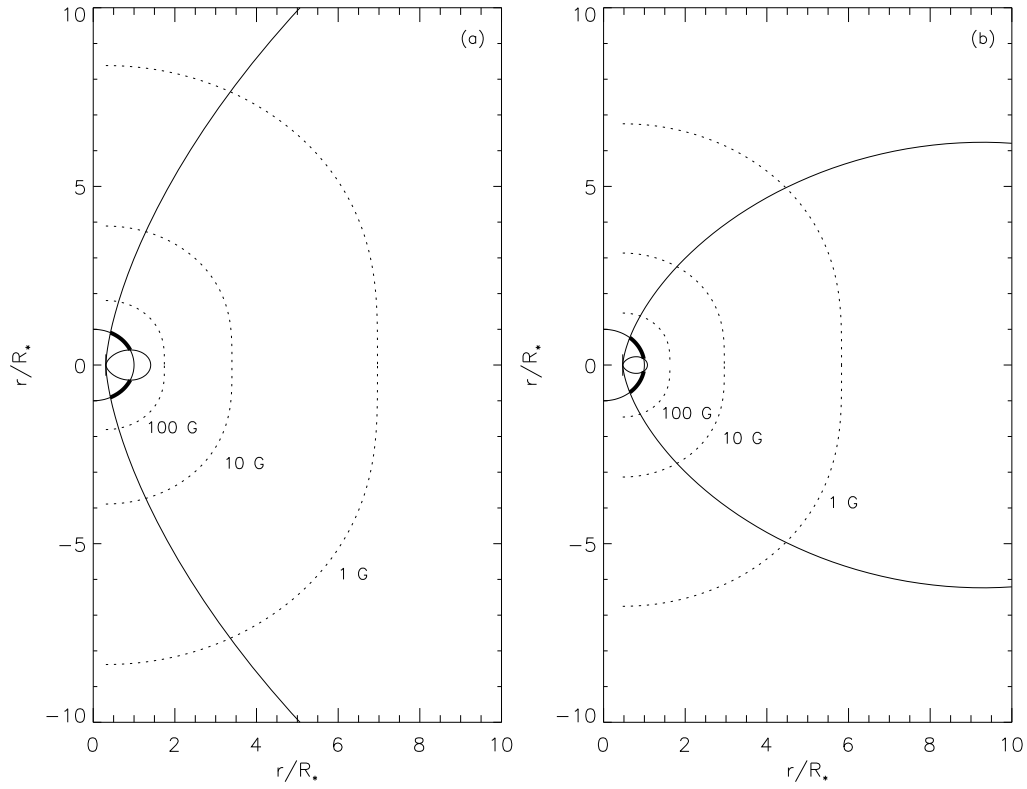

Fig. 2.6 Sketch of the source in the plane of the sky. The starspots are marked as thick arches: $R_{\rm spot} = 20°$ and the separation between the centres is $\Theta = 90°$ (a) and $\Theta = 60°$ (b). The source is limited by the solid lines; dotted lines represent the levels of constant B, having assumed $B_{\rm max} = 1000$ G

15 GHz, which is the most commonly observed value during active periods. All calculations are referred to the distance of the system UX Ari, $d = 50$ pc.

The loop is filled with a thermal plasma with temperature $T = 1.5 \times 10^7$ K, in agreement with the mean value of the hot component temperatures derived from recent X-ray observations (Dempsey et al. 1993). The thermal plasma density $n_{\rm e}$ has been assumed uniform within the source and left as a free parameter. Although the magnetic structure in the stellar corona may generate consistent density inhomogeneities between different loops, our approximation of a constant density within the same magnetic loop is not significantly different from the real situation. In fact, assuming that the electron density in the loop is distributed according to hydrostatic equilibrium, it decreases to $0.7 n_\circ$ at $R = 10\, R_\star$, where $n_\circ$ is the density at the stellar surface, and then it remains almost constant. The presence of the companion, if it is on the same side of

Tab. 2.1 Source volume as a function of the starspot size $R_{\rm spot}$ and ϕ and of the angular separation Θ

$R_{\rm spot}$ (°)	ϕ (°)	Volume (cm^3)	
		$\Theta = 60°$	$\Theta = 90°$
15	15.0	1.30×10^{36}	2.34×10^{37}
	22.5	2.01×10^{36}	3.61×10^{37}
20	20.0	1.88×10^{37}	9.57×10^{38}
	30.0	2.97×10^{37}	1.52×10^{39}

the loop, as well as the rotation of the system, make the density decrease even more slowly.

As in the preliminary case of the previous section, the initial electron energy distribution is assumed to be an isotropic power-law with esponent $\delta = 2$ and $\delta = 3$, defined for $\gamma_{\circ 1} \leq \gamma_\circ < \infty$, with $\gamma_{\circ 1} = 1.1$, which evolves in time due to radiation and collision energy losses. It is also assumed that electrons are accelerated at $t = 0$ uniformly over the whole loop; this hypothesis is justified by the fact that, even if electrons are injected in a certain point of the loop, the time needed to fill the entire loop volume is negligible with respect to the characteristic timescales of the flare decay. The presence of a converging magnetic field, however, causes a leak from the emitting region of electrons with small pitch angle, that penetrate deeper in the stellar atmosphere where they rapidly lose their energy. This phenomenon causes an anisotropy in the energy distribution; however, due to collisions with protons of the thermal plasma, the distribution becomes isotropic again in a characteristic time (Spitzer 1962):

$$\tau_{\rm d} \simeq 3.11 \times 10^{-20} \, \frac{v^3}{n_{\rm e}} \sim \frac{8.4 \times 10^{11}}{n_{\rm e}} \, \beta^3 \tag{2.20}$$

where $\beta = v/c$. The number of particles with energy γ escaping from the source into the loss-cone per unit time can be estimated as:

$$\left(\frac{dN}{dt} \right)_{\rm lc} = - \, \frac{\Omega_{\rm lc}}{4\pi} \, \frac{N(\gamma, t)}{\tau_{\rm d}} = - \, \frac{(1 - \cos \psi_\circ)}{2 \, \tau_{\rm d}} \, N(\gamma, t) \, , \tag{2.21}$$

where $\Omega_{\rm lc} = 2\pi\,(1 - \cos\psi_\circ)$ is the loss-cone solid angle, and:

$$\cos\psi_\circ = \sqrt{1 - \frac{B}{B_{\rm max}}}\,, \tag{2.22}$$

where B is the local magnetic field. In this case, Eq. (2.1) becomes:

$$\frac{\partial N(\gamma,t)}{\partial t} + \frac{\partial}{\partial\gamma}\left[\frac{d\gamma}{dt}\,N(\gamma,t)\right] = -\,\frac{(1-\cos\psi_\circ)}{2\,\tau_{\rm d}}\,N(\gamma,t)\,. \tag{2.23}$$

If we substitute β with an average value over the initial energy distribution, so that $\tau_{\rm d}$ becomes constant, from Eq. (2.2) we obtain:

$$N(\gamma,t) = N(\gamma_\circ,0)\,\frac{{\rm d}\gamma}{{\rm d}\gamma_\circ}\,{\rm e}^{-(1-\cos\psi_\circ)\,t/2\tau_{\rm d}}\,. \tag{2.24}$$

The distribution $N(\gamma,t)$ therefore has the same shape as Eq. (2.15) with an additional exponential term. For electrons with $\beta \simeq 1$ and the values of the parameters adopted in this chapter, the loss-cone effect is always very small, and the evolution of the distribution is not significantly different from the previous case. In the case of mildly-relativistic electrons, that have a lower mean value of β, the exponential term can reduce substantially the number of particles at a given time, causing a more rapid decay of the flare.

As mentioned in the previous paragraph, the presence of the thermal plasma has been taken into account also in the calculation of the emitted radiation, including in the model both the thermal free-free emission and absorption and the Razin effect. In our assumption of a uniform density the Razin effect, which strongly suppresses the radiation at frequencies $\nu \lesssim 20\,n_{\rm e}/B$, becomes very important at great distances from the active star, where the magnetic field is low. In order to take this effect into account, the complete expression of the emissivity and absorption coefficient (Eq. (2.8)) in a medium with $n_\pm \neq 1$ must be considered. The free-free emission and absorption appear instead as additional terms in the transfer equation.

§ 2.5 Comparison with observations

The radio spectra of RS CVn systems available in the literature show a large variety of intensity and spectral trends. Since there are no spectral observations

carried out several times during the same flaring event, a direct comparison of the computed spectra with the observed ones will not give any useful information on the model parameters, in particular on the spectral index δ, the loop volume and the thermal plasma density.

In spite of the large variety of observations, Mutel et al. (1987) have shown the existence of a very good correlation between the logarithm of the observed luminosity relative to the average one, $L_{\rm R}/\langle L_{\rm R}\rangle$, at 5 GHz, and the spectral index α measured between 1.4 and 5 GHz (see Fig. 1.3a). Considering also the relation obtained from other recent observations (Fig. 1.3b), we see that, although a certain scattering is present, not a single data point falls in the lower right or in the upper left corner of the diagram. More precisely, it happens that, for the totality of the observations, $\log(L_{\rm R}/\langle L_{\rm R}\rangle)$ must be larger than $1.31\alpha - 1.1$ and smaller than $1.31\,\alpha + 0.64$.

The Mutel et al. plot of the $\log(L_{\rm R}/\langle L_{\rm R}\rangle)$ vs. α correlation is shown in Fig. 2.7 together with some of the curves obtained from our model: each curve was obtained by calculating the luminosity and spectral index at different times, and each curve differs from the others in the initial parameters. The adopted value of the mean radio luminosity, $\langle L_{\rm R}\rangle = 5 \times 10^{16}$ erg sec^{-1} Hz^{-1}, has been obtained by averaging the luminosities of the stars listed in Tab. 3 of Drake et al. (1989).

The curves shown in Fig. 2.7 have been obtained, for each value of the exponent δ of the initial energy distribution, assuming $\Theta = 90°$ and $\phi = R_{\rm spot} = 20°$, and changing the total number of relativistic electrons and the thermal plasma density. A variation of the first parameter, $N_{\rm tot} = N_\circ V$, rigidly shifts the curves in the vertical direction if the radiation is optically thin at both frequencies (1.4 and 5 GHz), leaves them unchanged in the region where they are both optically thick and shifts the points in the upper right direction (increasing both L and α) in the case when the radiation is optically thin at 5 GHz and thick at 1.4 GHz. We can therefore conclude that no sensible variations in the shape of the curves shown in Fig. 2.7 are obtained by varying $N_{\rm tot}$. Upper and lower limits of $N_\circ$, inferred from the observations, are $5 \times 10^3 \leq N_\circ \leq 2 \times 10^4$ for $\delta = 2$ and $3 \times 10^5 \leq N_\circ \leq 1 \times 10^6$ for $\delta = 3$.

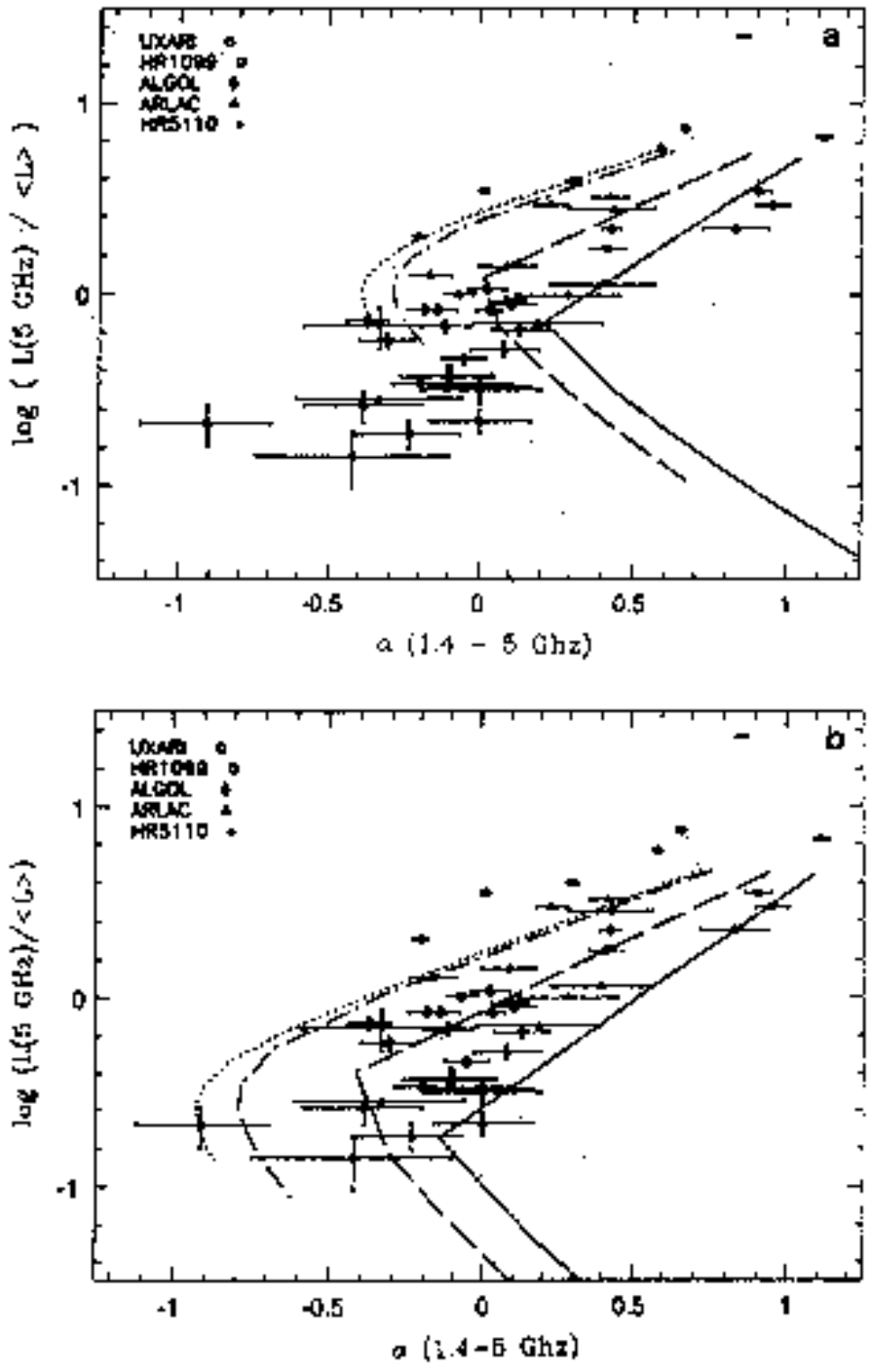

Fig. 2.7 Comparison of the computed relationship $\log(L_{\rm R}/\langle L_{\rm R}\rangle)$ vs α with the observed data points given by Mutel et al. (1987). The curves have been obtained assuming $R_{\rm spot} = \phi = 20°$, $\Theta = 90°$ in the two cases $\delta = 2$, $N_{\rm o} = 10^4$ cm^{-3} (a) and $\delta = 3$, $N_{\rm o} = 6 \times 10^5$ cm^{-3} (b). Different curves correspond to thermal densities $n_{\rm e} = 10^8$ cm^{-3} (solid line), 5×10^7 cm^{-3} (dashed line), 10^7 cm^{-3} (dash-dotted line) and 5×10^6 cm^{-3} (dotted line).

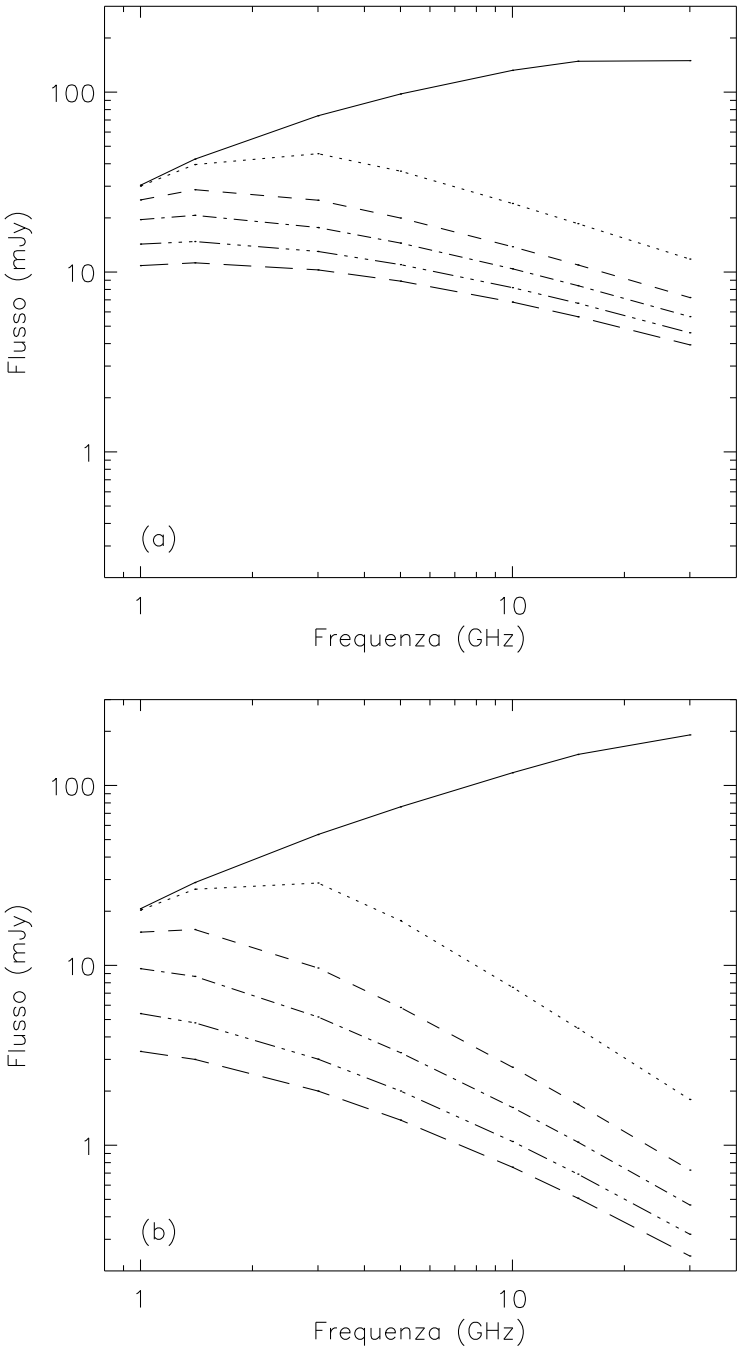

Fig. 2.8 Radio spectra obtained assuming $n_e = 10^7$ cm^{-3}, $\Theta = 90°$, $R_{spot} = \phi = 20°$, in the two cases $\delta = 2$, $N_\circ = 10^4$ cm^{-3} (a) and $\delta = 3$, $N_\circ = 6 \times 10^5$ cm^{-3} (b). The curves represent the flare spectrum for $t = 0$ (solid line) and, from top to bottom, that emitted after 2, 6, 10, 15, 20 days.

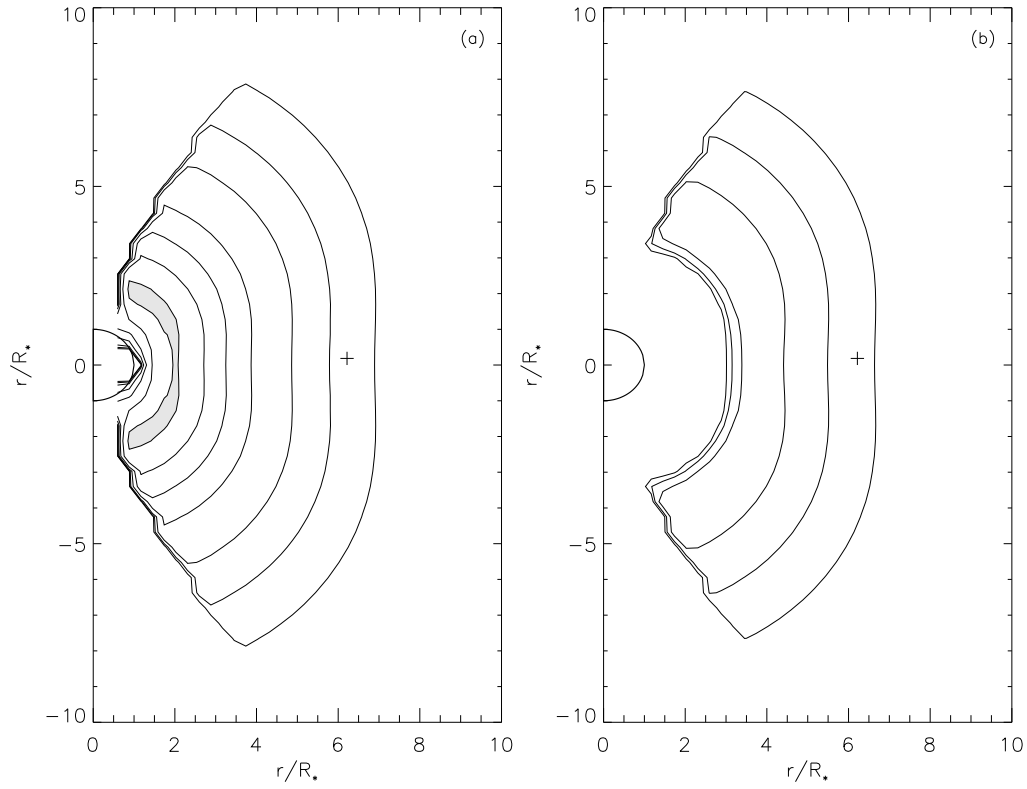

Fig. 2.9 Brightness distribution of the source at $\nu = 5$ GHz, computed at the flare onset (a) and after 6 days (b), assuming $\delta = 2$, $R_{\rm spot} = \phi = 20°$ and $\Theta = 90°$. Intensity contours are at 5×10^{-10}, 10^{-9}, 2×10^{-9}, 5×10^{-9}, 10^{-8}, 2×10^{-8} and 4×10^{-8} erg cm^{-2} sec^{-1} Hz^{-1} sr^{-1}. The highest brightness contour has been shadowed for the sake of clarity. The cross indicates the distance of the companion when the system is in quadrature.

The influence of the thermal electron density on the considered correlation is instead very important since it drastically changes the slope of the curves at low frequency; we see in fact from Fig. 2.7 that a thermal electron density in excess of 10^7 cm^{-3} causes the reversal of the curves toward the bottom right corner, in clear conflict with the observations. A variation of the parameters Θ, ϕ and $R_{\rm spot}$, leaving $n_{\rm e}$ and $N_{\rm tot}$ unchanged, does not sensibly affect the shape of the curves.

The radio spectra obtained during the flare ($t = 0$) and at different times after it are shown in Fig. 2.8 for $\delta = 2$ and $\delta = 3$. The loop parameters are the same of Fig. 2.7 and a thermal plasma density $n_{\rm e} = 10^7$ cm^{-3} has been assumed.

As far as the parameter δ is concerned, we notice that the spectra obtained

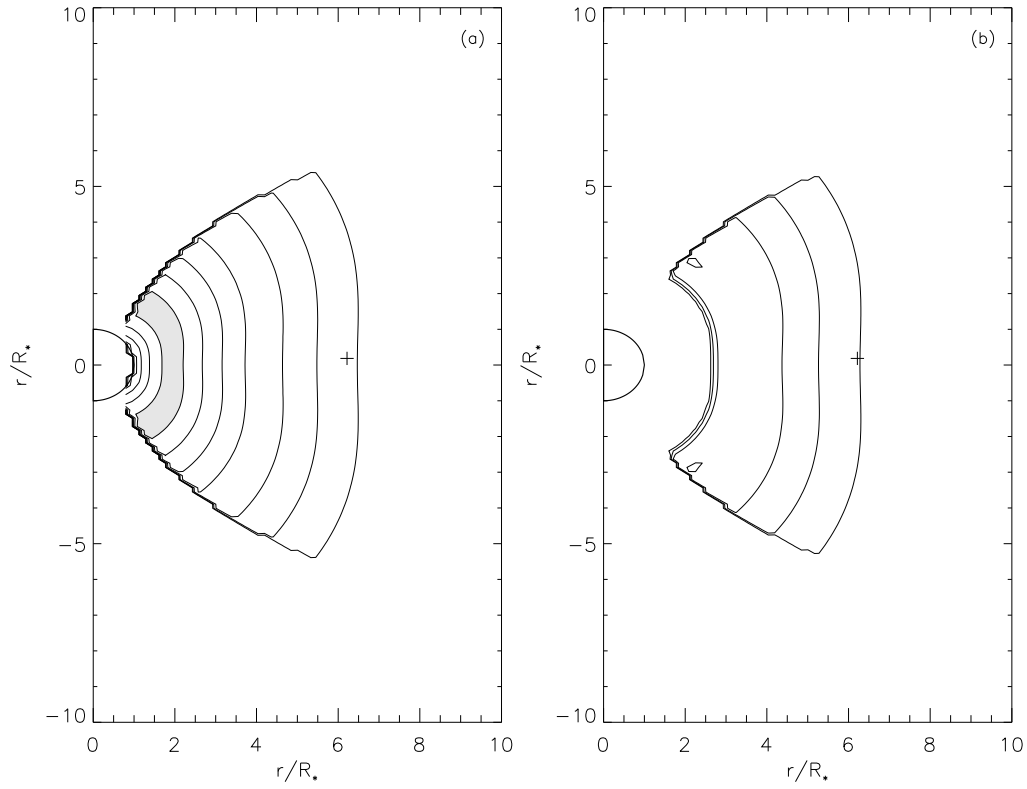

Fig. 2.10 Same as Fig. 2.9 but with a spot separation $\Theta = 60°$.

assuming $\delta = 3$ satisfy the $\log(L_{\rm R}/\langle L_{\rm R}\rangle)$ vs. α correlation in a wider range of parameter values, but that a much larger number density of relativistic particles is required to reproduce the observed flux density. Another important difference is noticed in the lifetime of the emitted radiation, which decreases much faster for $\delta = 3$. Although the available data do not allow a discrimination between the two values, the choice $\delta = 2$ appears more reasonable for energetic reasons.

Using again the same loop parameters and $\delta = 2$, we have computed the brightness distribution of the radio source at 5 GHz during the flare ($t = 0$) and six days later. The derived maps are shown in Fig. 2.9 for $\Theta = 90°$ and in Fig. 2.10 for $\Theta = 60°$. The parameter Θ is in fact the one which mostly affects the source size.

Figs. 2.9 and 2.10 show that the brightness distribution far from the star ($R > 4\,R_\star$) does not change much with time, while the much brighter region (about a factor of 40) present at a distance $R \simeq 2R_\star$ at $t = 0$ disappears in a few

days. These results, which do not appreciably change if $\delta = 3$ is assumed, agree very well with the assumption of a core-halo to halo evolution of the source structure.

The model therefore reproduces very well the characteristics of RS CVn spectra as well as the evolution of the source from a core-halo to a halo structure. This evolution was implicitly present also in the preliminary model, although the assumption of a constant magnetic field within the source made it impossible to show it in a quantitative way, and is completely in agreement with VLBI observations carried out in different epochs (Mutel et al. 1984, 1985; Lestrade et al. 1984a, 1984b, 1988; Little-Marenin et al. 1986; Massi et al. 1988; Trigilio et al. 1993, 1995). Further support to the model could come from observations of both the spectrum and the source structure during the decay phase of a flare, in order to evidentiate the temporal variations. Such observations, unfortunately not yet available, could give important informations on the physical characteristics of the source.

§ 2.6 Possible cospatiality of the X-ray and radio emission

As mentioned in Chapt. 1, although the X-ray and radio emission observed in RS CVn systems have different origins (synchrotron emission from non-thermal particles in the radio band, emission from a population of thermal electrons in the X-ray band), the luminosities observed in the two bands are strongly correlated (Drake et al. 1989, 1992; Dempsey et al. 1993). In two recent papers, Güdel & Benz (1993) and Benz & Güdel (1994) have shown that this correlation is not limited to RS CVn systems, but is valid for different types of stars and also for solar flares, extending with nearly the same slope over several orders of magnitude. According to these authors, the interpretation of this remarkable correlation must be searched in the primary process of energy release (magnetic reconnection?), where a relationship must exist between the energy spent to heat the plasma and the energy which goes into accelerating the particles, and therefore also between the X-ray and radio emissions. As we said in Chapt. 1, X-ray observations show that the hot component of the

coronal plasma is extended over dimensions comparable to the binary system, like the radio emission (Swank et al. 1981; White et al. 1990a); it is therefore interesting to exhamine the possibility of a cospatiality of the X-ray and radio emission.

The $\log(L_{\rm R}/\langle L_{\rm R}\rangle)$ vs. α plot shown in the previous section puts a very strict constraint on the thermal plasma density in the source, which cannot be larger than 10^7 cm^{-3} independently of the other parameters. Such a constraint can be used for a comparison with the emission measures derived from X-ray observations of RS CVn systems. The emission measures of the hot component span from 2×10^{52} cm^{-3} to 3×10^{54} cm^{-3} (Dempsey et al. 1993). A maximum thermal density of 10^7 cm^{-3} would imply a source volume $V \geq 2 \times 10^{38} - 3 \times 10^{40}$ cm^3. According to Tab. 2.1, a volume of the order of 10^{39} cm $^{-3}$ is obtained assuming the following values for the loop parameters:

$$\Theta = 90^\circ\ , \quad R_{\rm spot} \simeq 20^\circ\ , \quad 20^\circ \leq \phi \leq 30^\circ\ .$$

Therefore the constraints on the thermal plasma density derived from the $\log(L_{\rm R}/\langle L_{\rm R}\rangle)$ vs. α correlation are not in clear conflict with a possible cospatiality of the X-ray and radio emission, although the upper limit of the required volume is about one order of magnitude larger than the maximum volume assumed in this paper for the radioemitting loop. Of course an agreement between the radio and X-ray emitting volumes can still be achieved with a smaller starspot separation, if larger values for the starspot radius $R_{\rm spot}$ or for the angle ϕ are assumed.

It must be pointed out that the influence of the thermal plasma on the low-frequency radio spectrum through free-free absorption and Razin effect does not depend on this particular model. The derived constraint on the thermal electron density has therefore a very general validity. On the other hand, the remarkable correlation between the X-ray and radio luminosities does not necessarily imply that the electrons emitting in the two frequency bands must be cospatial in the same loop. In the case of solar flares, for instance, it is believed that the same process is responsible for the acceleration of energetic particles emitting gyrosynchrotron radiation in the radio spectrum and of those that, stopped

in the lower and denser layers of the atmosphere, produce the plasma heating and the consequent enhancement of the X-ray emission. Although strongly correlated, the two emissions take place in different portions of the loop.

CHAPTER 3

INTERPRETATION OF THE RISING PHASE OF FLARES

§ 3.1 Introduction

In the previous chapter we have developed a time-dependent model of the radio emission in order to interpret the quiescent component as the final phase of a flare decay; for this reason the model considered only the evolution of the emission due to energy losses, neglecting the rising phase which, for the timescales of interest, could be considered instantaneous. However the flare rising phase is important, being linked to the particle acceleration mechanism and thus to the energy release in the source. Until some time ago the only available data on the rising phase were observations of light curves at a single frequency, showing that this phase has a typical duration of a few hours; recently, however, some spectra have been obtained at Effelsberg which are clearly associated with an increase in the radio flux density and therefore can be attributed to the initial phase of a flare.

In this chapter we will therefore study the evolution of the radio emission during the rising phase of flares, introducing in our model a constant injection of relativistic electrons: the addition of this term constrasts the effect of energy losses, allowing an increase of the emission with time. We will consider for the source structure a magnetic loop similar to that of the previous chapter, assuming that electrons are accelerated at the top and then fill rapidly the entire loop; in this case, as we will see later, we obtain an energy distribution which

is no longer homogeneous, but depends on the position inside the loop.

§ 3.2 Observations of flare spectra during the rising phase

During the monitoring program of UX Ari performed at the Effelsberg radiotelescope some flare spectra were obtained, which can be attributed to the initial rising phase, since the corresponding data indicate an increase of the flux density over a timescale of the order of a few hours (Torricelli Ciamponi et al. 1995). These spectra are shown in Fig. 3.1, together with the other single-frequency observations performed during the same time intervals. Data referring to different orbital phases are indicated with different symbols, and a phase difference of 0.01 corresponds to about 1.5 hours.

Since the emission can increase only if an energy supply, in form of accelerated particles, is present, the timescale of the flux density increase gives an idea of the duration of the acceleration mechanism. From the observations shown in Fig. 3.1 we infer that the particle acceleration can last for a long time, up to two days; the data, however, have been sampled at long time intervals, therefore we cannot exclude the possibility that the observed increase of the flux density is not due to a single long-lasting particle acceleration, but the particles are accelerated in a succession of shorter-duration bursts. Since we do not have the possibility of determining, from the available data, the real structure of these flares on shorter timescales, we will consider each of them as single events.

The observations show that the spectral index α of the radiation received from UX Ari is positive between 1.4 and 10 GHz, except for flare 4 where $\alpha > 0$ only up to 5 GHz. The measured values of α are different from flare to flare and vary with time during the same flare, ranging from 0.31 to 0.73 in the frequency range $2.7-5$ GHz, and from 0.13 to 0.38 in the range $5-10.5$ GHz (-0.11 in the case of flare 4). These values agree with the spectral indexes measured in the spectra of other RS CVn systems, that, between 1.4 and 5 GHz, vary between $\alpha = -0.7$ and $\alpha = 1$ (Mutel et al. 1987), with higher values referring to higher luminosity periods. The fact that all spectra in Fig. 3.1 show positive spectral indexes at frequencies below 5 GHz implies that this is a characteristic of the

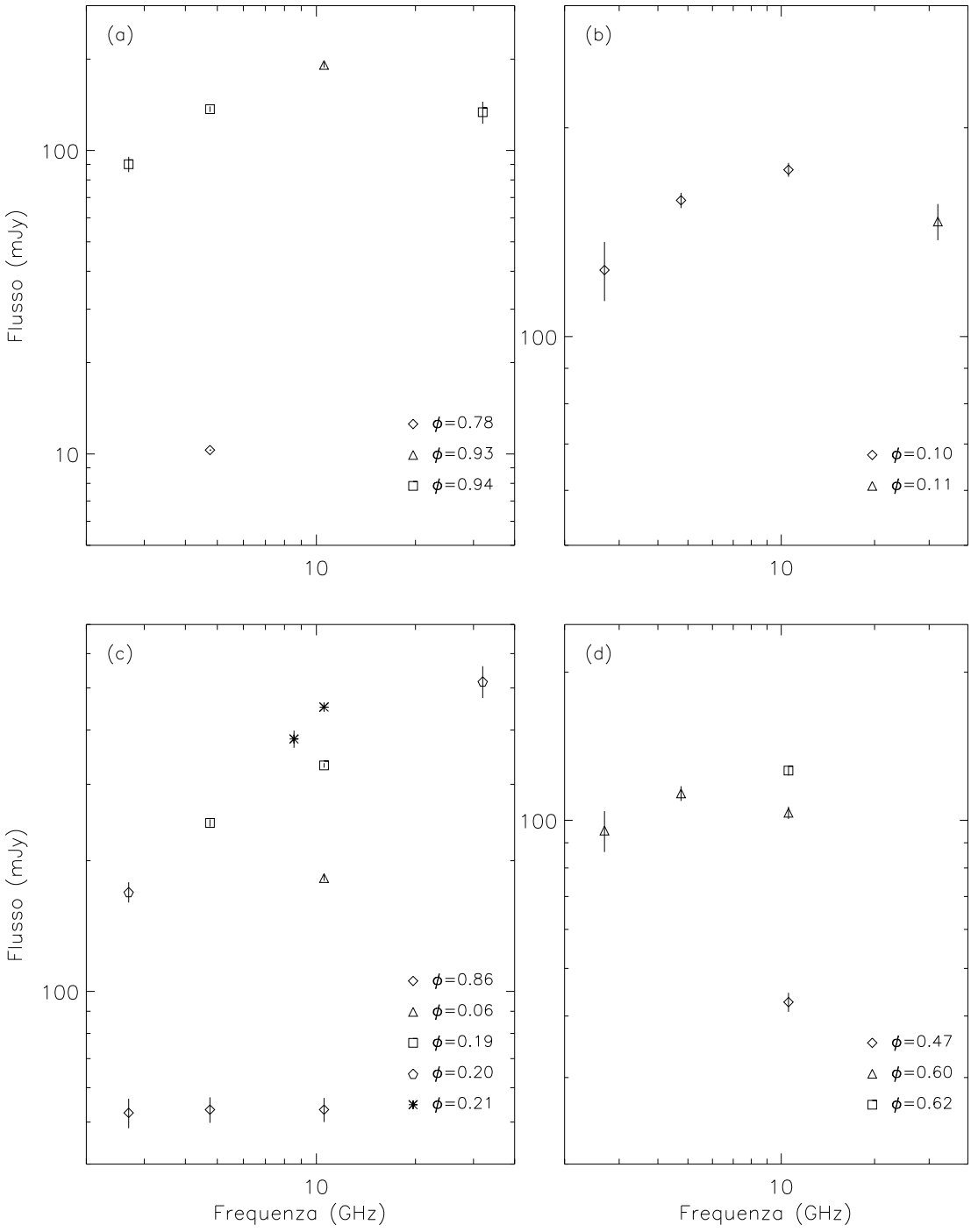

Fig. 3.1 Spectra observed at different times for four flares during the rising phase. (a) Flare 1: $\phi = 0.78$ corresponds to JD 2448965.170; (b) Flare 2: $\phi = 0.10$ corresponds to JD 2449462.930; (c) Flare 3: $\phi = 0.86$ corresponds to JD 2449467.790; (d) Flare 4: $\phi = 0.47$ corresponds to JD 2449478.160.

flare rising phases. In fact, as shown in Chapt. 2, during the decay phase the spectral peak shifts towards lower frequencies and the spectral slope changes sign becoming negative at these frequencies.

The common interpretation for spectra with a positive spectral index at radio wavelengths is synchrotron self-absorption. The values of α measured for UX Ari are however lower than the canonical slope for gyrosynchrotron emission from an optically thick homogeneous source, which is approximately given by $\alpha = 2.5 + 0.085\,\delta$ (Dulk 1985). The evolution of the distribution due to energy losses cannot explain the observed spectra, since this mechanism makes the spectrum optically thin, as shown in the previous chapter; moreover, this difference is found also when the flux density is increasing, i.e. during the rising phase where the spectral features depend not only on energy losses but also on the injection of new particles. However, it is possible to reproduce the spectral indices $\alpha < 2.5$ observed during flares by assuming that the emission originates in an inhomogeneous source. In fact, as we said in Chapt. 1, this hypothesis was successfully used to reproduce the spectrum of the February 1978 flare on HR 1099 in two opposite cases: a constant magnetic field with a varying density of relativistic electrons (Borghi & Chiuderi Drago 1985), and a dipolar magnetic field with uniform density (Klein & Chiuderi Drago 1987). In the next section we will show that, in a realistic magnetic configuration, during the phase of particle injection the electrons distribute themselves inside the loop with a density which is no more uniform, but depends on the position in the source.

§ 3.3 Energy distribution of relativistic electrons during the flare rising phase

The geometry of the region where the energy production, and therefore the particle acceleration, takes place is not known, although the emission properties suggest the presence of loop-like magnetic structures analogous to those present in the solar corona. Since relativistic electrons stream along magnetic field lines, their density will be distributed in the source in a way strictly related to the field configuration; however, this distribution can be strongly affected by the

presence of energy losses. In the case of mildly-relativistic electrons, collision losses have a typical timescale $t_{\rm coll} \sim 10^9/n_{\rm e}$ hours, while for synchrotron losses $t_{\rm sinc} \sim 10^4/B^2$ hours. The values of the magnetic field range from $\sim 1 - 10$ G in the corona to ~ 1000 G at photospheric level, while the small gravitational scale height implies an almost constant thermal density (Massi & Chiuderi Drago 1992) with $n_{\rm e} \sim 10^7 - 10^8$ cm^{-3}. Hence, while collision losses will influence the emission in the same way everywhere in the loop on timescales of the order of $1 - 2$ days, synchrotron losses will strongly suppress the radiation from the regions closer to the photosphere in a few minutes after the flare onset, but will affect the radiation from the outer regions only after some hours. Since different regions of the source contribute to the emission at different frequencies, the different efficiency of energy losses in different parts of the loop strongly affects the spectral shape already after a few minutes from the beginning of the acceleration. These considerations imply that radiative losses must be taken into account even during the rising phase, in which a large amount of new relativistic particles is injected in the source.

For the sake of simplicity, we assume that the magnetic configuration is perfectly symmetric with respect to the loop axis, and that electrons are injected at the top, uniformly and isotropically over the entire central section of the loop, at a rate $\hat{Q}(\gamma, t)$ el. cm^{-3} sec^{-1}; in any case, even if the particles were accelerated predominantly in one direction, the electron distribution would become isotropic in a short time due to collisions with the protons of the thermal plasma (see Chapt. 2).

The time needed for the relativistic electrons to fill the loop, $t_{\rm din} \sim L/c$ (L = loop length), is very short ($\sim$ 7 sec if $L \sim R_\star$ and $\sim$ 1 min if L is comparable to the size of the binary system). Therefore the electrons diffuse rapidly from the acceleration site to the entire magnetic loop, reaching in a very short time a spatially symmetric distribution with respect to the loop axis. From our point of view, the attainment of this spatial distribution can be considered instantaneous since, for the moment, we have no way of investigating this short transient phase. These considerations could led us to think that electrons are distributed uniformly in the loop; as we will see, however, the presence of an

inhomogeneous magnetic field influences the final distribution, causing it to depend on the position inside the loop.

We describe the magnetic field using polar coordinates (r, ϕ), where $\phi = 90°$ corresponds to the injection region. Electrons stream along the field lines, and therefore, for the continuity equation, the number of electrons crossing a given section of a magnetic flux tube must be constant. This implies that the particle density at a given point (r, ϕ) is proportional to that at the injection site through a factor $A(\phi = 90°)/A(\phi)$, which takes into account the variation of the loop section. From the conservation of magnetic flux ($\nabla \cdot B = 0$) we have then:

$$\frac{A(90°)}{A(\phi)} = \frac{B(r,\phi)}{B(r,90°)} , \tag{3.1}$$

and therefore the density in the point (r, ϕ) is proportional to the corresponding magnetic field.

On the other hand, each of the electrons accelerated at $\phi = 90°$ streams downward along a magnetic field line until its initial pitch angle $\psi_\circ$ satisfies the relation

$$\sin^2 \psi_\circ = \frac{B(r,90°)}{B(r,\phi)} . \tag{3.2}$$

At this location the electron is reflected and begins to oscillate between this point and the symmetric mirror point until it loses all its energy by radiation or collisions. Hence, each position in the loop, identified by the corresponding value of the magnetic field $B(r, \phi)$, can be associated to the value of the initial pitch angle $\psi_\circ$ of those electrons that are reflected at that point. Electrons with $\psi < \psi_\circ$ continue their way towards the stellar surface, while those with $\psi > \psi_\circ$ are trapped in the region above that location and contribute to increase the density around the loop top. If we consider a generic section of the loop, the mirror mechanism reduces the number of particles in a small volume below that layer by the fraction:

$$\frac{\int_0^{\psi_\circ} \sin\psi \, \mathrm{d}\psi}{\int_0^{\pi} \sin\psi \, \mathrm{d}\psi} = 1 - \cos\psi_\circ . \tag{3.3}$$

Taking both these mechanisms into account, Eqs. (3.1) and (3.3) imply that at a given position (r, ϕ) the distribution of injected electrons has the

form:

$$Q(\gamma,t,r,\phi) = \hat{Q}(\gamma,t)\,\left(1-\sqrt{1-\,\frac{B(r,90^\circ)}{B(r,\phi)}}\,\right)\,\frac{B(r,\phi)}{B(r,90^\circ)}\,. \qquad (3.4)$$

We stress again that this expression does not take into account the time necessary for electrons to fill the entire loop, and, moreover, it is correct only if $\hat{Q}$ does not change in time, i.e. only if $\hat{Q}(\gamma,t) \equiv \hat{Q}(\gamma)$. However it can be considered a good starting point for deriving the spatial distribution of electrons trapped in a magnetic loop at a given time after injection.

In the case of particle injection plus energy losses, Eq. (2.1), which describes the time evolution of the energy distribution, takes the form:

$$\frac{\partial N(\gamma,t,r,\phi)}{\partial t} \;+\; \frac{\partial}{\partial\gamma}\left[\frac{\mathrm{d}\gamma}{\mathrm{d}t}\,N(\gamma,t,r,\phi)\right] = Q(\gamma,r,\phi)\,, \qquad (3.5)$$

and the general solution (2.2) becomes:

$$N(\gamma,t,r,\phi) = N(\gamma_\circ,0,r,\phi)\,\frac{\partial\gamma_\circ}{\partial\gamma} \;+\; \frac{1}{|\mathrm{d}\gamma/\mathrm{d}t|}\,\int_\gamma^{\gamma_\circ} Q(\gamma^{\,\prime},r,\phi)\,\mathrm{d}\gamma^{\,\prime}\,. \qquad (3.6)$$

The complete expression of the energy distribution at time t is obtained by carrying out the integral in Eq. (3.6) and substituting the relation (2.7) between $\gamma_\circ$ and γ and the expression (2.6) for $\mathrm{d}\gamma/\mathrm{d}t$. We assume that both the injected energy distribution $Q(\gamma,t,r,\phi)$ and the initial distribution $N(\gamma_\circ,0,r,\phi)$ have the same dependence on the position (r,ϕ) along the loop, given by Eq. (3.4), and the same dependence on energy, described by a power-law, with:

$$\begin{aligned} \hat{N}(\gamma_\circ,0) &= K_\circ\,(\gamma_\circ-1)^{-\delta}\,, \qquad & \gamma_{\circ 1} \le \gamma_\circ \le \infty\,; \\ \hat{Q}(\gamma,t) &= Q_\circ K_\circ\,(\gamma-1)^{-\delta}\,, \qquad & \gamma_{\circ 1} \le \gamma \le \infty\,. \end{aligned} \qquad (3.7)$$

In these expressions $K_\circ = N_\circ\,(\delta-1)\,(\gamma_{\circ 1}-1)^{\delta-1}$ and $N_\circ$ is the total density of relativistic electrons at the loop top ($\phi = 90^\circ$) at $t = 0$. We can interpret this term as a residual population from a previous flare: in this case, however, as seen in Chapt. 2, its form cannot be considered anymore that of a power-law. However, since we do not have any information on the time elapsed from the previous flare, and hence on the true shape of the residual distribution, we have assumed a power-law for the sake of simplicity. The total density of particles

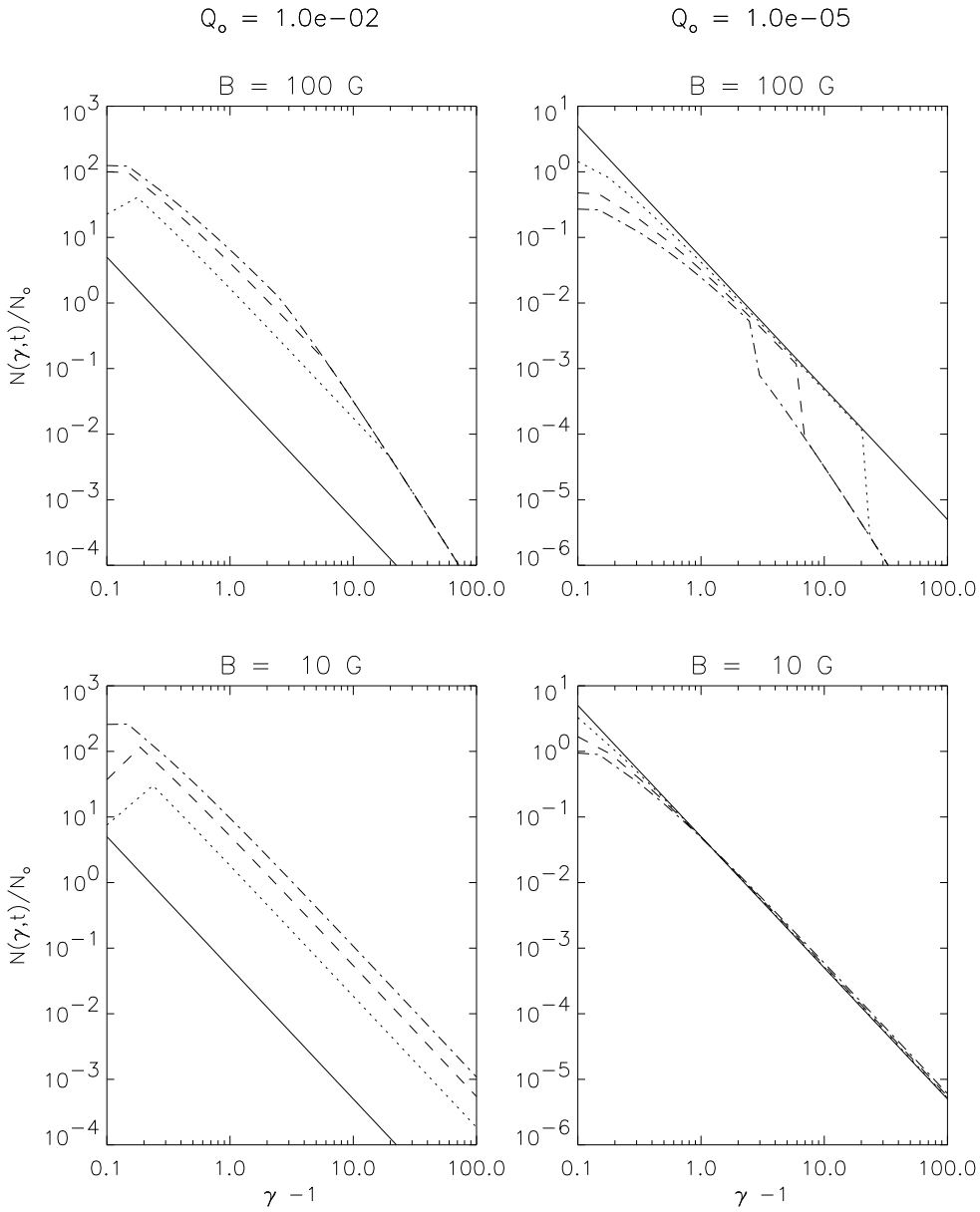

Fig. 3.2 Variation with time of the energy distribution, in the case $\delta = 2$, $\gamma_{o1} = 1.1$, $B(r, 90°) = 0.1$ G, $n_e = 10^7$ cm^{-3}, in two regions of the loop where $B = 100$ G and $B = 10$ G. The distribution has been computed assuming $Q_o = 10^{-2}$ sec^{-1} (left) and $Q_o = 10^{-5}$ sec^{-1} (right). The distribution is shown for $t = 0$ (solid line), 1^h (dotted line), 3^h (dashed line) and 6^h (dot-dashed line).

injected in the source per unit time at the loop top is therefore $Q_o\, N_o$. The result of the integral $I = \int_{\gamma}^{\gamma_o} \hat{Q}(\gamma')\, d\gamma'$ in Eq. (3.6) depends on the value of γ: since at a given time t the distribution $N(\gamma, t, r, \phi)$, due to energy losses, is defined for $\gamma \geq \gamma_1(\gamma_{o1}, t)$, while $Q(\gamma, t, r, \phi)$ is defined only for $\gamma \geq \gamma_{o1} > \gamma_1$, we

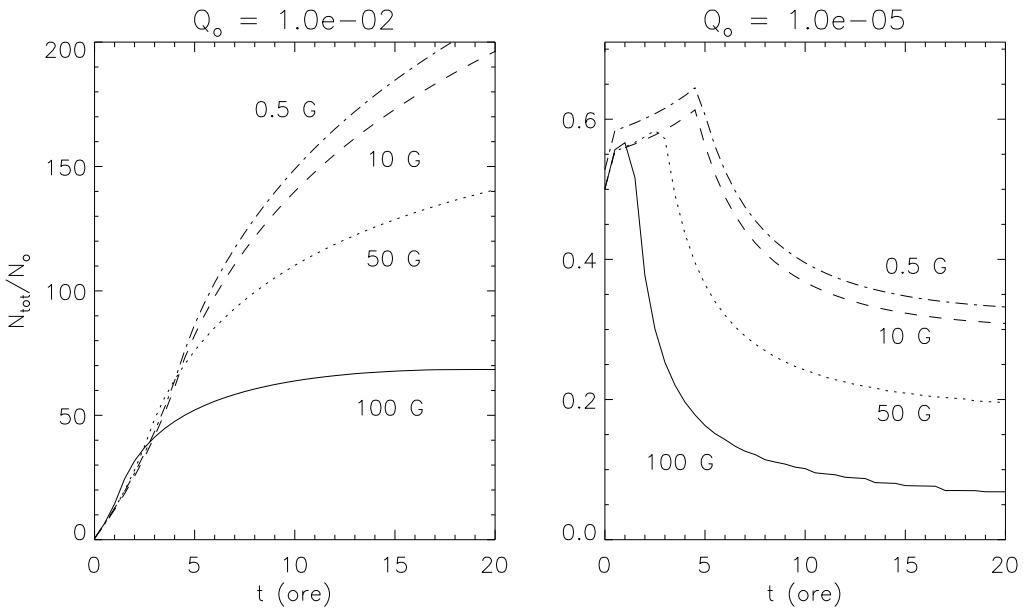

Fig. 3.3 Time evolution of the total density of relativistic electrons in the two cases $Q_\circ = 10^{-2}$ sec^{-1} (left) and $Q_\circ = 10^{-5}$ sec^{-1} (right), for different values of the magnetic field. The others parameters are the same of Fig. 3.2.

obtain:

$$I = \frac{Q_\circ K_\circ}{\delta - 1} \begin{cases} (\gamma_{\circ 1} - 1)^{1-\delta} - (\gamma_\circ - 1)^{1-\delta} & \gamma \leq \gamma_{\circ 1} \\ (\gamma - 1)^{1-\delta} - (\gamma_\circ - 1)^{1-\delta} & \gamma > \gamma_{\circ 1} \, . \end{cases} \tag{3.8}$$

Fig. 3.2 shows the time evolution of the energy distribution in the case $\delta = 2$, $\gamma_{\circ 1} = 1.1$, at two different positions in the loop corresponding to $B = 100$ G and $B = 10$ G, assuming $B(r, 90°) = 0.1$ G and $n_e = 10^7$ cm^{-3}. The distribution has been computed for two different values of $Q_\circ$. As it can be seen, for $Q_\circ = 10^{-2}$ sec^{-1} the injection term dominates over energy losses and the number of particles increases with time, tending to a steady state; energy losses however modify the shape of the distribution, flattening it at low energies and increasing its slope at high energies. If on the other hand $Q_\circ$ is very low (10^{-5} sec^{-1}), in regions of low magnetic field the distribution remains nearly steady, while for higher fields the rapid decrease of the number of high-energy electrons, due to the higher efficiency of synchrotron losses, is balanced only in part by the new accelerated particles, causing the formation of a knee in

the distribution. It is to be noted that in the case $Q_\circ = 10^{-2}$ the energy distribution does not depend much on magnetic field, and in particular it can be considered in good approximation a power-law in all points of the loop; this is consistent with our hypothesis of the previous chapter, where we had assumed that the distribution at the end of the injection was a homogeneous power-law. In the case $Q_\circ = 10^{-5}$, on the contrary, this is no longer true in regions of high magnetic fields.

Fig. 3.3 shows the time evolution of the total density of relativistic electrons, $N_{\rm R}(t) = \int N(\gamma, t)\, d\gamma$, for different values of the magnetic field B, for the two considered values of $Q_\circ$. If $Q_\circ$ is large, the number of electrons increases until it reaches a constant value at increasingly larger times as B decreases; if $Q_\circ$ is small, there is an increase only during the initial phases of the flare, then losses begin to dominate and the number of electrons decreases.

§ 3.4 Evolution of the spectrum and of the brightness distribution

As mentioned in Chapt. 2, the time evolution of the spectrum is obtained by substituting the energy distribution at time t, given by Eq. (3.7), in the approximate expressions for the emissivity and absorption coefficient derived by Klein (1987; Eq. (2.8)), and then computing the flux density. As in the previous case we considered the presence of the thermal coronal plasma by including in the calculation of the emission both the free-free contribution and the Razin effect.

For the source structure we have adopted the same model of the previous chapter, considering a magnetic loop lying on the plane of the sky and connecting two starspots on the stellar surface, and assuming that the field is constant along lines parallel to the line of sight.

For the geometrical and physical parameters of the loop we have used the values adopted in the previous chapter, and we have computed the evolution of the spectrum in the two cases $Q_\circ = 10^{-2}$ sec^{-1} and $Q_\circ = 10^{-4}$ sec^{-1}, assuming an initial density of electrons at the loop top equal to $N_\circ = 5 \times 10^3$ cm^{-3}. We abandoned the value $Q_\circ = 10^{-5}$ sec^{-1} considered in the previous section since

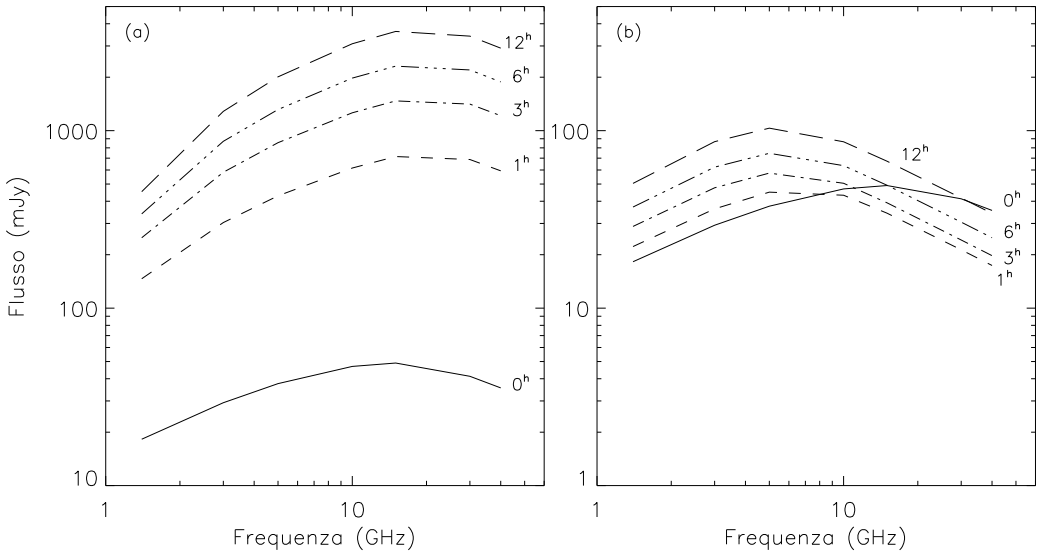

Fig. 3.4 Time evolution of the spectrum in a loop with $\Theta = 90°$, $R_{\rm spot} = 20°$, $B_{\rm max} = 1000$ G, for $\delta = 2$, $n_{\rm e} = 10^7$ cm^{-3}, $N_\circ = 5 \times 10^3$ cm^{-3}, in the two cases $Q_\circ = 10^{-2}$ sec^{-1} (a) and $Q_\circ = 10^{-4}$ sec^{-1} (b).

it is too low to be able to contrast losses and therefore to allow an increase of the flux density, and moreover, as already noted, since it is in contrast with the assumptions made in Chapt. 2.

The results are shown in Fig. 3.4. It can be seen that the strongest variations of the flux density or of the spectral shape take place shortly after the beginning of the acceleration; similar results, although assuming $t = 0$ at the end of the particle injection, were found in Chapt. 2. In the case of Fig. 3.4a, where the number of accelerated particles is quite high, the flux density increases due to the increase of the total number of electrons, while the shape remains unchanged, since in this case losses are negligible. If $Q_\circ$ is lower, as in Fig. 3.4b, the higher efficiency of energy losses in regions of high magnetic field close to the stellar surface rapidly reduces the emission from these regions modifying the shape of the spectrum, which becomes optically thin at higher frequencies; the increase of the flux density on longer timescales is due to the contribution to the emitted radiation from regions of lower magnetic field, where energy losses are negligible.

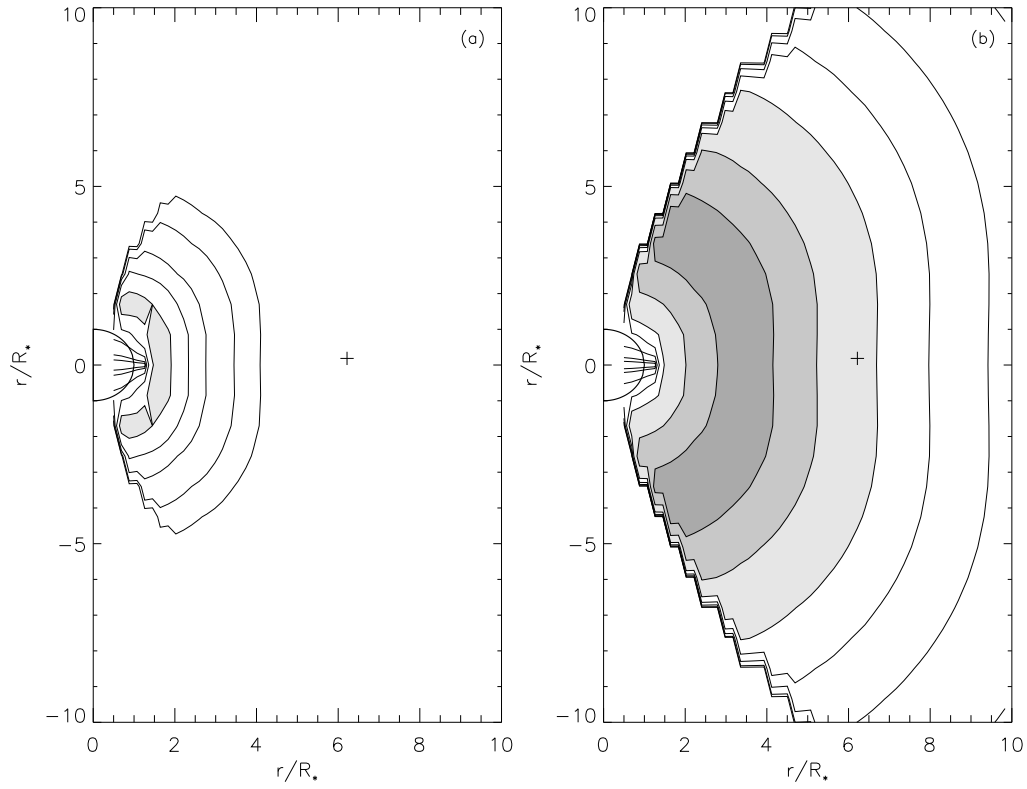

Fig. 3.5 Brightness distribution on the plane of the sky at $t = 0$ (a) and $t = 4^{\rm h}$ (b) in the case shown in Fig. 3.4a. Contour levels correspond to an intensity $I = 10^{-9}$, 2×10^{-9}, 5×10^{-9}, 10^{-8}, 2×10^{-8}, 5×10^{-8} e 10^{-7} erg cm^{-2} sec^{-1} Hz^{-1} sr^{-1}. Contours corresponding to intensities greater than 2×10^{-8} erg cm^{-2} sec^{-1} Hz^{-1} sr^{-1} have been shadowed for the sake of clarity. The cross marks the position of the companion star when the system is in quadrature.

We have also computed the brightness distribution on the plane of the sky in the two cases of interest (Fig. 3.5 e 3.6), for $t = 0$ and $t = 4$ hours. In both figures we have shadowed the contours corresponding to intensities higher than 2×10^{-8} erg cm^{-2} sec^{-1} Hz^{-1} sr^{-1}. As it can be seen, the injection of energetic particles into the loop, which increases the density of emitting electrons expecially in the outer regions where the magnetic field is lower, causes an increase of the intensity of the emitted radiation: this results in an apparent increase of the size of the radio source which assumes a *core-halo* structure in agreement with VLBI observations (Mutel et al. 1985; Lestrade et al. 1988). The effect is higher for higher values of the injection rate $Q_\circ$.

This result agrees very well also with VLBI observations of a flare occurred

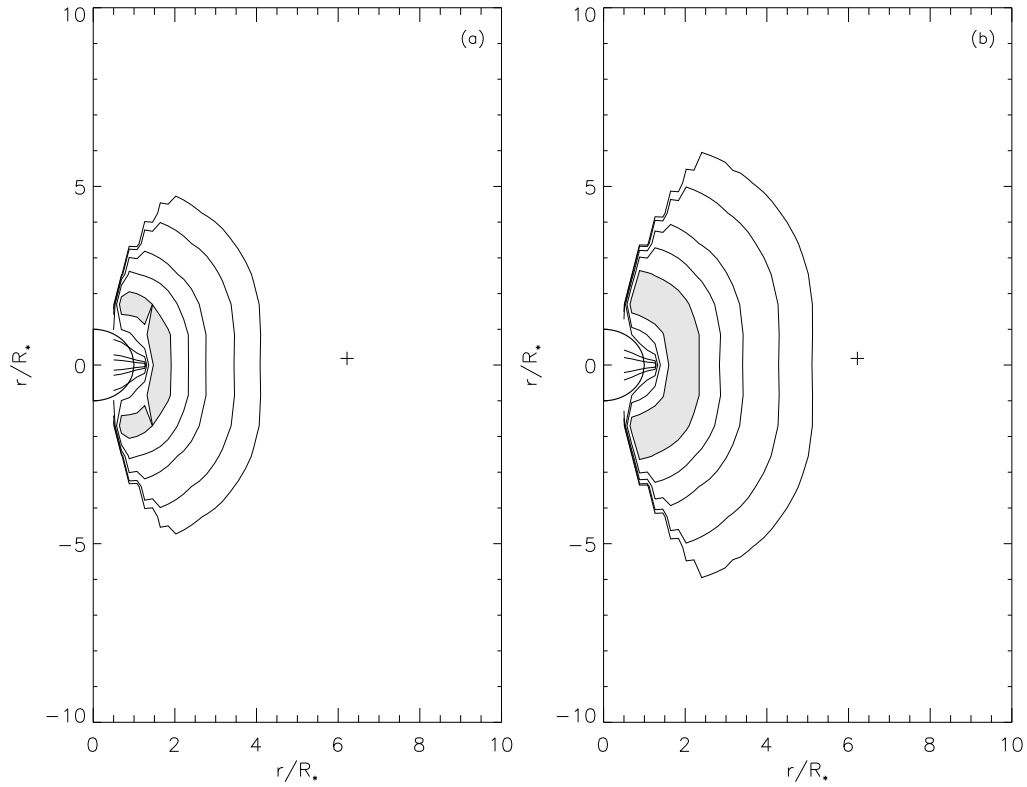

Fig. 3.6 Same as Fig. 3.5 in the case of Fig. 3.4b. Contour levels are the same as in Fig. 3.5.

on HR 1099 on April 29, 1992 (Trigilio et al. 1995), for which it was possible to follow the evolution of the emission in both the rising and decay phases. During the rising phase the flux density and the source size at 5 GHz increased by a factor of 3 and 2, respectively, in three hours: these values are very similar to those obtained with our model in the case $Q_\circ = 10^{-4}$ sec^{-1}. The different values of the flux density and the initial source size obtained from the model with respect to the observed ones can be abscribed to a different value of the initial density $N_\circ$ or to a longer time interval elapsed from the flare onset.

§ 3.5 Comparison with the UX Ari observations

We have used the model described in the previous sections to reproduce the spectra of UX Ari observed at Effelsberg (Fig. 3.1). To this aim, we need to take into account the influence of the different model parameters on the shape

and on the time evolution of the spectrum.

Regarding the spectral index δ of the initial energy distribution and of the distribution of injected electrons, it determines the slope of the optically thin part of the spectrum, but it does not significantly affect the optically thick part, hence its choice is not crucial in our case; its value was therefore fixed to $\delta \sim 1.7 - 2$. The slope of the optically thick part depends instead on the choice of the spot radius $R_{\rm spot}$ and separation Θ, which determine the loop size and therefore the relative extension of the halo and the core. From optical observations values of $R_{\rm spot} = 20^\circ - 30^\circ$ are deduced, while Θ is much more variable (see e.g. Vogt & Hatzes 1991; Elias et al. 1995). For a given $R_{\rm spot}$, a variation of Θ changes the slope of the optically thick part of the spectrum: for example, if Θ decreases the spectrum steepens, since this reduces the contibution from regions of low magnetic field far from the star, that emit predominantly at lower frequencies. The choice of Θ is however limited by the choice of $R_{\rm spot}$ to a range of values that give reasonable loop sizes.

An important parameter is the time $t_\circ$ when the particle acceleration, and hence the flare, starts, since it determines the shape of the energy distribution at the time of the observation. Unfortunately, given the sparse temporal coverage, it is not possible to infer $t_\circ$ from our data: in fact, the flare onset could have occurred at any time between the observation of the first rising spectrum and a preceding observation of quiescent emission. The emission level at $t = t_\circ$, before the flare onset, is determined by $N_\circ$, while the intensity at any later time depends on the choice of $Q_\circ$, $n_{\rm e}$ and $B_{\rm max}$.

The thermal plasma density, $n_{\rm e}$, from the considerations of the previous chapter, must have a value $n_{\rm e} \lesssim 10^7$ cm^{-3}. In this case the calculations have shown that the best agreement with the observed spectra is obtained assuming smaller values of $n_{\rm e}$; we have therefore assumed $n_{\rm e} = 10^6$ cm^{-3} for all four flares.

The value of the magnetic field $B_{\rm max}$ at the base of the loop determines the efficiency of synchrotron energy losses. As shown in Chapt. 2, these losses determine a cutoff in the spectrum which moves towards lower frequencies with increasing $B_{\rm max}$, due to the suppression of the emission from higher energy

Tab. 3.1 Parameters used to reproduce the spectra of the four observed flares

	δ	Θ (°)	$R_{\rm spot}$ (°)	$B_{\rm max}$ (G)	$N_\circ$ (cm^{-3})	$Q_\circ$ (sec^{-1})
Flare 1	2.0	75	20	300	2.35×10^5	1.5×10^{-5}
Flare 2	1.7	90	20	1000	4.0×10^2	2.2×10^{-3}
Flare 3	2.0	50	20	500	1.0×10^6	5.0×10^{-5}
Flare 4	2.0	90	20	1000	4.4×10^3	1.65×10^{-4}

electrons. The choice of $B_{\rm max}$ is linked to the choice of the time interval $t - t_\circ$ from the flare onset and depends on the position of the spectral peak.

In order to fit the observed spectra, we have first reproduced a ground level emission assuming a specific value for $t_\circ$ and deriving in this way $N_\circ$; the subsequent evolution of the spectrum is then determined by choosing $B_{\rm max}$, Θ and $Q_\circ$ in order to reproduce the observed spectral characteristics (position of the peak, spectral index and flux density increase with time). The results are shown in Fig. 3.7 and the adopted values of the parameters are given in Tab. 3.1. The values of Θ reported in Tab. 3.1 imply very extended loops, over dimensions comparable to the binary system separation. The magnetic field at the base of the loop derived from the comparison with observations is of the same order of magnitude or slighly lower than the photospheric values derived from optical observations (Giampapa et al. 1983; Gondoin et al. 1985; Donati et al. 1990). The lowest values are found for flares 1 and 3, for which, as explained later, we are observing a later phase of the flare, and are consistent with the fact that we do not see anymore the emission originating close to the photosphere, which is completely decayed, but only that coming from higher coronal regions.

The times shown in Fig. 3.7 are those actually used in the calculation, that have been derived from the real time intervals between the observations, and not from the approximated orbital phases shown in the figure. For flares 2 and 4 (Figs. 3.7b and 3.7d, respectively) the level of emission at $t = t_\circ$ is that corresponding to the quiescent phase of the star. However, the identification of this level with the quiescent one, although it seems the most obvious and

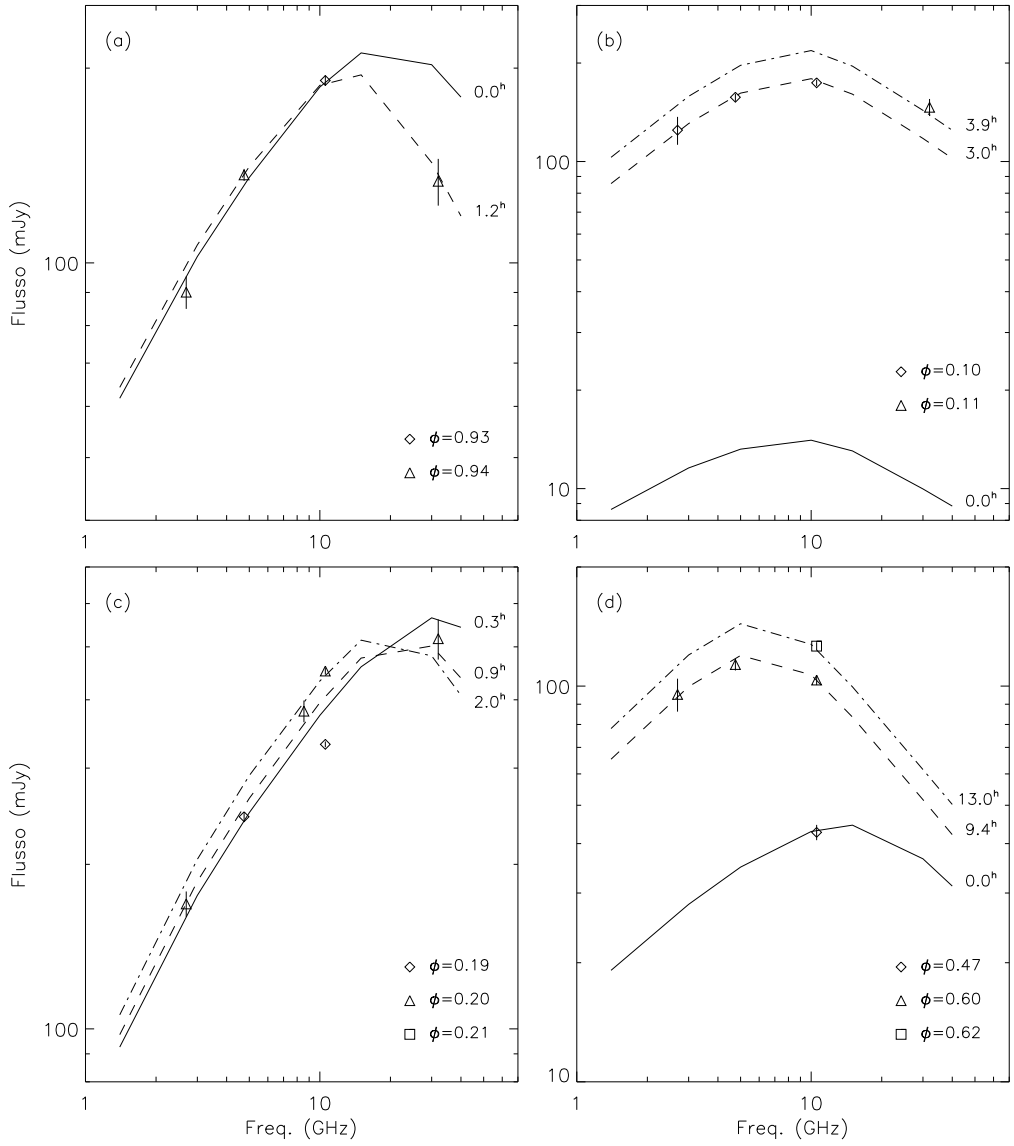

Fig. 3.7 Comparison between observed and computed spectra for the four flares of interest. (a) Flare 1; (b) flare 2; (c) flare 3; (d) flare 4.

elegant choice, is not always the best. In fact, the evolution of the energy distribution has been derived in the assumption of a constant particle injection rate and therefore the model must be applied in this limit. For example in flare 1 the emission keeps high but almost at the same level for a time $\Delta t \sim 1$ hour, implying that the flare is near its maximum, i.e. we are observing a phase where the acceleration is almost over. To reproduce such a case the only possibility is to assume a very low value of $Q_\circ$ in this time interval; however, the same

$Q_\circ$ cannot reproduce the whole rising phase starting from a quiescent level of about 10 mJy. For this reason we have assumed phase $\phi = 0.93$ as starting time and the corresponding emission as ground level. The same happens for flare 3 where we suppose that phase $\phi = 0.19$ corresponds to $t - t_\circ = 0.3$ hours. Flares 2 and 4, for which the evolution can be followed from the beginning, clearly show a longer time evolution. In particular, it becomes clear that flare 4 is the only one having a negative spectral index between 5 and 10 GHz because many hours have passed since the start of the acceleration.

The good agreement of the model results with the observed spectra confirms the interpretation of the flaring emission in terms of gyrosyncrothron emission from relativistic electrons continuously injected in a magnetic loop. How long this continuous supply of accelerated electrons can last is not known. For flare 3, for example, the data show that the emission increases for 23 hours; however our model, in which the amount of accelerated particles is constant in time, can reproduce only part of this evolution, namely 2 hours. This fact suggests that in reality the injection rate is variable and that the observed 23 hours increase is probably due to a succession of unresolved strong bursts. For the two flares 2 and 4, for which it is possible to follow the evolution starting from the quiescent emission ground level, we derive 4 and 13 hours respectively of constant injection. In any case, we can conclude that the observed flare rising phases imply a continuous supply of relativistic electrons at least for some hours. The observations are however too sparse in time to allow a definite better comprehension of the process.

As Fig. 3.7 shows, this model is able to reproduce flares having different spectral shapes and observed at different phases of their evolution, thanks to the interplay of radiative losses and continuous injection of fresh relativistic electrons. Flares observed near the peak (flares 1 and 3) have a very low injection rate, while those observed in their full rising phase need higher values of $Q_\circ$. We have also seen in the previous section that the predictions of the model on the increase of the flux density and the source size are in very good agreement with VLBI observations. Despite the good results, it is evident from the above considerations that a deeper insight in the injection mechanism and

hence in the physics of the flare will be possible only by taking into account also temporal variations of the injection rate. However a more detailed model can give useful information only if more complete data sets become available, with a better time coverage of the evolution of the flare spectrum from its onset to the end of its decay.

CHAPTER 4

ROTATIONAL MODULATION OF THE RADIO EMISSION

§ 4.1 Introduction

Observations of RS CVn and Algol-type bynaries show that the source of radio emission is associated with the active component of the system; since the active star is rapidly rotating with a period nearly equal to the orbital one (see Chapt. 1), this suggests the possibility that the observed radiation could vary with time as a function of orbital phase. Some authors investigated this possibility in the past (e.g. Gibson et al. 1978; Mutel & Morris 1988), but the scarce available data, and in particular the lack of observations extended over a sufficiently long period of time, led to the conclusion that this relationship did not exist. Recently, however, new observations of some RS CVn and Algol systems have been performed over several consecutive orbital periods, showing that during high-activity phases the radio flux density varies with time with a period comparable to the orbital one. This modulation is evident only at high flux levels, while it is not observed during quiescent phases, and can be interpreted assuming that the emission comes from a compact source, located near the stellar surface, which is occulted as the star rotates. The fact that the quiescent component arises from the entire binary system, as shown by VLBI observations, can explain the absence of modulation at lower flux levels.

In order to interpret these observations, in this chapter we will develop a simple model in which the radio emission arises from a dipolar loop which

is located at the stellar equator and is seen under different angles as the star rotates. We will first consider the case of emission from a population of electrons which is constant in time; we will then assume, instead, that a flare occurs in the loop and then the emission decays due to energy losses, according to the model described in Chapt. 2. As it will be seen, this model reproduces successfully the observed light curves.

§ 4.2 Observations of rotational modulation of the radio emission

The first indication of a possible relationship between the radio flux density and the orbital phase was obtained from the observations of UX Ari performed during the monitoring program at the Effelsberg radiotelescope (Neidhöfer et al. 1993; Torricelli Ciamponi et al. 1995; Massi et al. 1996). As mentioned in Chapt. 2, the system is observed during the gaps between other scheduled observations, at various frequencies between 1.4 and 43 GHz depending on the available receiver; in spite of the poor temporal coverage and the variety of the observing frequencies, if we plot the observed flux density as a function of the orbital phase ϕ (Fig. 4.1) we see that the most intense flares (with $F_\nu \gtrsim 200$ mJy) are more common around $\phi = 0$, when the active star is in front, while they are never observed around $\phi \sim 0.4$, where a sharp minimum is found; on the other hand, the emission at flux levels lower than ~ 50 mJy does not show any significant modulation. This behaviour can be interpreted as a geometric occultation of the source during the rotation of the system. The fact that the modulation is present only at higher flux levels implies that the source of the most intense emission is a compact region near the stellar surface, while the quiescent component should arise from an extended region, too large to be obscured, in agreement with the core-halo structure observed with VLBI techniques (Mutel et al. 1985; Lestrade et al. 1988).

These results are confirmed by other observations of UX Ari by Elias et al. (1995): these authors observed the system at 5 GHz in October 1992, just before the start of the Effelsberg monitoring program, about three times per day during three consecutive orbital periods, simultaneously with observations

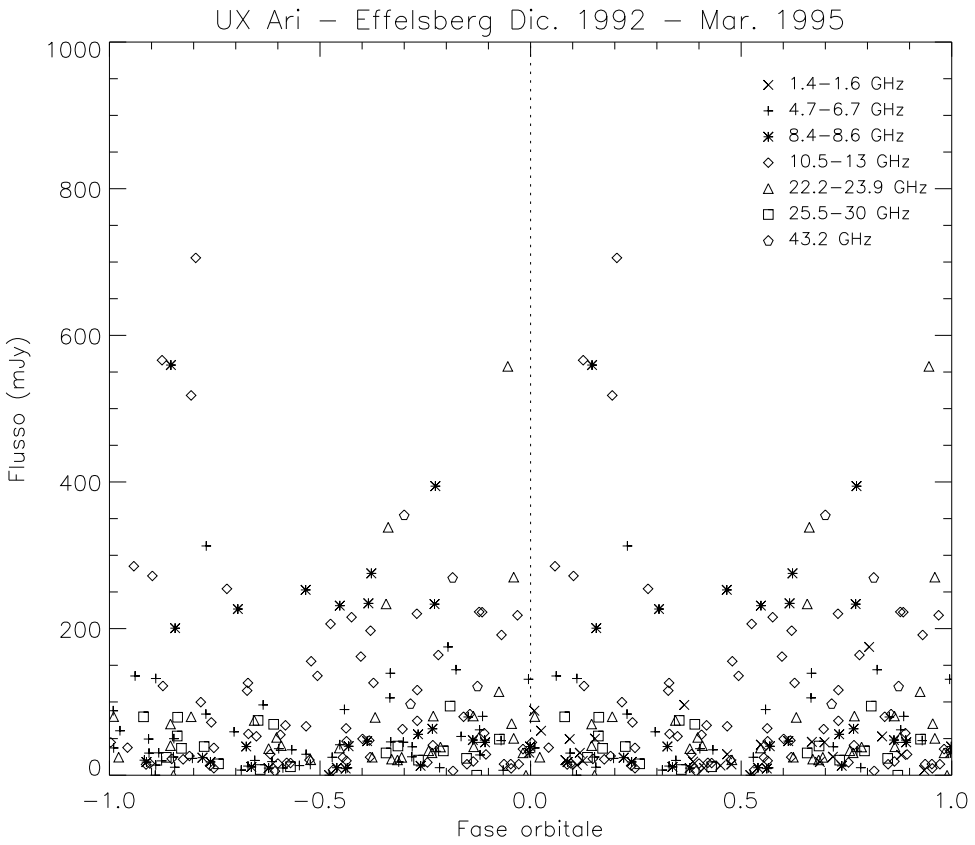

Fig. 4.1 Observations of UX Ari performed at the Effelsberg radiotelescope from December 1992 to March 1995, plotted as a function of orbital phase (Neidhöfer et al. 1993; Massi et al. 1996). Observations at different frequencies are indicated with different symbols.

of the light curve at optical wavelenghts. The temporal behaviour of the radio emission, shown in Fig. 4.2, indicates that UX Ari was at the beginning of a new active period, and shows a series of peaks of different intensity, with the highest ones corresponding to $\phi \sim 0$, while there is a minimum around $\phi = 0.7$. Comparing the radio and optical data, these authors found that the optical and radio light curves, plotted as a function of orbital phase, are perfectly anticorrelated, with the maximum total radio flux corresponding to the minimum of the optical emission. This result clearly indicates that the emission arises in coronal active regions located above the starspot groups. A similar association between maximum radio emission and spots has been observed also on the single star AB Dor by Lim et al. (1992, 1994).

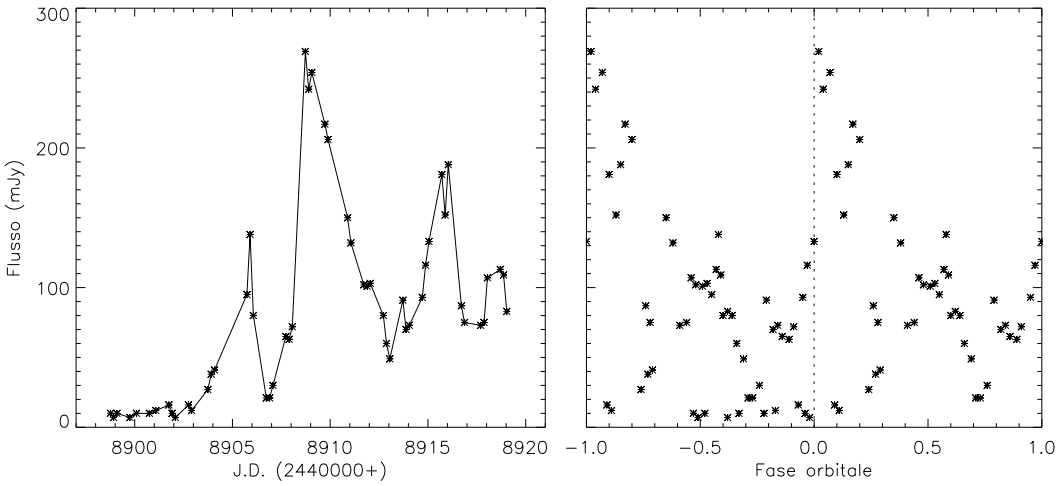

Fig. 4.2 Observations of UX Ari performed in October 1992 at 5 GHz by Elias et al. (1995). In (a) we show the flux density as a function of time; in (b) the observations are plotted as a function of the orbital phase.

Rotational modulation of the emission has been observed also at lower flux levels ($10 - 80$ mJy) on Algol by Lefèvre et al. (1994): observing the system for three consecutive orbital periods outside of eclipses, these authors found a systematic decrease of the radio flux density between phases $0.2 - 0.35$, and an increase for $\phi = 0.6 - 0.75$. A similar, although less evident behaviour was found also for the system σ^2 CrB.

During high-activity periods, when the source is subject to frequent and strong flares, the radio light curve shows a more complex behaviour. Trigilio et al. (1996) observed UX Ari with the Noto radiotelescope from January 7 to February 6, 1993, covering almost five consecutive orbital periods. Their observations, plotted in Fig. 4.3 as a function of orbital phase, show a background emission of the order of $100 - 200$ mJy, which appears to be modulated with the orbital period, with a maximum at $\phi = 0$ and a minimum at $\phi \sim 0.5$; superimposed on this emission there is a series of strong flares with characteristic timescales of a few hours, occurring at all orbital phases with similar temporal behaviour. It is probable that in this case two sources contribute to the observed emission: one, associated with active regions at low latitudes, which

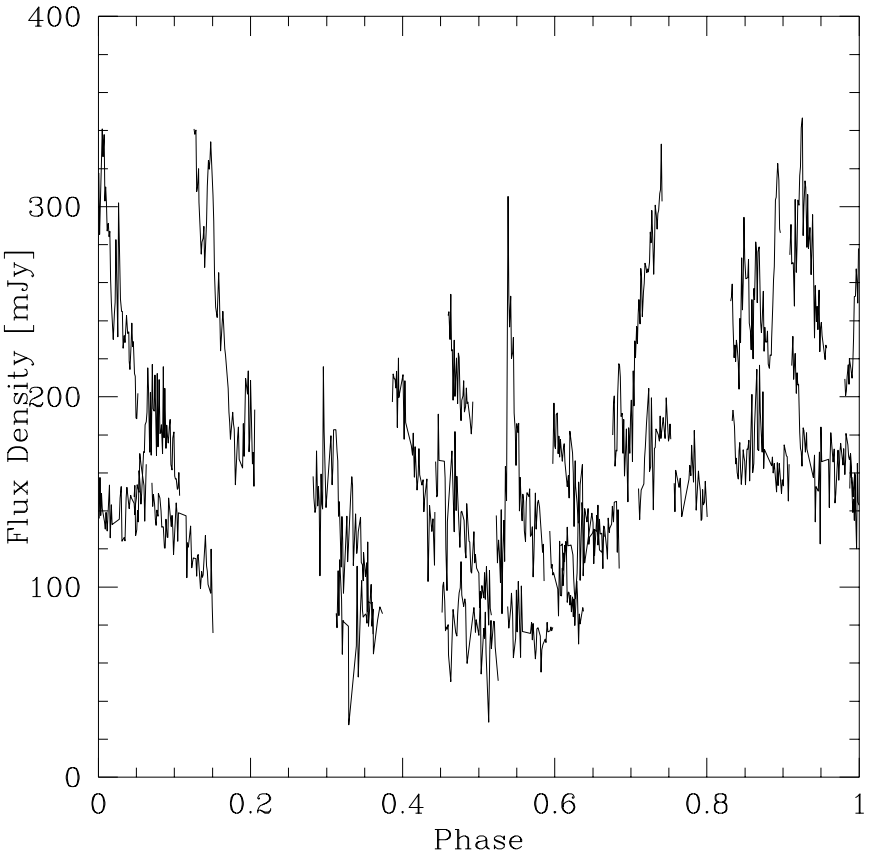

Fig. 4.3 Observations of UX Ari at 5 GHz performed at the Noto radiotelescope in January-February 1993 (Trigilio et al. 1996), plotted as a function of orbital phase.

is partially occulted during the stellar rotation giving rise to the modulated component, and the other, where flares occur, which is always visible, possibly associated with the polar spot derived from optical observations (e.g. Vogt & Hatzes 1991).

In the light of these new results, we have examined old radio observations of active stars, in particular the series of outburts observed on the system HR 1099 in February 1978 (Feldman et al. 1978), that lasted for nine days, corresponding to three orbital periods. In their paper, the authors noticed a periodicity of about one burst per day, but, since the orbital period is nearly three days, they concluded that there was no significant correlation between the radio peaks and the orbital phase. However, when we plotted their data as a function of phase

(Fig. 4.4), we realized that all peaks fall around three well defined orbital phases (0, 0.3 and $0.6 - 0.7$), therefore suggesting that the emission could have been originated in three active regions simultaneously present on the star. The peaks are very narrow, and expecially those at $\phi \sim 0.3$ have very rapid rise and decay times: this is probably due to a region that is completely eclipsed during the stellar rotation and remains visible only for a short period of time. A peculiar characteristic of these bursts is that they slightly drift towards higher orbital phases in successive periods.

§ 4.3 Modulation of the emission from a steady particle distribution

In order to reproduce the observed rotational modulation, we have computed the gyrosynchrotron emission from a dipolar magnetic loop anchored on the surface of the active star and rotating with it. For the sake of simplicity, we have assumed that the loop lies on the equatorial plane and that the star's rotation axis is perpendicular to the line of sight. This is a rather strong approximation, since it is strictly valid only for eclipsing systems such as Algol; the most active RS CVn systems on the contrary usually have a low inclination of the rotation axis with respect to the line of sight, and are therefore viewed nearly pole-on (except for UX Ari, which has $i = 60°$, the inclination is $i = 33°$ for HR 1099 and only 9° for HR 5110). However we will see that even with such an approximation the model allows us to obtain results in good agreement with the observations.

The structure of the source on the equatorial plane is the same as in the previous chapters, i.e. the source consists of a magnetic loop connecting two starpots on the stellar surface, which is generated by a dipole buried below the photosphere and lying on the equatorial plane. The magnetic field varies only on the equatorial plane and is constant along lines perpendicular to it. The only difference with the previous cases is that now we have assumed, for the sake of simplicity, that the height of the source perpendicularly to the equatorial plane is constant and given by $L \simeq R_\star$.

As a preliminary calculation, we consider the effect of rotation on the ra-

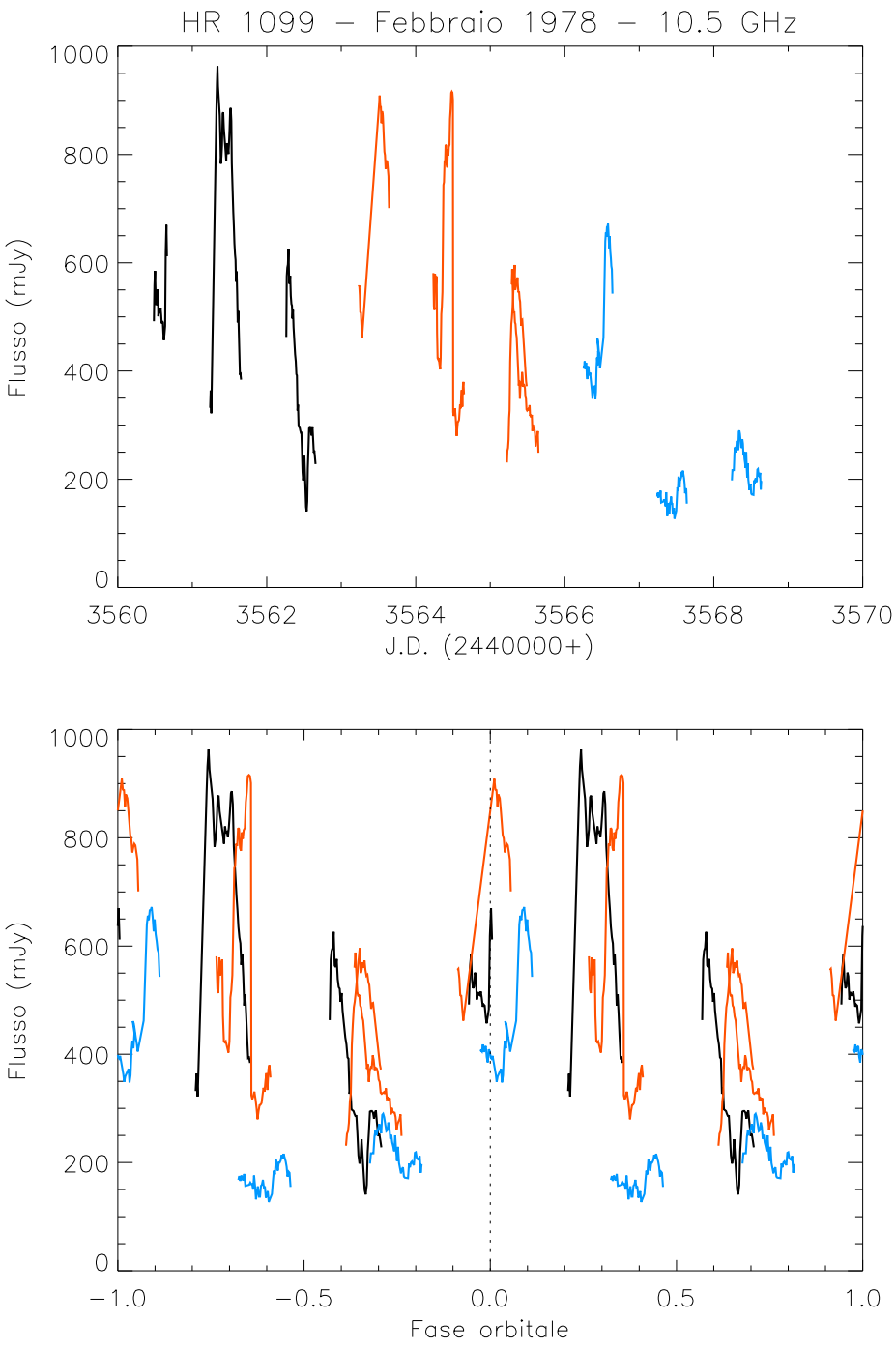

Fig. 4.4 Observations of HR 1099 during the series of outbursts in February 1978 (Feldman et al. 1978). (a) Radio light curve during the nine observing days; (b) flux density as a function of orbital phase. Data relative to different orbital periods are indicated with different colours for the sake of clarity.

diation from a non-thermal population of electrons which does not vary with time. We assume that the energy distribution is a power-law of the type described by Eq. (2.14), with minimum energy $\gamma_1 = 1.1$ and total density of relativistic electrons $N_\circ$; the value of the exponent δ has been fixed to $\delta = 2$. The gyrosynchrotron emission is computed using the approximate expressions by Klein (1987) for different values of the angle α between the line of sight and the loop axis; varying α between 0° and 360° we obtain the radio light curve during a complete stellar rotation. In this case the calculation of the intensity is complicated by the fact that the emissivity and the absorption coefficient are no longer constant along the line of sight, but vary due to the different values of the magnetic field and of the angle θ in different points of the loop. In the calculation we have also taken into account the influence of the thermal coronal plasma through free-free emission and absorption and the Razin effect.

Optical observations show the presence of large spots or spot groups with radii of the order of $15^\circ - 30^\circ$ and angular separation $60^\circ - 110^\circ$ (Dorren et al. 1981; Vogt & Penrod 1983; Gondoin 1986; Rodonò et al. 1986; Vogt & Hatzes 1991; Elias et al. 1995). If the source consists of a very extended loop connecting two large spots with large separation, as in the previous chapters, only a small fraction of it will be occulted by the star: in this case we obtain only a weak modulation of the emission due only to the variation of the angle between the magnetic field and the line of sight. The modulation effect becomes stronger if we instead consider a small loop, anchored on two spots inside a single starspot group, which is nearly completely occulted by the star when $\alpha \sim 180^\circ$, thus considerably reducing the observed emission. For this reason, in this chapter we will consider smaller loops, in order to better evidentiate the flux variations.

Fig. 4.5 shows the flux density as a function of phase $\phi = \alpha/2\pi$ for a loop with $R_{\rm spot} = 10^\circ$ and angular separation $\Theta = 40^\circ$, at the three frequencies 1.4, 5 and 10.5 GHz. As it can be seen, the modulation induced by the stellar rotation gives rise to a broad peak centered at $\phi = 0$, corresponding to $\alpha = 0$ (when the loop is in front), and a minimum at $\phi = 0.5$, whose depth is higher if a higher fraction of the loop is obscured by the star. The modulation is more evident at higher frequencies, in agreement with the fact that the emission at

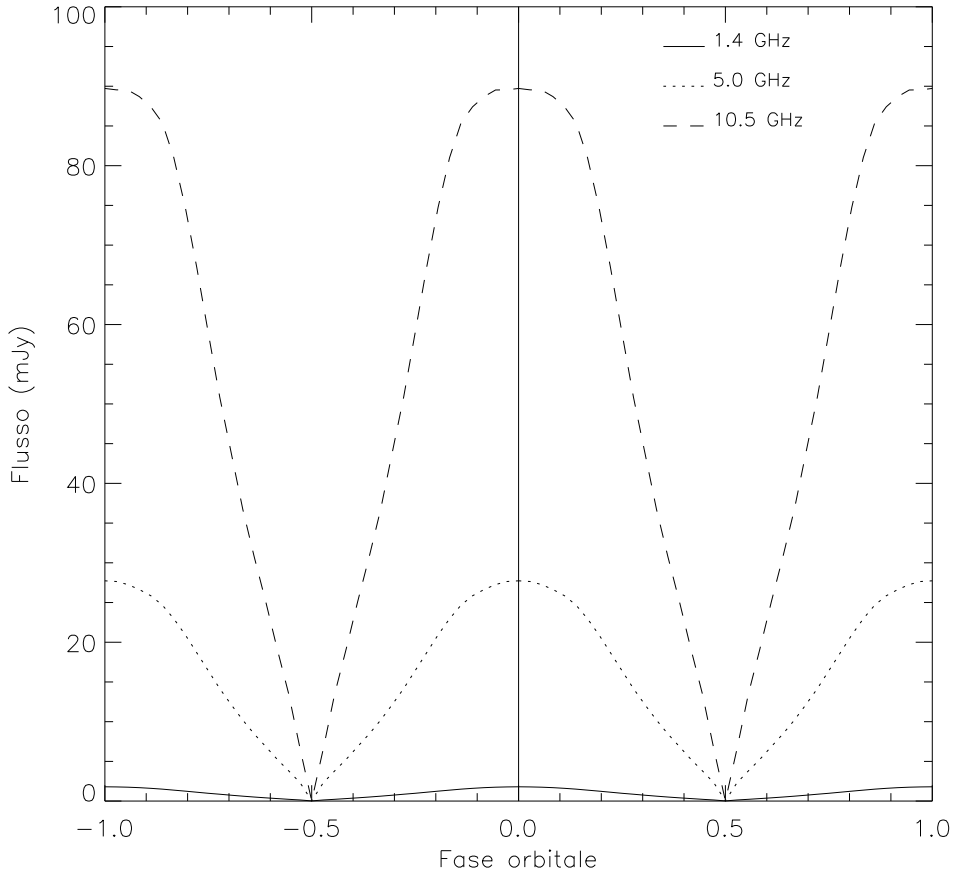

Fig. 4.5 Rotational modulation of the emission from a loop with a constant electron energy distribution. The three curves correspond to 1.4, 5 and 10.5 GHz. The calculations are referred to UX Ari ($R_\star = 2.1 \times 10^{11}$ cm, $d = 50$ pc). The adopted parameters are $R_{\rm spot} = 10°$, $\Theta = 40°$, $B_{\rm max} = 1000$ G, $N_{\rm o} = 10^6$ cm^{-3} and $n_{\rm e} = 10^7$ cm^{-3}. Orbital phase 0 corresponds to $\alpha = 0$.

high frequency is more concentrated in the lower regions of the loop, near the stellar surface, with respect to lower frequencies, as shown by Klein & Chiuderi Drago (1987).

The results obtained with this model are in good agreement with the flux variations observed at low flux levels by Leféyre et al. (1994), and with the background modulation observed on UX Ari by Trigilio et al. (1996), but the broad peak at $\phi = 0$ is not able to reproduce the steeper decreases observed in the light curves during higher activity periods. However, in the latter case

the presence of flares gives an additional contribution to the flux variations, and we can therefore obtain a more rapid decrease of the emission as a result of the decay phase of flares. In the next section we will therefore consider the variations of the emitted radiation due to the combined effect of the stellar rotation and of the time evolution of the energy distribution due to energy losses.

§ 4.4 Modulation of the emission during the decay phase of a flare

In order to take the contribution of flares to the flux variations into account, we assume that a flare occurs in the loop at $t = 0$ when the angle between the line of sight and the loop axis has a given value $\alpha = \alpha_\circ$. For the sake of simplicity, as in Chapt. 2 it is assumed that the particle injection in the source takes place istantaneously at the flare onset with an isotropic and homogeneous energy distribution described by Eq. (2.14); the distribution then evolves in time due to collision and syncrotron energy losses, and the emission decays according to the model described in Chapt. 2. Contrary to the previous chapters however, as already anticipated in Chapt. 2, we now abandon the unrealistic hypothesis of a loop which remains fixed on the plane of the sky, and we consider instead a loop rotating with the star: at each time $t > 0$ the angle between the line of sight and the loop axis can be obtained from the relation:

$$\alpha(t) = \alpha_\circ + \frac{2\pi}{P_{\rm orb}}\, t\,. \tag{4.1}$$

where we substituted the orbital period of the system, $P_{\rm orb}$, for the rotation period, $P_{\rm rot}$, since, as already said before, they are generally nearly equal.

The computed light curves at 1.4, 5 and 10.5 GHz are shown in Fig. 4.6 for three different values of $\alpha_\circ$ (0°, 90° and 180°). The adopted values of the parameters are the same of the previous section, and the calculations are referred to UX Ari, which has $P_{\rm orb} = 6.44^{\rm d}$. In Fig. 4.7 the light curves obtained in the two cases $\alpha_\circ = 0°$ and $\alpha_\circ = 90°$ (solid lines) are compared with those obtained considering only the rotational modulation of the emission from a constant particle distribution (dotted lines), and those obtained only from the

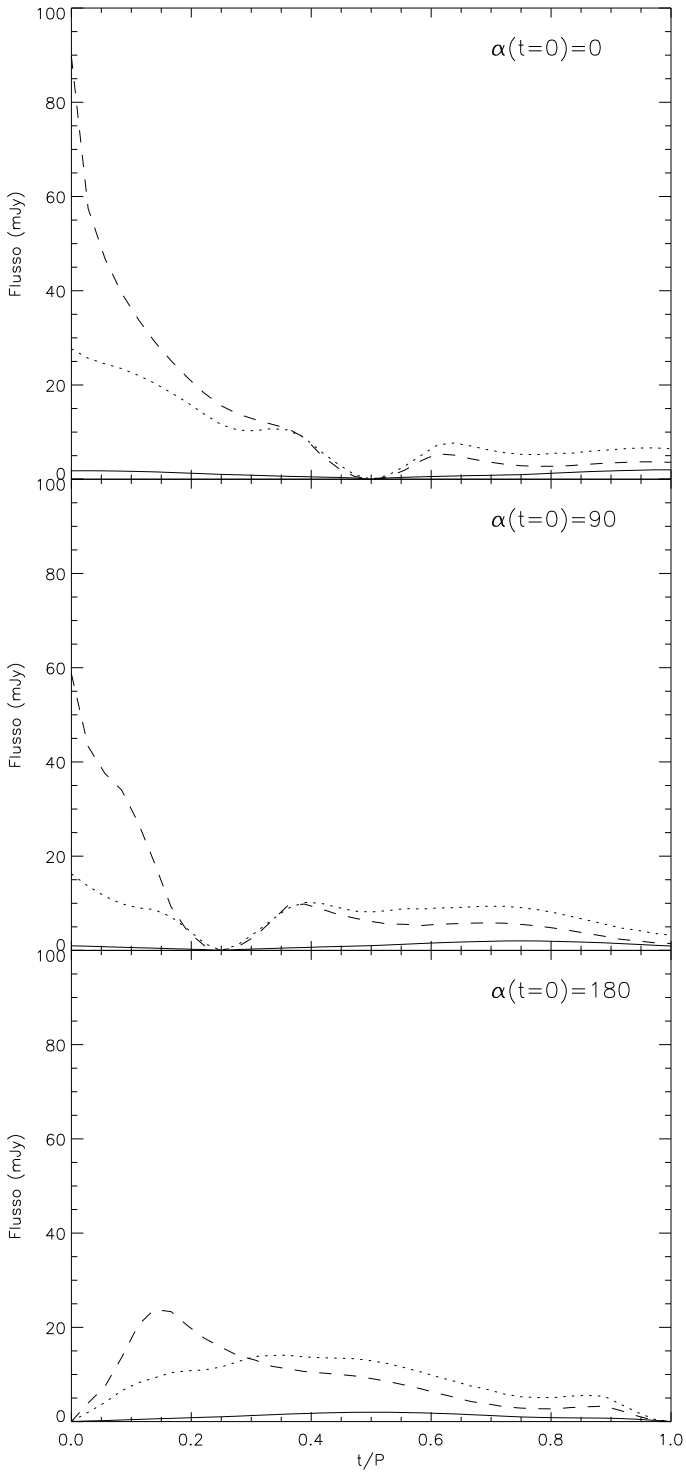

Fig. 4.6 Light curves obtained in the case of rotational modulation plus time evolution of the emission, for $\alpha_\circ = 0°$, 90° and 180°. The calculations are referred to UX Ari ($d = 50$ pc, $P_{\rm orb} = 6.44^{\rm d}$) and the parameters are the same as in Fig. 4.5. The curves correspond to 1.4 GHz (solid line), 5 GHz (dotted line) and 10.5 GHz (dashed line).

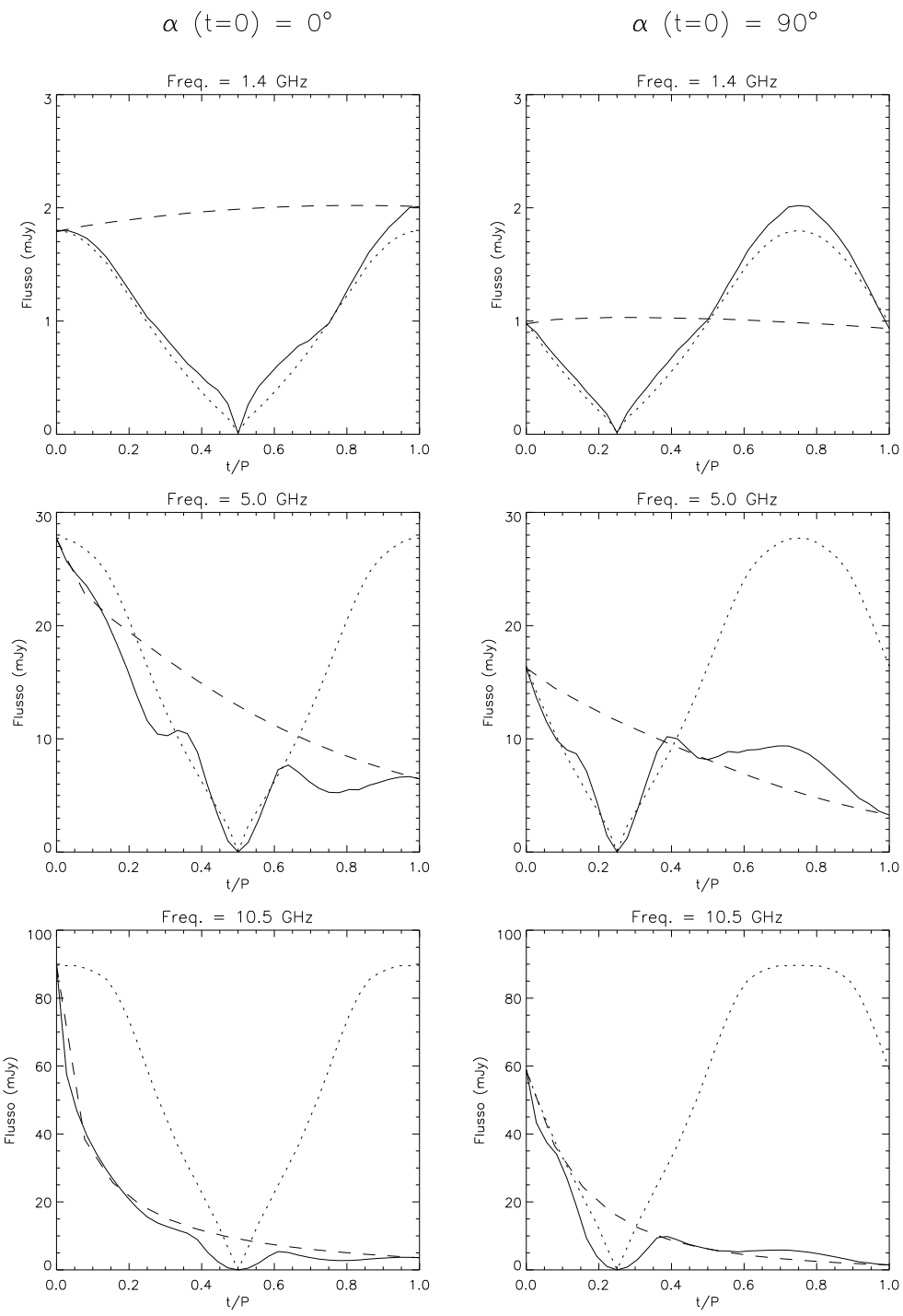

Fig. 4.7 Comparison between the light curves obtained in the case of rotational modulation only with a constant distribution (dotted line), of evolution of the distribution only in a fixed loop (dashed line), and of the combined effect of rotation and evolution (solid line). The calculations have been made at 1.4, 5 and 10.5 GHz in the two cases $\alpha_o = 0°$ and $\alpha_o = 90°$ with the same parameters as in Fig. 4.5.

time evolution of a distribution in a fixed loop with $\alpha(t) = \alpha_\circ$ (dashed lines). As it can be seen, the combined effect of stellar rotation and of time evolution of the flux density gives narrower peaks, expecially at higher frequencies; stronger magnetic fields or higher thermal densities, increasing the efficiency of energy losses, can further reduce the peak width. These results are in very good agreement with the observed light curves during active periods.

Fig. 4.8 shows the comparison between the temporal behaviour of the spectrum in the three cases under consideration: rotation only, evolution only and combination of rotation and evolution, for the case $\alpha_\circ = 0$. The effect of rotation only with a constant energy distribution is just a periodic variation of the flux density keeping the spectral shape unchanged, except for a small range of angles α around 180° where the spectrum can change sensibly because the source is more eclipsed at higher frequencies, where the emission is more concentrated near the stellar surface. For symmetry reasons, the spectrum is identical in the positions corresponding to angles α and $360° - \alpha$. In the case of time evolution only, as shown in Chapt. 2, the spectrum flattens becoming optically thin at high frequencies, while the flux remains nearly constant at low frequencies. Combining the two effects we obtain a very complex behaviour, as shown in the bottom panel of Fig. 4.8, with variations of both the flux density and the spectral shape.

§ 4.5 Comparison with observations

The comparison of the spectra obtained from the model with the observed ones could give important informations on the physical parameters of the emitting regions. To this aim, we need multifrequency observations performed several times during one or more consecutive orbital periods, that are unfortunatly not yet available. We can therefore only compare the theoretical light curves at a single frequency with the observed ones. We will consider in particular the observations of UX Ari by Elias et al. (1995) and of HR 1099 by Feldman et al. (1978).

As mentioned in Sect. 4.2, Elias et al. (1995) observed UX Ari at 5

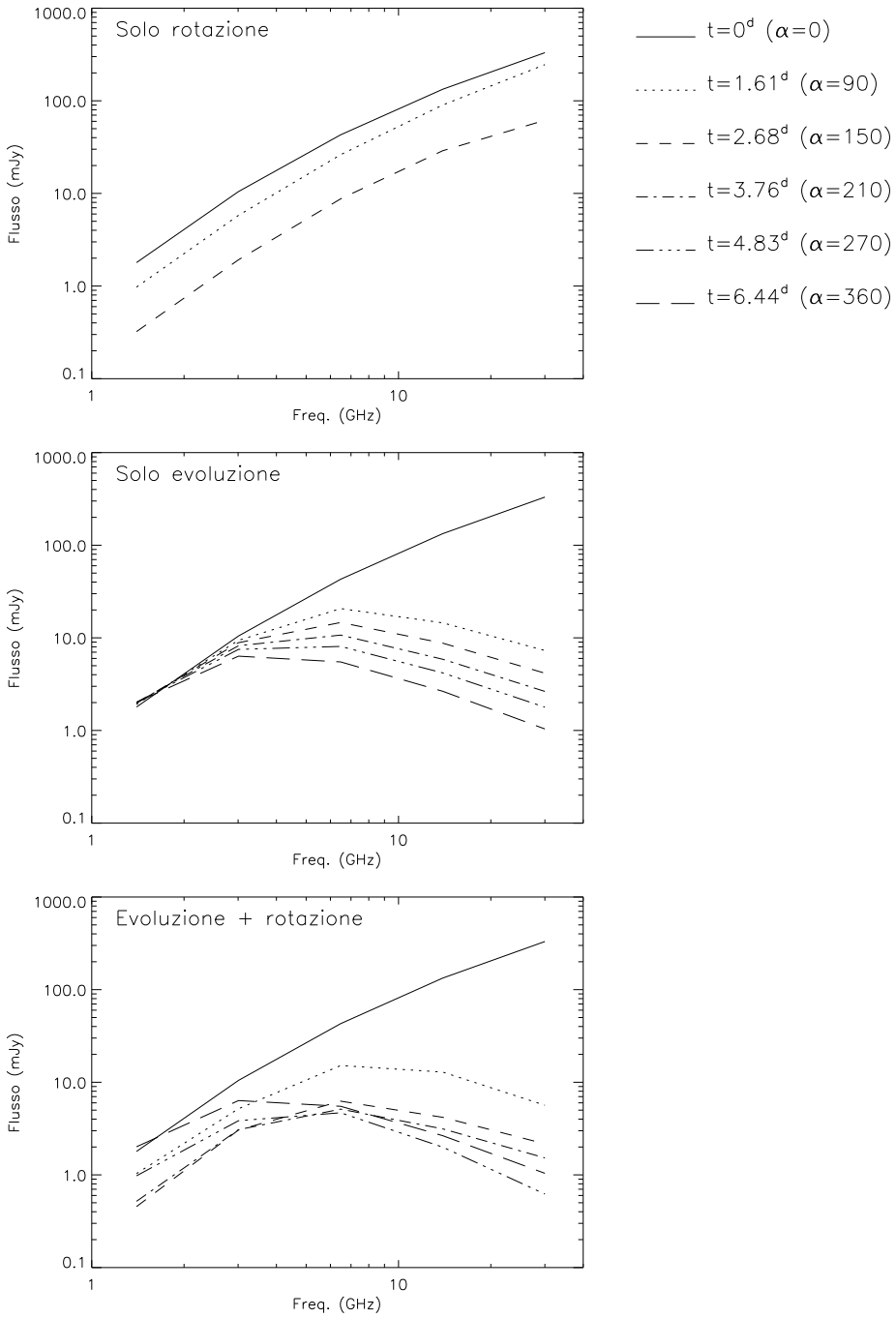

Fig. 4.8 Comparison between the predicted variations of the spectrum in the case of rotational modulation only (top), time evolution only in a fixed loop (middle) and when both effects are present (bottom). In the first case, the spectra obtained at angles $\alpha > 180°$ are coincident with those at angles $360° - \alpha$. The parameters are the same as in Fig. 4.5.

GHz during three consecutive orbital periods in October 1992, obtaining the light curve shown in Fig. 4.2 and finding that it is perfectly anticorrelated with the optical light curve. The radio emission therefore originates in coronal active regions located above the photospheric spots. The optical light curve was reproduced by these authors assuming the presence of two large spots or more probably starspot groups, with radius $\sim 20° - 30°$, both located at latitude 30° and separated in longitude by $\sim 110°$; the effective angular separation between the two groups, taken on the arc of parallel connecting them, is therefore $\sim 90°$. One of the spots faces the observer for $\phi \sim 0$.

We have assumed that the optical light curve is due to the presence of two bipolar spot groups and that the radio emission comes from two loops, anchored on each of the starspot groups. The choice of two small loops instead of a single extended loop connecting the two groups is necessary in order to have a significant modulation of the radio emission; on the other hand we cannot assume too small loops, otherwise it is not possible to reproduce the high values of the observed flux density (up to ~ 300 mJy) with reasonable values of the parameters. We have therefore considered two equal loops, each connected to two spots of radius $R_{\rm spot} = 15°$ and angular separation $\Theta = 40°$. In each loop a flare occurs at a given time $t_\circ$ and for a given position $\alpha_\circ$ (different for the two loops); before the flare there is no emission and we assume an istantaneous rising phase as in the previous section. We indicate with $t_\circ = 0$ the time of the first flare; at successive times, the total flux density is the sum of the contributions from the two loops.

The parameters used to reproduce the light curve of UX Ari are shown in Tab. 4.1. As it can be seen, we have considered for both loops a magnetic field $B_{\rm max} = 1000$ G in the feet of the loop. In the first loop the flare occurs for $t_\circ = 0$ at orbital phase $\phi = 0.5$, when $\alpha_\circ = 100°$, with an initial density of relativistic electrons $N_\circ = 5 \times 10^7$ cm^{-3}; in the second loop the flare occurs for $\phi = 0.97$ and $t_\circ = 3.04^{\rm d}$, when $\alpha_\circ = 0°$, with $N_\circ = 10^7$ cm^{-3}. The thermal plasma density is $n_{\rm e} = 10^7$ cm^{-3} in the first loop and $n_{\rm e} = 10^8$ cm^{-3} in the second one.

In Fig. 4.9 we show the geometry of the source with respect to the observer

Tab. 4.1 Parameters used to reproduce the observations of UX Ari by Elias et al. (1985). The orbital period of UX Ari is $P_{\rm orb} = 6.44^{\rm d}$.

Loop	Θ	$R_{\rm spot}$	$B_{\rm max}$ (G)	$n_{\rm e}$ (cm^{-3})	$\alpha(t=0)$
1	40°	15°	1000	10^7	100°
2	40°	15°	1000	10^8	190°

Flare	Loop	ϕ	$t_\circ$ (d)	$N_\circ$ (cm^{-3})	$\alpha_\circ$
1	1	0.50	0.00	5×10^7	100°
2	2	0.97	3.04	1×10^7	0°

at the time of the two flares; the flaring loop has been shadowed for the sake of clarity. In Fig. 4.10 the computed light curve is compared with the observations. As it can be seen, the theoretical curve agrees very well with the observed one, except for some small differences that could be due to the simplified assumptions of the model. For example the fact that the rotation axis is inclined with respect to the line of sight could explain the rapid flux decreases if the source, instead of at the equator, is located at high latitudes in the southern emisphere, where it can be completely eclipsed during the stellar rotation.

The case of the HR 1099 observations by Feldman et al. (1978) is more complex. As we have said, in February 1978 this system underwent a series of outburts that lasted nearly nine days (about three orbital periods) with a mean of one burst per day (Fig. 4.4), and flux densities up to ~ 1 Jy. In this case there are no simultaneous optical observations available, so we do not know the spot distribution on the stellar surface. However, as already mentioned, if we plot the light curve as a function of orbital phase we see that all the emission peaks fall around three well defined phases, with a slight drift towards higher phases in successive periods; this suggests the presence of three active regions on the stellar surface. We have therefore considered three small loops, assuming, for the sake of simplicity, that in the first orbital period a flare occurs in each of them when $\alpha_\circ = 0$. The position of the loops at the time of the following flares has been determined by the phase of the corresponding peaks: the fact that they

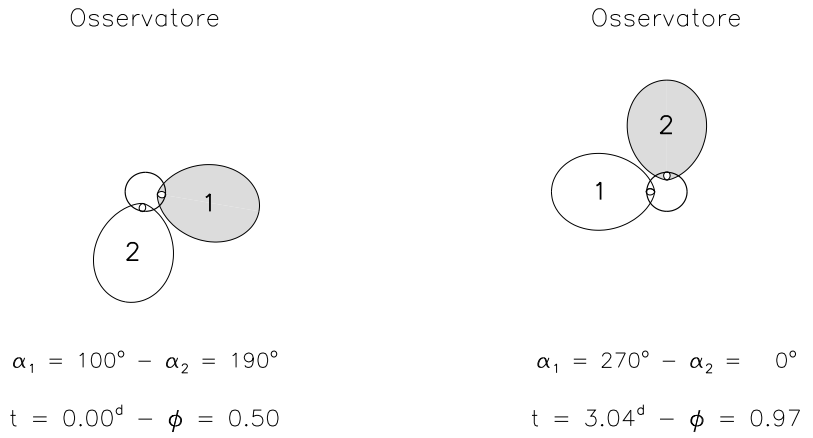

Fig. 4.9 Position of the two loops on UX Ari with respect to the observer at the time of the two flares. For each time, the flaring loop has been shadowed for the sake of clarity.

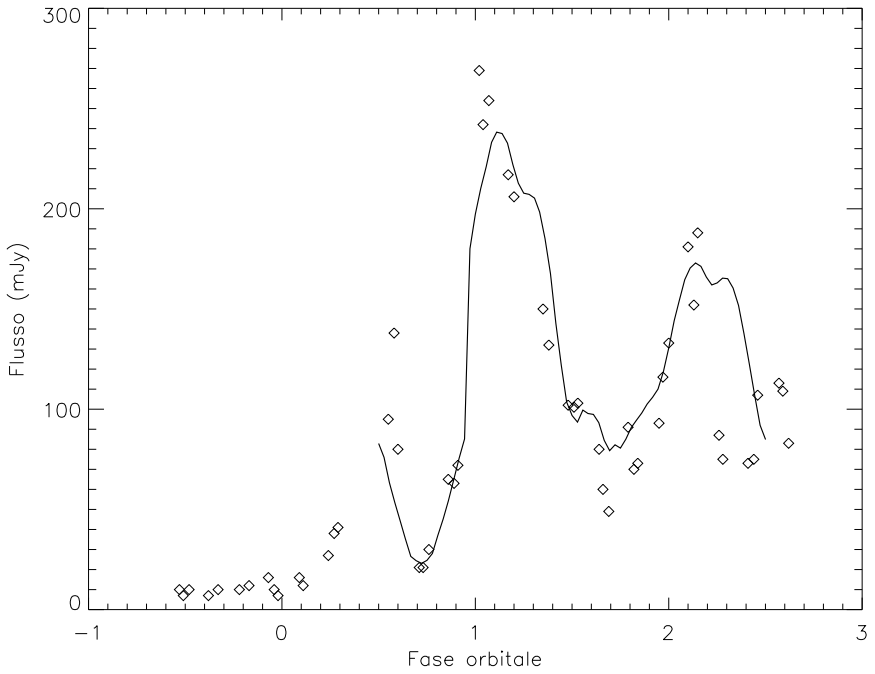

Fig. 4.10 Comparison between the light curve of UX Ari observed by Elias et al. (1995; diamonds) and the computed one (solid line). The rising phase before $\phi = 0.5$ has not been computed, having assumed an impulsive rise of the flare. The first flare occurs at $\phi = 0.5$ and the second at $\phi \sim 1$. For $\phi > 1$ both loops contribute to the total emission. The used parameters are shown in Tab. 4.1.

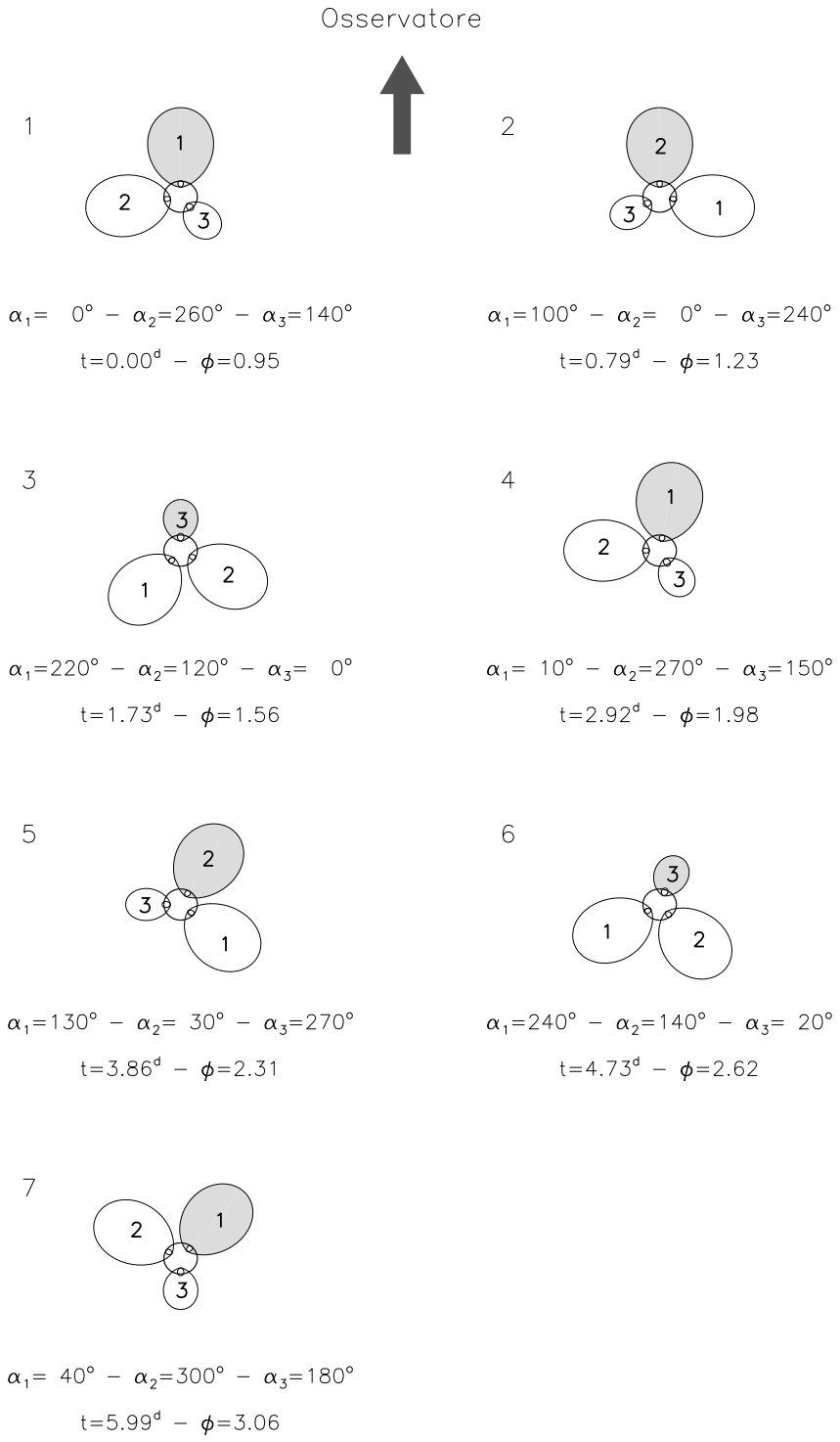

Fig. 4.11 Geometry of the loops on the system HR 1099 with respect to the observer at the time of the flares in February 1978. For each time, the flaring loop has been shadowed for clarity. The parameters relative to the seven flares are given in Tab. 4.2.

drift towards higher orbital phases can be simply explained by assuming that at the time of the flare the loop has a position $\alpha_\circ > 0$. We have considered only the stronger peaks, neglecting the two weaker ones at the end of the observation that can be due to low-energy flares or to emission residuals from the source. Contrary to the case of UX Ari, we considered the possibility that the three loops could have also different sizes in addition to different physical parameters, and that subsequent flares in the same loop were due to energy distributions of relativistic electrons with different total number density $N_\circ$; for the sake of simplicity we have however assumed that the exponent δ of the distribution was the same for all flares and for all loops ($\delta = 2$).

In Tab. 4.2 we give the values of the parameters that better reproduce the observed light curve. The flares occur when the corresponding loop is at the centre of the stellar disk, with the axis directed toward the observer or at a small angle. The system geometry with respect to the observer at the time of the seven considered flares is shown in Fig. 4.11, while the comparison between the observed and theoretical light curve is shown in Fig. 4.12. As it can be seen there is a very good agreement, in spite of the great difference between the adopted geometry of our model and the real geometry of the system HR 1099, whose axis has a low inclination with respect to the line of sight and the star is therefore observed nearly pole-on. The two smaller peaks at the end of the observing period can also be reproduced considering two other small flares occurring in the second and third loop.

We have therefore seen that a model which takes into account both the time evolution of the emission during the flare decay and the system rotation is able to successfully reproduce the light curves observed during active periods.

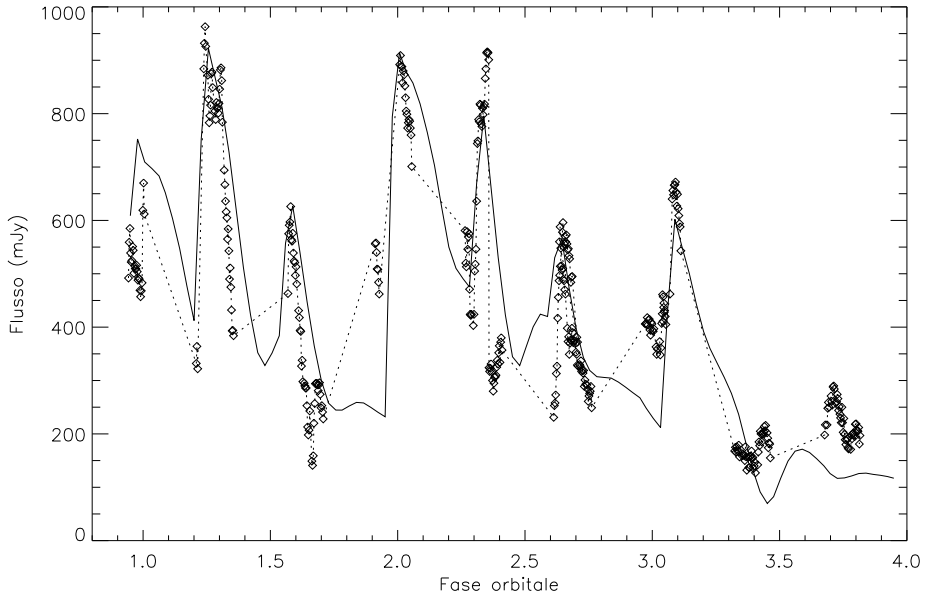

Fig. 4.12 Comparison between the HR 1099 light curve observed by Feldman et al. (1978; diamonds) and the computed one (solid line); for the sake of clarity the observed data points have been connected with a dotted line. The computed light curve is the sum of the contribution of the three loops. The adopted values of the parameters are given in Tab. 4.2.

Tab. 4.2 Parameters used to reproduce the observations of HR 1099 by Feldman et al. (1978). The orbital period of HR 1099 is $P_{\rm orb} = 2.84^{\rm d}$.

Loop	Θ	$R_{\rm spot}$	$B_{\rm max}$ (G)	$n_{\rm e}$ (cm^{-3})	$\alpha(t=0)$
1	40°	15°	3000	10^8	0°
2	40°	15°	3000	10^8	260°
3	40°	10°	3000	10^8	140°

Flare	Loop	ϕ	$t_\circ$ (d)	$N_\circ$ (cm^{-3})	$\alpha_\circ$
1	1	0.95	0.00	2×10^6	0°
2	2	1.23	0.79	1×10^6	0°
3	3	1.56	1.73	5×10^5	0°
4	1	1.98	2.92	2×10^6	10°
5	2	2.31	3.86	5×10^5	30°
6	3	2.62	4.73	5×10^5	20°
7	1	3.06	5.99	5×10^5	40°

CAPITOLO 5

CIRCULAR POLARIZATION OF THE RADIO EMISSION

§ 5.1 Introduction

In the previous chapters we have considered the interpretation of the properties of the total flux density of RS CVn and Algol-type systems: as we have seen, the gyrosynchrotrom mechanisms is able to successfully reproduce the observed spectra and light curves, as well as the source structure during both high-activity and quiescent phases. We have however neglected a very important property of the radio emission from these systems, namely the circular polarization of the radiation which can reach quite high values, expecially in RS CVn systems. The interpretation of the polarization observed in the stellar case is not always straightforward, and for this reason it has not been widely exploited; however, the circular polarization of radio emission from active stars is almost the only diagnostic available for studying the structure of magnetic fields in the coronae of these systems, and it is therefore important to try to understand its properties thoroughly.

The properties of circular polarization in RS CVn systems have been studied for several years, however, despite the available data, they have remained a puzzle. In this chapter we will compare the polarization properties, deduced from previous and new observations, with the predictions of gyrosynchrotron models, evidentiating the difficulties encountered in their interpretation. In particular, we will propose a new interpretation for the observed reversal of

polarization of the quiescent emission at low frequencies, suggesting that it is due to the presence of a weak coherent component.

§ 5.2 Circular polarization properties and results of current models

As mentioned in Chapt. 1, only during the past few years, thanks to the advent of more sensitive radiotelescopes, have reliable multiwavelength observations of the circular polarization of the emission from RS CVn systems become available, expecially for the most active systems UX Ari, HR 1099 and HR 5110 (Pallavicini et al. 1985; Mutel et al. 1987; Willson & Lang 1987; White et al. 1990b; Massi & Chiuderi Drago 1992; Su et al. 1993; Umana et al. 1993; Fox et al. 1994; Jones et al. 1994). The polarization properties have been analyzed for the first time by Mutel et al. (1987), who observed a sample of RS CVn stars at 1.4, 4.9 and 15 GHz during a period of three years and compared their results with the few previously-published data; these properties have been confirmed by later observations.

Radio emission from RS CVn systems is characterized by a degree of circular polarization π_c anticorrelated with the flux density: while the quiescent component can reach values of π_c up to 40 %, flares are generally unpolarized or weakly polarized ($\pi_c \lesssim 10$ %). Moreover, the observed degree of polarization depends on the inclination i of the stellar rotation axis with respect to the line of sight: the maximum degree of polarization is observed for systems with low i, such as HR 5110, HR 1099 and UX Ari, while it is very low for eclipsing systems ($i \sim 90°$), such as AR Lac and Algol-type systems. For non-eclipsing systems there is often a reversal in the sense of polarization between 1.4 and 5 GHz (HR 5110 has always been found to be unpolarized at 1.5 GHz); this reversal is independent of the spectral shape, and is observed both during flares, with positive spectral indexes, and during quiescent phases, with flat or decreasing spectra. Moreover, for the best studied objects the sense of polarization at a given frequency has been observed to be nearly always the same over more than 15 years: generally at frequencies above 5 GHz the sense of polarization is right-hand (Stokes parameter $V > 0$) for HR 1099 and HR 5110 and left-hand

($V < 0$) for UX Ari. This fact implies that the polarized emission is associated with a large-scale magnetic field, possibly linked to the polar spots (one of which is always visible in these systems) and not to loops anchored on low-latitude spots: in the latter case in fact the stellar rotation would cause a modulation of the sense of polarization, which would change sign during the orbital period, in contrast with observations.

As mentioned in Chapt. 1, the commom interpretation for the presence of circular polarization together with high brightness temperatures is gyrosynchrotron emission from mildly relativistic electrons. Owen et al. (1976) first suggested that emission from an optically thick, self-absorbed source could explain the observed properties of flares, such as the low degree of polarization and the shape of the spectrum; in particular the polarization reversal can be explained as the transition from an optically thin source at higher frequencies to an optically thick one at lower frequencies. In the case of the 1978 flare observed on HR 1099, Borghi & Chiuderi Drago (1985) have shown that both the shape of the spectrum and the observed polarization reversal between 1.4 and 5 GHz can be obtained with a simple model with uniform magnetic field and a density of relativistic electrons which decreases with the distance from the star. However this model cannot be applied to the quiescent emission, since it predicts that the polarization should change sign at a frequency where the spectral index is positive, whereas at low activity levels the reversal is observed to occur at frequencies where the spectrum is flat or decreasing.

VLBI observations of a *core-halo* source structure (Mutel et al. 1985; Lestrade et al. 1988) have led some authors to consider simple source models consisting of two homogeneous sources of different size and magnetic field strength. As pointed out by Mutel et al. (1987), a two-component model can explain the presence of a polarization reversal together with a flat spectrum, provided that the magnetic fields in the two sources have opposite orientations with respect to the line of sight.

Recently Morris et al. (1990) have proposed a two-dimensional magnetospheric model to interpret the radio emission from late-type active stars. These authors assume the source consists of a toroidal region, threaded by dipolar field

lines, which contains thermal plasma and a trapped non-thermal distribution of relativistic electrons emitting gyrosynchrotron radiation. For the special case of a pole-on view, they find that only a few sets of parameters are consistent with the observations of the flaring and quiescent emission; in particular, the only way to obtain, for the quiescent component, a reversal in the sense of circular polarization with $\alpha \lesssim 0$ is to assume that the relativistic electron density increases strongly with radial distance.

A similar conclusion was reached also by Jones et al. (1994) in the case of a three-dimensional dipole field with a spherically symmetric relativistic electron density. In order to reproduce both the frequency of reversal and the observed degree of circular polarization they find that the magnetic field geometry should be an arcade of loops, with the emitting electrons confined only to a thin shell at a distance of about $2\,R_\star$ from the stellar surface.

§ 5.3 Results of models in the case of a homogeneous source

In order to interpret the observed polarization properties, we have first computed the spectrum and polarization of gyrosynchrotron emission from a homogeneous source, for different values of the source parameters. Emission in a vacuum as well as in a medium with uniform thermal plasma density $n_{\rm e}$ and temperature T has been considered; in the latter case Razin suppression and free-free emission and absorption have been taken into account. For the temperature, as in the previous chapters, we have adopted a mean value $T = 1.5 \times 10^7$ K for the hot coronal plasma component based on recent X-ray observations (Dempsey et al. 1993).

We have assumed that the source has a cylindrical shape, with projected surface area $S = \pi\,(L/2)^2$ and dimension L along the line of sight; L has been chosen to be of the order of the binary separation, in agreement with VLBI observations of the quiescent component (Mutel et al. 1985; Lestrade et al. 1988; Massi et al. 1988). The magnetic field B is considered uniform within the source and making an angle θ with the line of sight.

The distribution of relativistic electrons has been assumed to have a power-

law energy spectrum of the form given in Eq. (2.14), with total number density of particles $N_\circ$. The emissivity $j^\pm$ and the absorption coefficient $k^\pm$ for the ordinary (+) and extraordinary (−) modes have been computed using the approximate expressions (2.8) derived by Klein (1987). In the assumption that the two modes propagate independently we can solve the transfer equation separately for the two radiation modes; the emergent Stokes parameters I (total intensity) and V (circularly-polarized intensity) can then be obtained by combining the intensities $I^\pm$ using the relations (Ramaty 1969):

$$\begin{aligned} I &= I^- + I^+ \,, \\ V &= (I^- - I^+)\,\frac{2a_{\theta+}}{1+a_{\theta+}^2} \,, \end{aligned} \tag{5.1}$$

where $a_{\theta+}$ is the polarization coefficient of the ordinary mode, defined in Eq. (2.11), and we have adopted the convention that $V > 0$ (right-hand polarization) when the polarization is in the sense of the extraordinary mode for a magnetic field directed towards the observer ($\cos\theta > 0$). The degree of circular polarization is then $\pi_c = V/I$.

We have investigated the trend of the spectrum and circular polarization between 1 and 30 GHz for different values of the parameters δ, $N_\circ$, θ, B and n_e. Specific examples of how the flux and polarization spectra change when the source parameters are varied are shown in Fig. 5.1. The results obtained for the polarization show that:

1) the degree of circular polarization has a maximum at a certain frequency near the spectral peak and then decreases at higher frequencies where the source is optically thin, as numerous other studies have shown (e.g., Dulk & Marsh 1982);
2) the polarization is always in the sense of the extraordinary mode ($V > 0$) in the optically thin part of the spectrum, and reverses its sense at a certain frequency below the spectral peak;
3) the peak degree of polarization is greater for greater values of B and δ, while it decreases if θ or $N_\circ$ are increased. This latter result is consistent with the observation of smaller degrees of polarization at higher flux levels, when presumably the number of relativistic electrons in the source is greater than

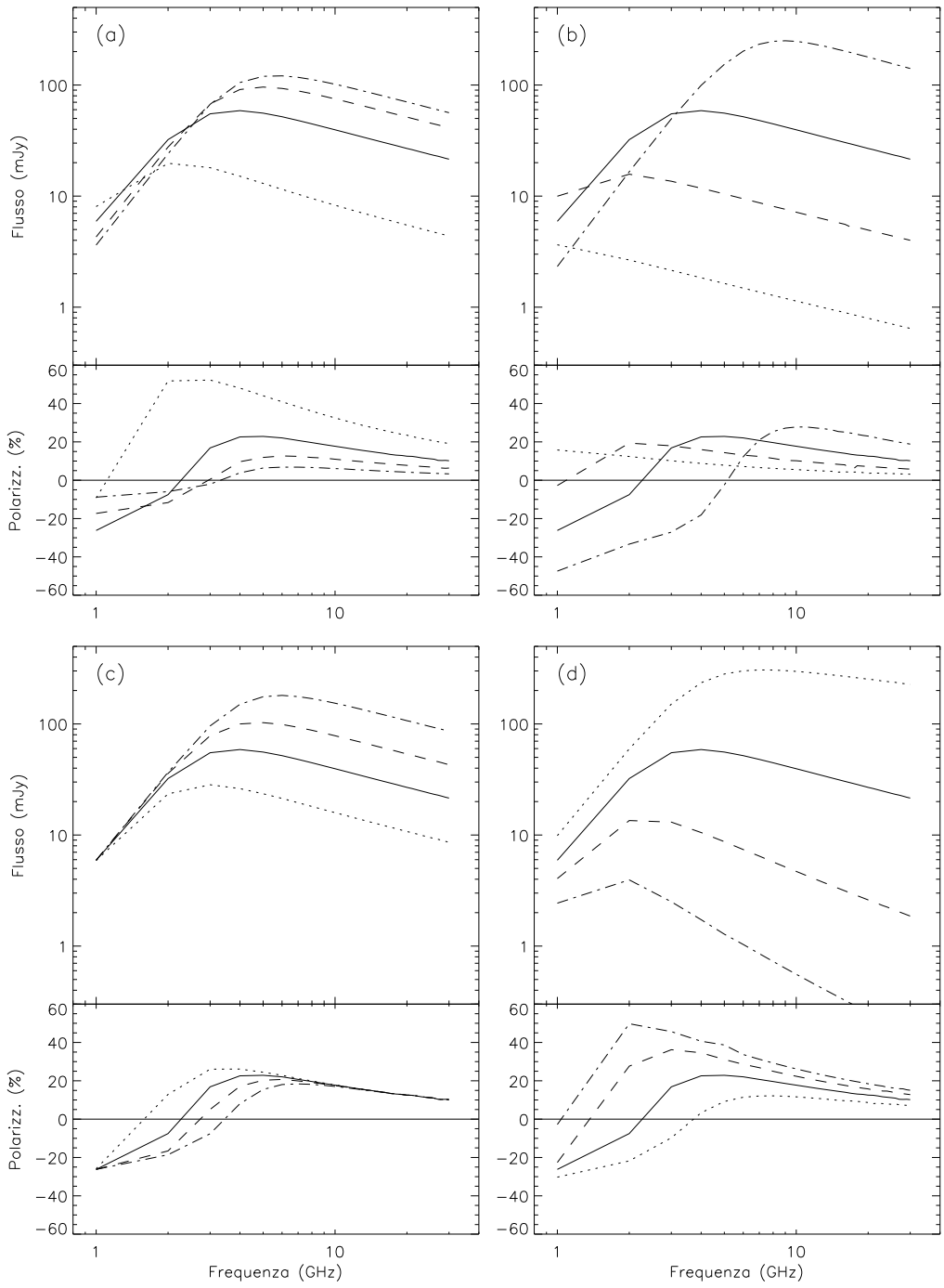

Fig. 5.1 Variation of the spectra and polarization for a homogeneous source for different values of the parameters θ (a), B (b), $N_\circ$ (c) and δ (d). In all panels the solid curve was obtained for $\delta = 2$, $B = 30$ G, $\theta = 30°$, $N_\circ = 5 \times 10^3$ cm^{-3}. The dotted, dashed and dot-dashed lines correspond, respectively, to: (a) $\theta = 10°$, $50°$, $70°$; (b) $B = 3$, 10, 100 G; (c) $N_\circ = 2 \times 10^3$, 10^4, 2×10^4 cm^{-3}; (d) $\delta = 1.5$, 2.5, 3.

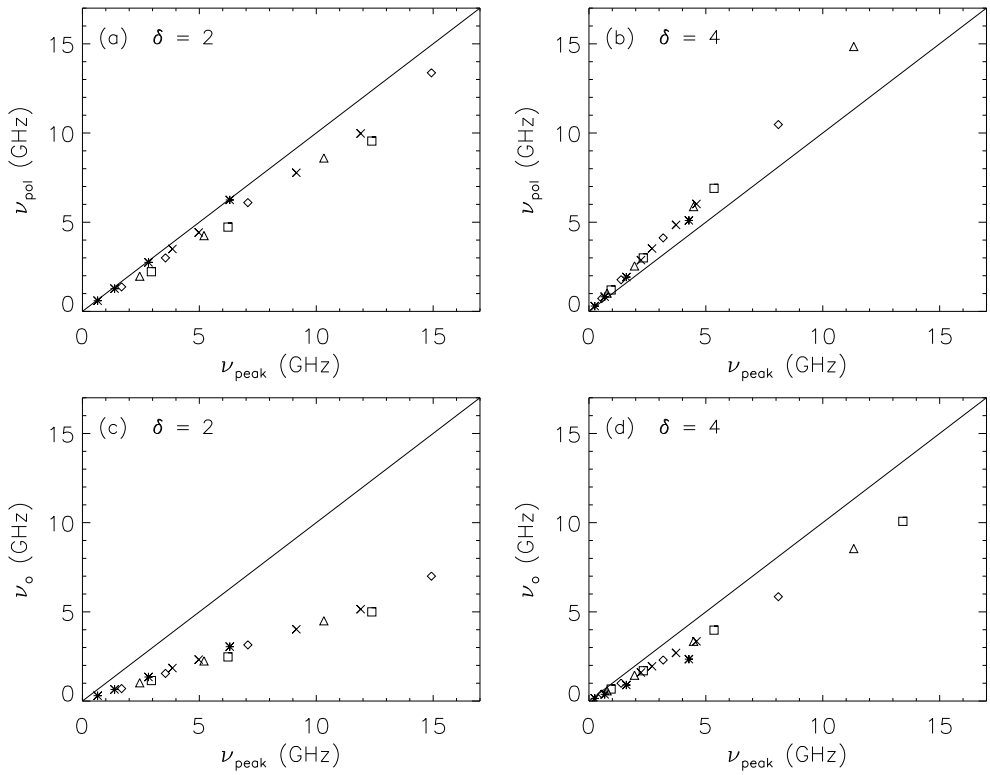

Fig. 5.2 Behaviour of the frequencies $\nu_{\rm pol}$ and $\nu_{\rm o}$ as a function of $\nu_{\rm pk}$, for a series of homogeneous gyrosynchrotron models of varying δ, θ, B and $N_{\rm o}$. The panels show $\nu_{\rm pol}$ as a function of $\nu_{\rm pk}$ for $\delta = 2$ (a) and $\delta = 4$ (b); and $\nu_{\rm o}$ as a function of $\nu_{\rm pk}$ for $\delta = 2$ (c) and $\delta = 4$ (d). The points shown refer to calculations in a vacuum, with $B = 3$, 10, 30, 100 G, $N_{\rm o} = 5 \times 10^3$ cm^{-3} ($\delta = 2$) and 10^6 cm^{-3} ($\delta = 4$), $\theta = 10°$ (asterisks), 30° (diamonds), 50° (triangles), 70° (squares); and with $\theta = 30°$, $B = 30$ G, $N_{\rm o} = 10^3$, 2×10^3, 10^4, 2×10^5, 2×10^6, 5×10^6 cm^{-3} for $\delta = 2$ and $N_{\rm o} = 2 \times 10^5$, 5×10^5, 2×10^6, 5×10^6 cm^{-3} for $\delta = 4$ (crosses).

during low activity periods.

Fig. 5.2 shows the relationships between the frequency at which the total flux density is maximum, $\nu_{\rm pk}$, the frequency at which the polarization degree is maximum, $\nu_{\rm pol}$, and the frequency at which the sense of polarization reverses, $\nu_{\rm o}$, in the two cases $\delta = 2$ and $\delta = 4$. In the figure the frequencies obtained for different values of θ, B and $N_{\rm o}$ are plotted, in the case of emission in a vacuum. As it can be seen, for a fixed value of δ, and therefore for a fixed electron energy spectrum, there is a very good linear correlation between these frequencies (i.e., $\nu_{\rm pol} \propto \nu_{\rm pk}$ and $\nu_{\rm o} \propto \nu_{\rm pk}$) which is largely independent of the

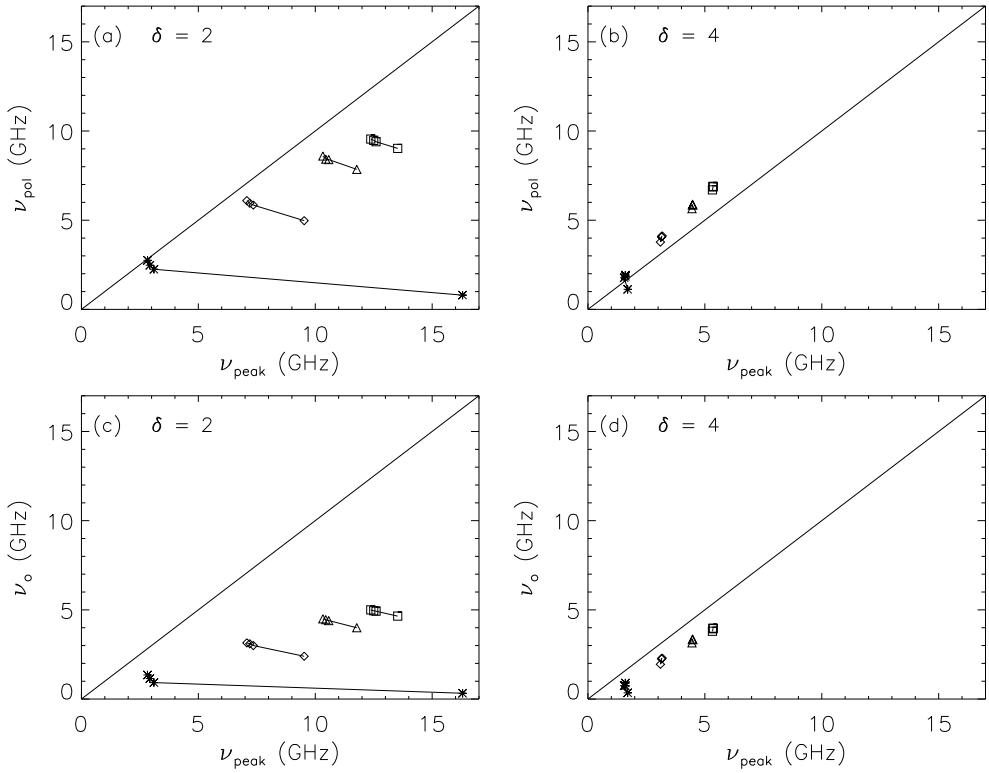

Fig. 5.3 Effect of a thermal plasma on the relationships shown in Fig. 5.2. The panels are the same as in Fig. 5.2 except that the values of B and N_o are fixed while n_e varies, for four different values of θ. Points with the same θ but differing n_e are joined by solid lines. The parameters are $B = 30$ G, $N_o = 5 \times 10^3$ cm^{-3} ($\delta = 2$) and 10^6 cm^{-3} ($\delta = 4$), $n_e = 0$, 5×10^7, 10^8, 5×10^8 cm^{-3}, $\theta = 10°$ (asteriscs), $30°$ (diamonds), $50°$ (triangles) and $70°$ (squares). The points most distant from the linear relationship correspond to $n_e = 5 \times 10^8$ cm^{-3}.

parameters θ, B and N_o. The slopes of the linear relationships do depend on the energy spectrum, being greater for greater values of δ.

To investigate the effect of the ambient thermal plasma on ν_{pol} and ν_o, in Fig. 5.3 we present the same relationships for fixed values of B and N_o, with varying n_e, for four different values of θ. Points with the same value of θ are joined by a solid line. Both relationships are practically unaffected by the medium until the plasma density is so high ($n_e = 5 \times 10^8$ cm^{-3}) that the spectrum becomes strongly suppressed at low frequencies due to the Razin effect.

Therefore, in the absence of a significant Razin effect, which should be

discernible in the spectrum, the homogeneous model predicts a general linear relationship between $\nu_{\rm pk}$, $\nu_{\rm pol}$ and $\nu_\circ$, which is independent of the source parameters, but depends only on the value of the energy distribution exponent δ, which can be determined from the observed spectral index in the optically thin part of the spectrum. In particular we find always $\nu_{\rm pol} \simeq \nu_{\rm pk}$ and $\nu_\circ < \nu_{\rm pk}$, i.e., the peak degree of circular polarization coincides with the spectral peak, but the polarization reversal due to self-absorption occurs in a region where the spectral index is positive.

This result is inconsistent with the observations of RS CVn systems: in fact, as pointed out in the previous section, the polarization reversal occurs generally between 1.4 and 5 GHz independently of the position of the spectral peak, and in most cases the polarization peaks at a much higher frequency than does the flux spectrum.

§ 5.4 Extension to inhomogeneous models

Homogeneous models are a convenient tool because of their simplicity and the limited number of free parameters they involve, but we do not expect that they are a good representation of stellar radio sources. The appropriate question to ask is, therefore, what general properties of the polarization of homogeneous sources also apply to inhomogeneous sources.

If we think of an inhomogeneous source as a collection of several homogeneous sources, all having the same form of the electron energy distribution, we can make the following considerations. In the frequency range where all sources are optically thin, the total spectrum is given by the sum of the single spectra and the emission is thus dominated by the region of the source in which $B \sin\theta$ is largest. It follows that in such an inhomogeneous source the property of homogeneous models that circular polarization decreases as frequency increases above the spectral peak will also hold, although with the complication that the spectral peak frequency is not the same for all sources. This fact does not allow us to extrapolate to the inhomogeneous case the relationships between the frequencies $\nu_{\rm pk}$, $\nu_{\rm pol}$ and $\nu_\circ$. The calculations of polarization performed with the

inhomogeneous models described in the previous chapters however confirm the properties derived in the homogeneous case, i.e. that the polarization degree peaks close to the spectral peak and that the polarizazion reverses below the peak, in the optically thick part of the spectrum.

Some authors investigated the possibility of obtaining optically thick spectra with a flat or decreasing trend, in order to explain in a simple way the polarization reversal. Jones et al. (1994) analyzed a set of dipole models and concluded that it is very difficult to achieve a degree of polarization larger than 1 % at optically thick frequencies, and that in order to obtain the observed flat spectra in the assumption of an optically thick source the non-thermal electron density must increase with the distance from the star, as found also by other authors (Drake et al. 1987; Morris et al. 1990). According to White et al. (1989), it is also possible to obtain optically thick flat spectra without requiring that density increase with height: it is in fact sufficient to assume that both the energetic electron density and the magnetic field strength fall slowly as height above the stellar surface increases. However, the difficulty of obtaining the observed values of circular polarization with an optically thick source still remains.

§ 5.5 Observations of coherent emission

As part of a project to study the long-term evolution of the polarization of RS CVn systems (White 1996), we have been observing the three brightest and most polarized systems (HR 1099, UX Ari and HR 5110) with the VLA, at regular intervals of about 4 months since June 1993. Figs. 5.4 (HR 1099, July 5, 1993) and 5.5 (UX Ari, April 23, 1994) show two examples of the behaviour of the light curves in left (L) and right (R) circular polarization at 1.4 GHz. In each case the observation lasted $\sim$ 20 min and data were obtained at two sidebands, each of 50 MHz bandwidth and centered on 1385 MHz and 1415 MHz, respectively. In Fig. 5.4 we plot R and L for 1385 MHz, together with total intensity data in subsequent scans at 4535 and 8065 MHz; Fig. 5.5 shows instead R and L for both 1385 and 1415 MHz, in order to compare the

behaviour at the two sidebands; the data points are each 10 seconds apart. In both these examples the stars were relatively bright. Fig. 5.4 shows that the left circular polarization received from HR 1099 was up to twice as strong as the right, and while R was steadily increasing over the 20-minute observation, L was fluctuating rapidly on timescales as short as 10 s, but overall showed a clear decreasing trend. In Fig. 5.5 we see that UX Ari was steady at L, but showed rapid fluctuations in R. From the similarity of the 1385 and 1415 MHz time profiles in Fig. 5.5, it is clear that the rapidly fluctuating component is quite broadband, and this was true for HR 1099 also: in both cases in fact there appears to be little significant difference in the emission between the two sidebands 30 MHz apart.

To ensure that the observed fluctuations in one polarization were real and not instrumental, we studied the time profiles of the two polarizations for a strong background source in the field of view of HR 1099. Such background sources are almost always extragalactic objects which should have essentially no circular polarization, and should not vary on such short timescales. This was found to hold true for the background source we investigated, indicating that the fluctuations observed in HR 1099 were not instrumental artefacts.

The most important characteristics of these observations are that the circular polarization is predominantly due to a broadband component which has small variations on very short timescales, but appears to be slowly modulated on longer timescales. If the observations did not have adequate signal-to-noise, needing longer integration times we would be unable to see the small rapid fluctuations, but the slower modulation would be evident. The rapid fluctuations are characteristic of a coherent emission process, such as plasma emission or cyclotron maser emission (e.g. see Dulk 1985; Melrose 1991), which are able to produce very high degrees of circular polarization. The slower modulation could be mistaken for an incoherent process such as gyrosynchrotron emission.

In both our observations, the sense of the predominant circular polarization at 1.4 GHz is opposite to that at higher frequencies. On July 5, 1993 the polarization of HR 1099 was -29 % at 1.4 GHz, $+7$ % at 5 GHz and $+10$ % at 8 GHz; on April 23, 1994 that of UX Ari was $+11$ % at 1.4 GHz, -1 % at

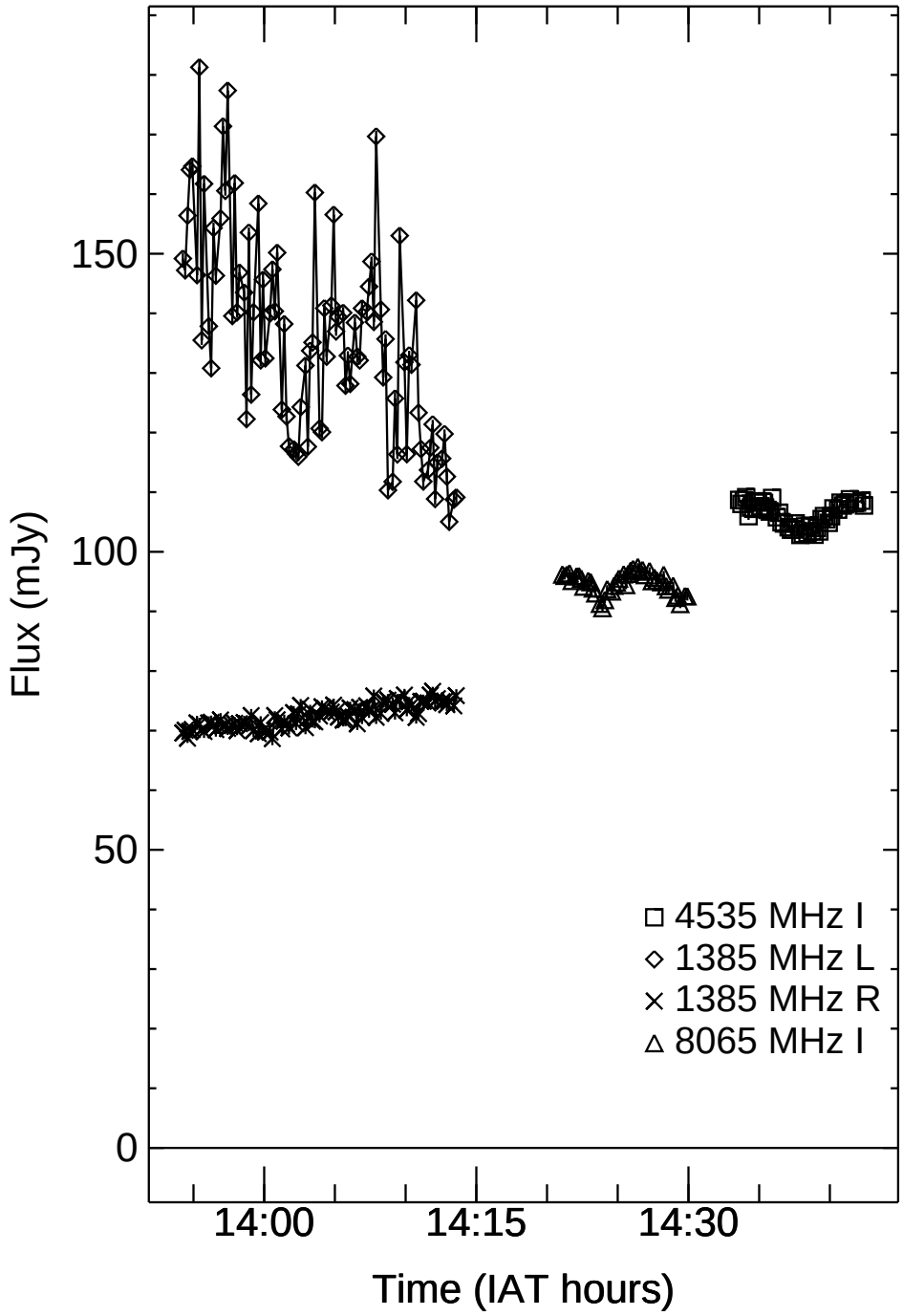

Fig. 5.4 Time profiles of right (R; crosses) and left (L; diamonds) circular polarization at 1.385 GHz during a VLA observation of HR 1099 on July 5, 1993. Data are plotted every 10 sec. The total intensity observed at 4.5 GHz (squares) and 8.1 GHz (triangles) is also plotted. Error bars of $\pm\sigma$ are plotted on all points.

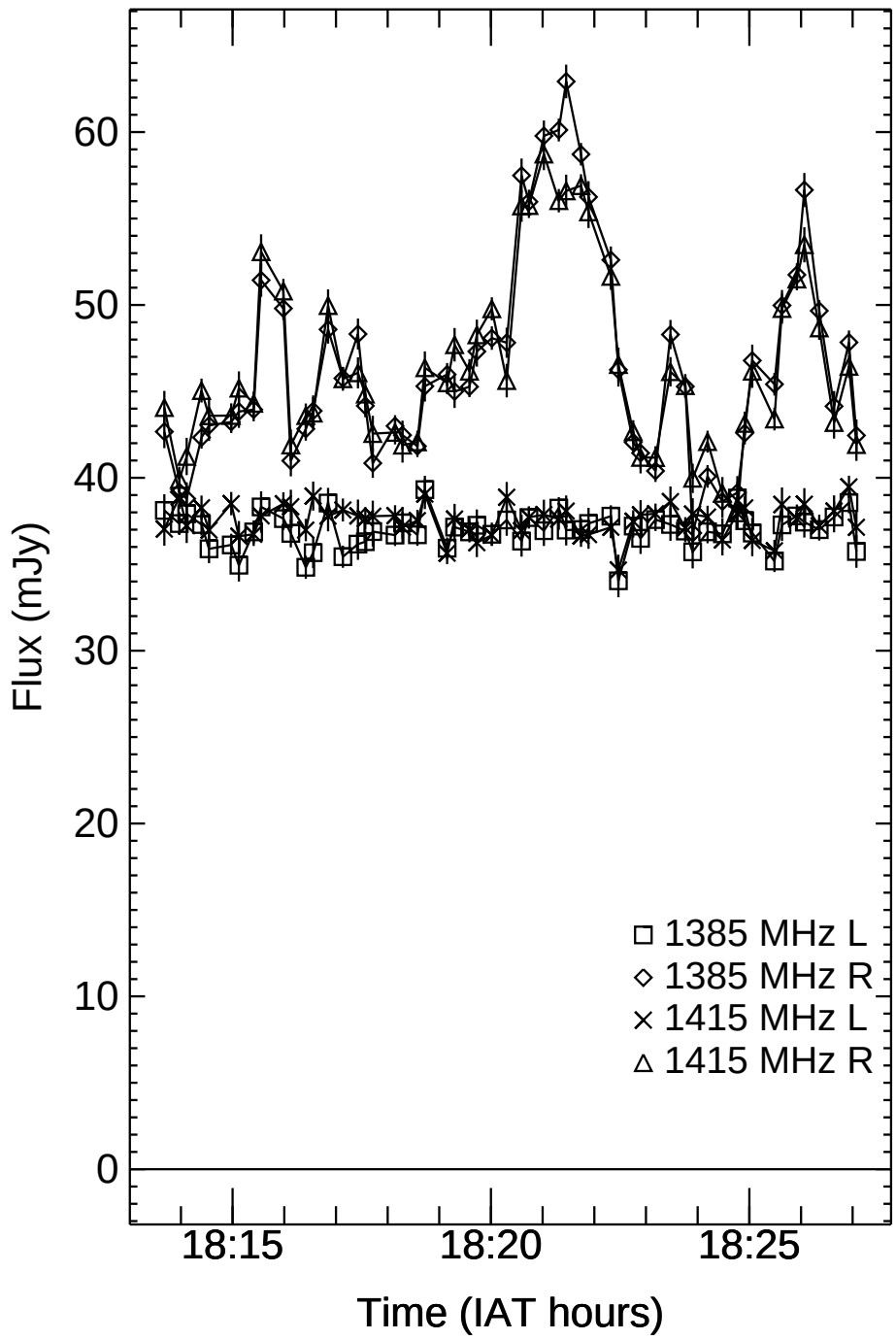

Fig. 5.5 Time profiles of right (R) and left (L) circular polarization during a VLA observation of UX Ari on April 23, 1994. Data are plotted every 10 sec. Observations in the two sidebands at 1385 MHz (squares: L; diamonds: R) and 1415 MHz (crosses: L; triangles: R) are plotted; each sideband had a bandwidth of 50 MHz. Error bars of $\pm\sigma$ are plotted on all points.

5 GHz, − 2 % at 8 GHz and − 3 % at 15 GHz. This is exactly the behaviour attributed to the quiescent emission of these systems by Mutel et al. (1987).

Highly polarized emission has often been seen in these systems previously, and has generally been described as flare-related emission. Mutel & Weisberg (1978) and Fix et al. (1980) observed HR 1099 at $1.4 - 1.7$ GHz at Arecibo and saw left circular polarization of up to 75 %, with rapid variability; on UX Ari Mutel & Weisberg (1978) found right circular polarization of up to 20 %. Brown & Crane (1978) measured left circular polarization of up to 40 % on HR 1099 at 2.7 GHz, and found it to vary on timescales shorter than 1 hour. Gibson et al. (1978) measured rapid variability at 1.4 GHz on HR 1099, but with no polarization data. Simon et al. (1985) detected a highly left-circularly-polarized (86 %) flare from AY Ceti at 1.5 GHz, while Lestrade et al. (1988) saw up to 70 % left circular polarization from Algol at 1.7 GHz. The latter example, also obtained with the VLA, appears quite similar to Figs. 5.4 e 5.5, with one polarization (R, in the case of Algol) steady while the other shows rapid but small fluctuations superimposed on a steady level of emission. It should be noted that all of these examples of highly-polarized emission occurred at a frequency below 3 GHz.

In most of the examples cited above, the highly-polarized component was attributed to an outburst due to a coherent emission mechanism. On the basis of Figs. 5.4 e 5.5, however, it is clear that only a portion of the emission at 1.4 GHz is due to such a mechanism: the steady level of emission seen in the weaker polarization is clearly not related to the rapidly fluctuating component in the stronger polarization. Thus in this case a combination of two sources of emission is present: a possibly weakly-polarized component which is steady, and a highly-polarized component, possibly 100 % polarized, which has rapid fluctuations on a short timescale, but a more gentle modulation on a longer timescale. We suggest that the most likely mechanism for the highly-polarized emission is plasma emission. The main argument in favour of this is that the polarization detected at high frequencies, where the radio spectrum is falling and the source should be optically thin, should represent the extraordinary mode (x-mode) for gyrosynchrotron emission. Since the low-frequency polarization

is in the opposite sense, it probably represents the ordinary mode (o-mode), which is characteristic of plasma emission. On the Sun plasma emission comes in many different guises; the form which is closest to that seen in these stars is the noise storm emission common at frequencies between 200 and 500 MHz (Kai et al. 1985): it is broadband, typically 100 % polarized in the sense of the o-mode, and can exhibit both rapid fluctuations as well as a slower modulation. From the observed very high degrees of polarization we infer that the o-mode emission is at the fundamental of the plasma frequency, i.e., $\nu = \nu_{\rm p} \simeq 9000\sqrt{n_{\rm e}}$, and hence arises in a region of the corona where the ambient electron density $n_{\rm e} \sim 2 \times 10^{10}$ cm^{-3}.

§ 5.6 Interpretation of the polarization reversal at low frequencies

Based on the observations of low-frequency polarization discussed in the previous section, we suggest a new interpretation for the polarization reversal of the quiescent emission observed at frequencies below 5 GHz. Presently this polarization reversal is attributed either to the intrinsic o-mode polarization of self-absorbed gyrosynchrotron emission, or to the combination of several gyrosynchrotron components, each with a spectral peak located conveniently to reproduce the observed properties. As noted above, the occasional very large degrees of polarization observed at low frequencies and the location of the inversion with respect to the spectral peak are inconsistent with optically thick models, and the multi-component models are somewhat ad hoc. We suggest instead that the low-frequency polarization is not an intrinsic property of the quiescent gyrosynchrotron emission, but is actually due to the presence of weak but highly-polarized coherent o-mode emission superimposed on a weakly polarized or unpolarized quiescent component. When the highly-polarized component is strong, it is readily identified as something other than quiescent emission, as in the examples shown in Figs. 5.4 e 5.5. Often this highly-polarized component will be rapidly varying, but on other occasions it may vary only slowly and thus be difficult to distinguish from the true quiescent component on the basis of temporal properties alone. Moreover, when the coherent emission is

weaker, the rapid low-level fluctuations would not be detectable due to the limited signal-to-noise in the data, and the slow modulation could be mistaken for the true quiescent emission.

We cannot determine the true sense of polarization of the quiescent component from the available data; however, a few examples seem to indicate that the quiescent emission at 1.4 GHz has the same sense of polarization as observed at high frequencies, and can therefore be attributed to x-mode. On April 23, 1994 the polarization for HR 1099 was + 8 % at 1.4 GHz, + 25 % at 5 GHz, + 31 % at 8 GHz and + 35 % at 15 GHz; Fig. 5.6 shows an observation of HR 1099 at 1.4 GHz on May 15, 1993, lasted for about 6 hours, where the steady emission observed after the decay of the rapidly-variable coherent component is clearly polarized in the opposite sense. Note the long duration of the coherent emission in the latter case (several hours), suggesting the need for a continuous acceleration of electrons and hence a continuous energy release in the source.

The observation by van den Oord & de Bruyn (1994) of a highly-polarized emission at 0.61 GHz from II Peg (up to 90 %) is consistent with our interpretation since, based on the solar analogy, we expect the highly-polarized coherent emission to become more dominant over the weakly-polarized quiescent emission as we go to lower frequencies.

One issue which needs to be addressed is why plasma emission should be observed to be so common at 1.4 GHz in RS CVn and Algol systems, while it is largely confined to lower frequencies on the Sun. The conventional explanation for its absence at higher frequencies on the Sun is the fact that the absorption of plasma emission by the thermal plasma in the corona is a very strong function of frequency: since free-free opacity varies as $n_e^2/T^{1.5}\nu^2$, where n_e is the ambient electron density, and the plasma frequency ν_p varies as $n_e^{0.5}$, the opacity at the plasma frequency rises as a very high power of ν_p (see e.g. Benz 1993). Thus there is a fairly sharp upper limit to the frequency range of plasma emission for a corona of a given temperature, except when very sharp gradients are present in the corona (Benz et al. 1992). However, as already noted in Chapt. 1, the typical temperature of coronal material in RS CVn and Algol systems is at least

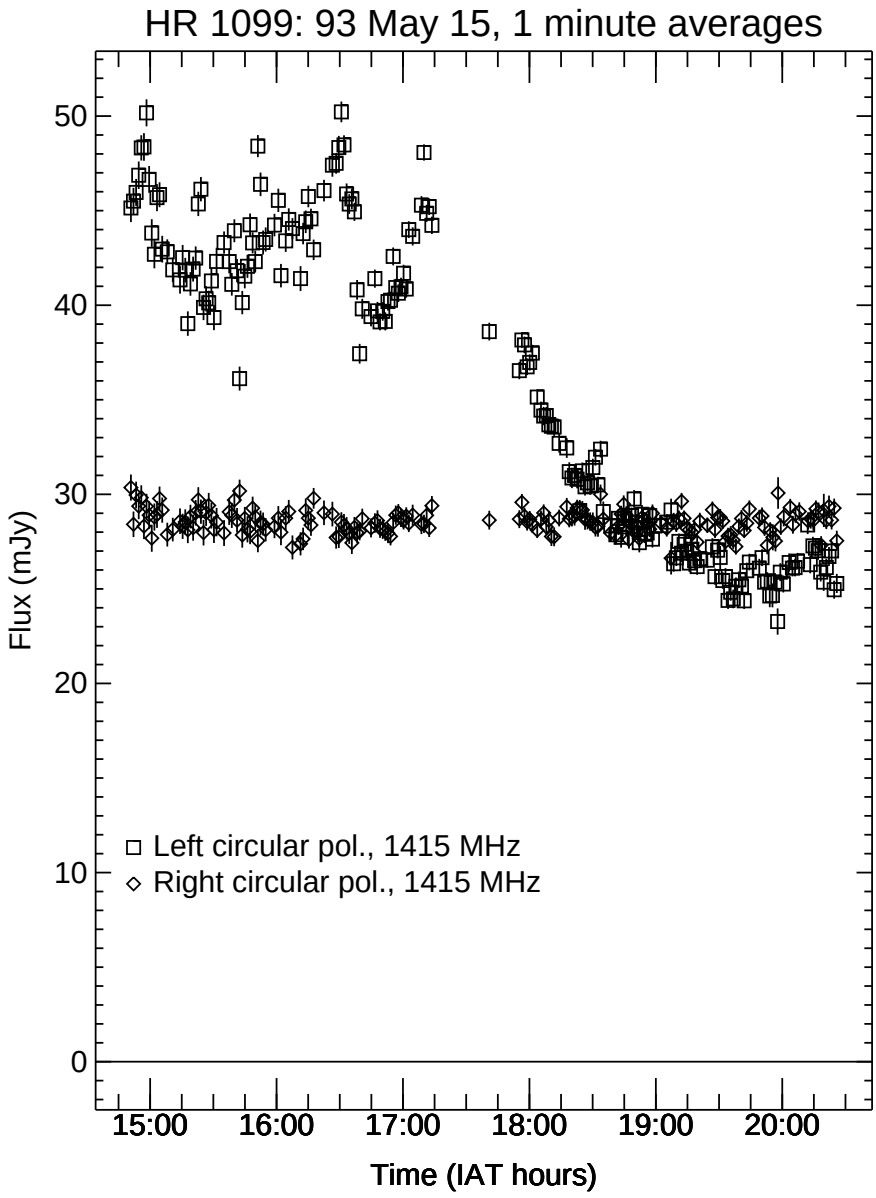

Fig. 5.6 Time profiles of the right (diamonds) and left (squares) circular polarization at 1.415 GHz during a VLA observation of HR 1099 on May 15, 1993. The observation lasted $\sim$ 6 hours and data are plotted in 1-min intervals. Error bars of $\pm\sigma$ are plotted on all points.

an order of magnitude larger than in the solar corona, and this effect will reduce the opacity for plasma emission at a given frequency and allow it to appear at higher frequencies than on the Sun.

As noted earlier, the three systems UX Ari, HR 1099 and HR 5110 are all

observed roughly pole-on, and this fact is believed to be crucial in making them highly polarized compared with eclipsing systems such as AR Lac and Algol (Mutel et al. 1987): as mentioned in Chapt. 1, most studies of the magnetic field structure on active stars led to the conclusion that there are large long-lived polar spots on the stellar surface, and since the systems are pole-on we only ever see a spot of one polarity, which also explains the observed consistency in polarization over long timescales (Mutel et al. 1987; White 1996). On the other hand in eclipsing systems, where emission from both poles is visible, at higher frequencies where the emission is optically thin we can expect a rough cancellation of polarization, which has opposite senses at the two poles, and it would anyway be low since the magnetic field is nearly perpendicular to the line of sight: this explains why the polarization in these systems is generally lower. However, coherent sources are usually more variable than incoherent ones, so it is unlikely that coherent o-mode sources over both poles will have the same strength at all times, and we might expect to see more variability in the observed polarization. It is possible that coherent sources over the poles may be beamed away from us if we are looking at them from the equator: some low-frequency plasma emission on the Sun is known to be beamed, mainly because o-mode emission at the fundamental is emitted in a region with refractive index much smaller than unity, and must refract as it propagates to lower densities (Melrose & Dulk 1988; Lim et al. 1994). In a corona with a predominantly radial density gradient, this effect will cause fundamental plasma emission to be radially beamed, and therefore for a polar source it will be directed away from observers in the equatorial plane. Another consideration is that not all systems will necessarily show the coherent emission reported here: the system HR 5110 for example is a very active radio source, is observed nearly pole-on, and can be highly polarized at 5 GHz (Mutel et al. 1987), but so far it has never shown any circular polarization at 1.4 GHz.

If our interpretation of the polarization reversal is correct, it removes the need for gyrosynchrotron models to reproduce the low-frequency polarization of the quiescent emission observed in these systems, which has proven to be a difficult constraint (e.g. Morris et al. 1990; Jones et al. 1994). In particular, it

may not be necessary for the energetic electron density to increase with distance from the star, as some models of the quiescent emission have required in order to reproduce both the flux spectrum and the polarization reversal. In some cases, the presence of the highly-polarized component will also change the spectrum of the quiescent component considerably: for example, in Fig. 5.4 the spectrum obtained if we assume that the quiescent emission at 1.4 GHz is at the same level of the right circularly polarized emission is quite different from that obtained if we use the total intensity as the quiescent level (the spectrum peaks between 1.4 and 5 GHz, rather than peaking below 1.4 GHz).

§ 5.7 Polarization at high frequencies

In the previous section we proposed a new interpretation of the polarization reversal of the quiescent component, which removes the problems with gyrosynchrotron models. However, as we will see in this section, the behaviour of the degree of polarization at high frequencies is also inconsistent with these models. Figs. 5.7, 5.8 and 5.9 show the flux and polarization spectra of UX Ari, HR 1099 and HR 5110, respectively, obtained from our observations (White & Franciosini 1995) in 1993 and 1994 and from other previously published observations with measurements of at least three frequencies. The previous data are taken from Pallavicini et al. (1985), White et al. (1990b), Su et al. (1993), Umana et al. (1993) and Fox et al. (1994). The dates corresponding to observations from each authors are given in Tab. 5.1. Comparing these observations we see that, except during strong flares which are unpolarized, the degree of circular polarization π_c increases with frequency (in the R sense for HR 1099 and HR 5110, in the L sense for UX Ari), at least up to 15 GHz, independently of the shape of the spectrum. This increase becomes more pronounced as the flux density decreases. Only in one case (UX Ari, August 13, 1994) we observed the polarization peak at 8.4 GHz, which is however still well above the spectral peak frequency ($\lesssim 1.4$ GHz).

Moreover, if we separate the observed quiescent emission in the two oppositely polarized components, we see that this increase of π_c is due to the fact

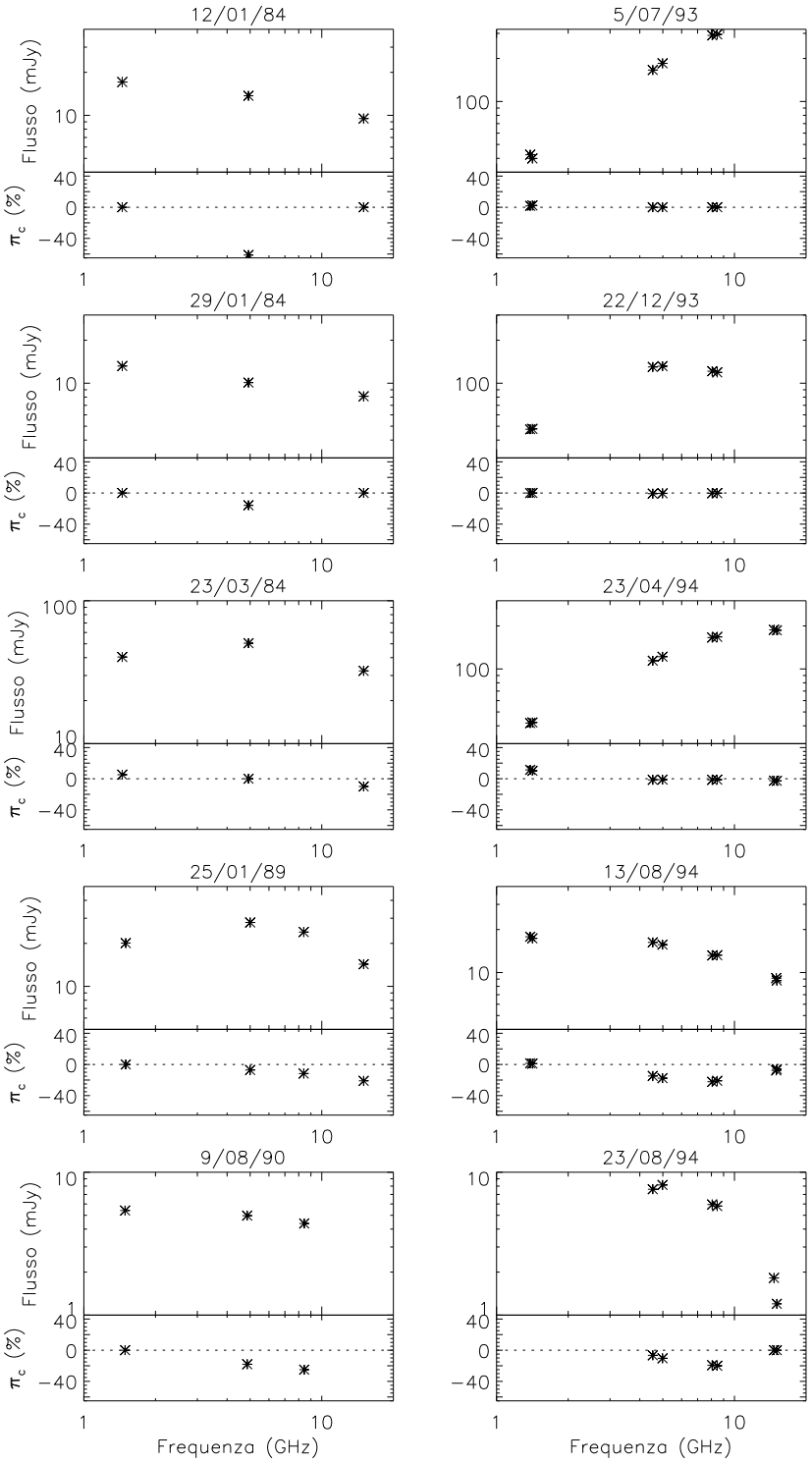

Fig. 5.7 Flux and polarization spectra as a function of frequency observed on UX Ari. Only observations with measurements of at least 3 frequencies are included. The date of the observation is given above every panel.

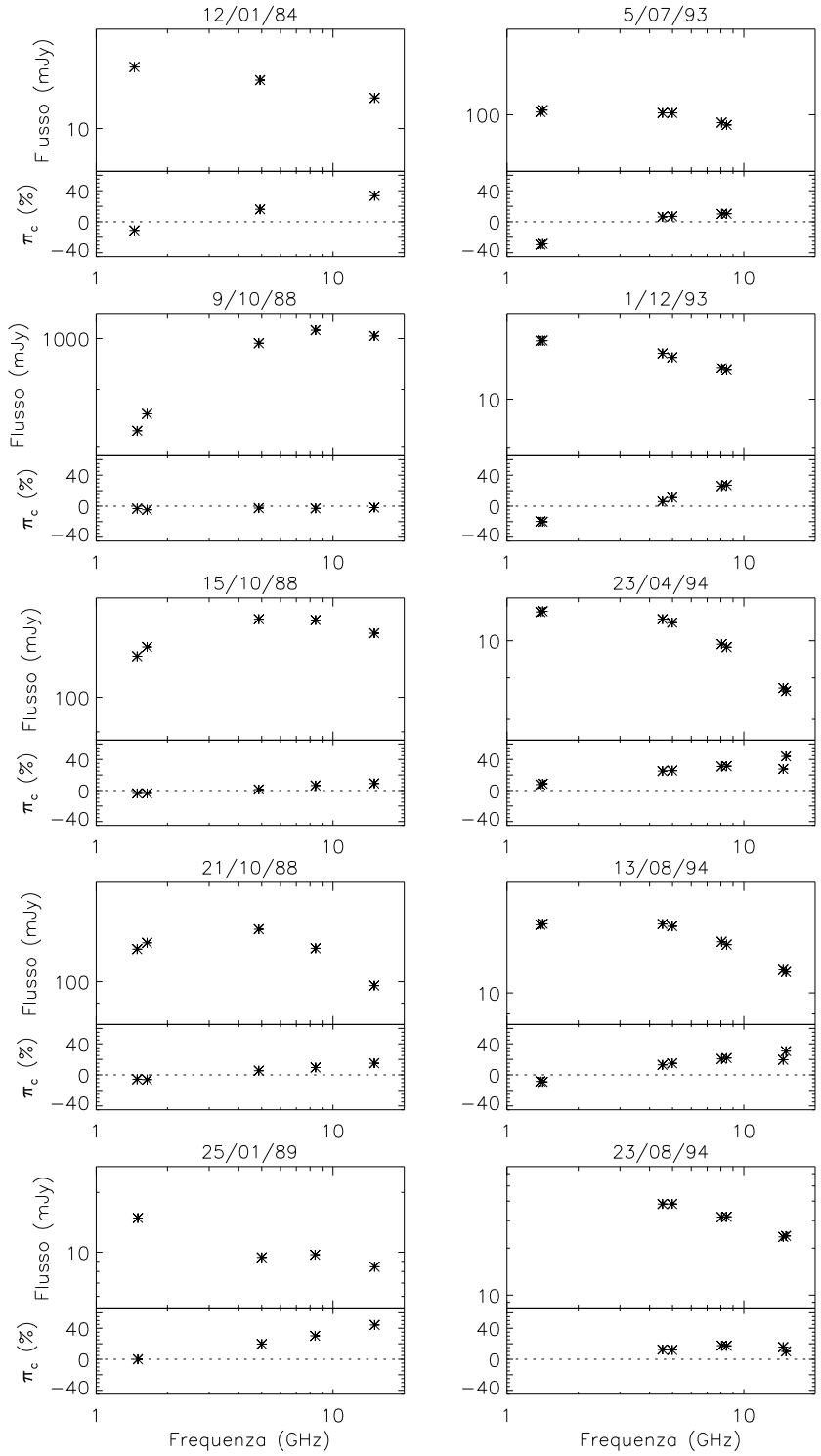

Fig. 5.8 Same as Fig. 5.7 in the case of HR 1099.

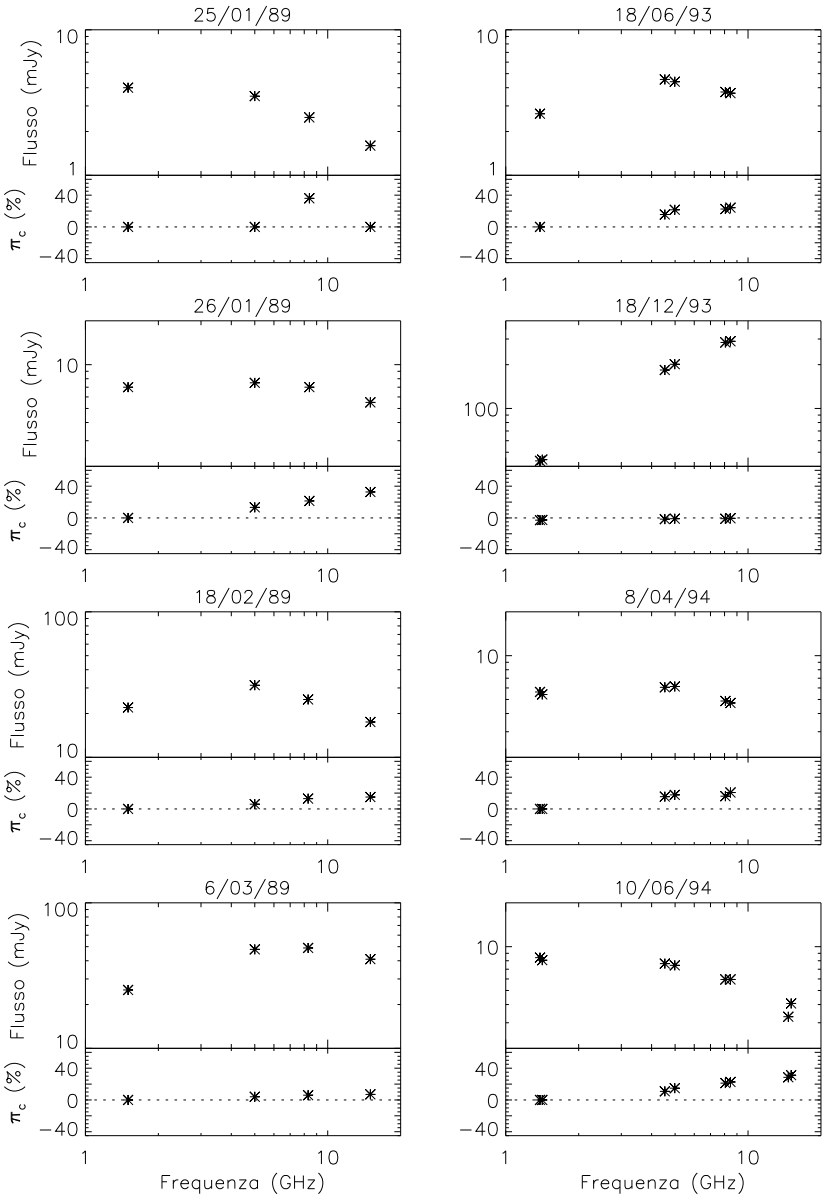

Fig. 5.9 Same as Fig. 5.7 in the case of HR 5110.

that generally the component with higher flux density at high frequency (R for HR 1099 and HR 5110, L for UX Ari) has a flatter spectrum, while the other one decreases faster with frequency. This behaviour is the opposite of what is predicted by gyrosynchrotron models: in fact where the source is optically thin, with $\alpha < 0$, we expect a decreasing degree of polarization with increasing frequency, because we obtain a flatter spectrum for the o-mode, but the emission

Tab. 5.1 Osservazioni dei sistemi UX Ari, HR 1099 e HR 5110 riportate nelle Fig. 5.7, 5.8 e 5.9

Data	Autori	Stelle osservate
1984	Pallavicini et al. 1985	UX Ari, HR 1099
1988	Su et al. 1993	HR 1099
25-26/1/89	White et al. 1990b	UX Ari, HR 1099, HR 5110
18/2-6/3/89	Umana et al. 1993	HR 5110
1990	Fox et al. 1994	UX Ari
1993-1994	White & Franciosini 1995	UX Ari, HR 1099, HR 5110

is polarized in the sense of the x-mode.

This problem of obtaining a degree of polarization which increases towards higher frequencies has not been addressed by most earlier published models, which generally have been concerned only with the explanation of the spectrum and of the polarization reversal at lower frequencies. Only Jones et al. (1994) have noted that they could not reproduce the behaviour of the degree of polarization at high frequencies. Inhomogeneous models can allow an increase of the polarization degree over a certain frequency range, but above a given frequency the source becomes optically thin everywhere, and gyrosynchrotron models then require that the degree of polarization decreases with increasing frequency. One can come up with ad hoc multi-component models which reproduce this behaviour: for example, the sum of an unpolarized steep spectrum component and a polarized, flatter-spectrum component can produce a degree of polarization which is increasing with frequency. However, even in this case, above some frequency the steep-spectrum component becomes insignificant and the degree of polarization should again decrease with increasing frequency. Our observations indicate that this does not generally occur below 15 GHz.

CONCLUSIONS

In this thesis we have considered some properties of the radio emission from RS CVn and Algol-type systems that have been observed recently during both active and quiescent periods, and we have developed quantitative models to interpret these characteristics.

As we have seen, radio observations performed in different periods indicate a possible evolution of the spectrum and of the source structure during flares, both during the initial phase, when the flux density increases for some hours, and during the following decay phase which typically lasts for a few days. These observations have been interpreted with a model which computes the time evolution of the energy distribution of relativistic electrons in a dipolar magnetic field: during the decay phase this evolution is determined by collision and synchrotron energy losses, while during the rise phase it is mainly due to the injection of new accelerated particles in the source, which contrasts the effect of losses.

The model results show that during the decay phase the spectrum changes its shape from an optically thick, autoabsorbed spectrum typical of flares to an optically thin, flat or decreasing spectrum, which is typical of the quiescent component: this result therefore confirms the hypothesis that the quiescent component represents the residual emission from a flare at the end of its decay. The model also reproduces very well other observed characteristics, in particular it explains the correlation between the low-frequency spectral index and the radio luminosity found by Mutel et al. (1987) and the variations of the source structure, observed with VLBI techniques, from the *core-halo* structure commonly seen at high flux density levels (Mutel et al. 1985; Lestrade et al.

1988) to the extended *halo* when the flux density is low (Massi et al. 1988). The predictions of the model indicate for the quiescent component a lifetime of a few days, in agreement with previous observations (Massi & Chiuderi Drago 1992); this lifetime is compatible with the frequency of flares deduced from monitoring programs performed at Effelsberg (Neidhöfer et al. 1993; Torricelli Ciamponi et al. 1995; Massi et al. 1996) and Noto (Umana et al. 1995), that show that medium-intensity flares ($\sim 50 - 150$ mJy) are frequent enough in these systems to mantain a quiescent level of emission.

During the rising phase, the increase of the flux density depends on the relative importance of the injection of new particles and of energy losses. The comparison with the spectra observed at Effelsberg (Torricelli Ciamponi et al. 1995) shows that our hypothesis of a constant injection rate does not allow us to reproduce the entire rising phase of the flare: in fact, for flares observed near the peak it is necessary to assume a low value of $Q_\circ$, since they are in a phase where the acceleration process is nearly over, while flares observed in the initial phase are reproduced by a higher injection rate. To better understand the rising phase, and therefore the acceleration mechanism, it is hence necessary to consider a time-variable injection rate. The model also predicts an increase in the source size, due to the increasing intensity of the radio emission in the outer parts as the density of relativistic electrons increases; this result is in good agreement with the VLBI observations performed by Trigilio et al. (1995).

Long-term observations of some systems have shown that the radiation emitted from the source can be strongly influenced by stellar rotation: in fact a compact source near the stellar surface, like those associated with the strongest flares, can be partly or completely occulted by the star during its rotation, and therefore the emission will show a strong modulation as a function of orbital phase. We have studied the effect of the modulation by computing the emission from an equatorial loop anchored on the star and rotating with it. We have shown that if the energy distribution of relativistic electrons is constant in time one obtains a periodic modulation which agrees with the one observed at low flux density levels; during strong activity periods however, when many flares are present, the light curves have narrower peaks, and it is therefore necessary

to take into account also the time evolution of the distribution. The model has been applied to the light curves observed on UX Ari in October 1992 (Elias et al. 1995) and on HR 1099 in February 1978 (Feldman et al. 1978), obtaining a good agreement with the observations.

Unfortunately, the study of the evolution of the emission during flares and of the modulation effect induced by stellar rotation is limited by the lack of spectral observations. In fact, although in the last years simultaneous observations of the radio emission at different frequencies have become available, the full evolution of a flare spectrum from its start to the end of the decay has not been studied yet. However, a series of spectral observations performed several times during a flare would give important informations on the acceleration mechanism and on the physical properties of the source. Moreover, long-term observations over several orbital periods would allow us to evidence spectral variations due to rotational modulation; the comparison with simultaneous optical observations would also allow us to derive the geometry of active regions and hence the structure of the magnetic fields present in the coronae of these stars. We have submitted a proposal to the VLA to observe some systems for 12 consecutive hours in order to follow the spectral evolution during flares; unfortunately during the two observations of HR 1099 performed so far the emission was at a quiescent level for the entire duration of the observation.

We have also studied the properties of the circular polarization observed in these systems. In particular, we have shown that the inversion in the sense of polarization of the quiescent component between 1.4 and 5 GHz is in contrast with gyrosynchrotron models. However recent VLA observations of these systems have shown the presence of a rapidly-varying component which is highly polarized in the opposite sense to the higher frequency emission and whose characteristics are compatible with coherent emission at the plasma frequency. This component also shows a slow modulation on timescales of a few minutes, and therefore, when the rapid fluctuations are not observable because they are too weak or unresolved due to longer integration times, it could be easily mistaken for gyrosynchrotron emission. We have proposed that this highly-polarized component is often present, although generally too weak to be distinguished from

the stronger but weakly-polarized quiescent component: the total polarization would then be dominated by that of the rapidly-varying component, explaining the observed inversion in the sense of polarization. We have proposed to observe a sample of RS CVn and Algol systems at 1.4 GHz, with the aim of determining whether this highly-polarized component is a common characteristics of these systems, and of studying whether it depends on the inclination of the stellar rotation axis.

The polarization observations have also evidenced a discrepancy between the predictions of gyrosynchrotron models and the behaviour of the polarization at high frequencies: we have in fact noted that it increases with frequency up to at least 15 GHz, well above the spectral peak. The gyrosynchrotron models predict that the degree of polarization should decrease above the frequency where the the source becomes completely optically thin; using ad-hoc inhomogeneous configurations it is however possible to obtain an increase of the polarization over a given frequency interval where the source is partly optically thick. We have proposed to perform VLA observations at high frequency, up to 43 GHz, in order to determine if and at which frequency the polarization reaches its peak value. The position of the polarization peak can give stringent indications on the magnetic structure of the source.

REFERENCES

Benz, A.O. (1993), *Plasma Astrophysics* (Kluwer, Dordrecht)

Benz, A.O., & Güdel, M. (1994), *A&A,* **285**, 621

Benz, A.O., Magun, A., Stehling, W., & Su, H. (1992), *Sol. Phys.,* **141**, 335

Bopp, B.W., & Talcott, J.C. (1978), *AJ,* **83**, 1517

Borghi, S., & Chiuderi Drago, F. (1985), *A&A,* **143**, 226

Brown, R.L., & Crane, P.C. (1978), *AJ,* **83**, 1504

Catalano, S. (1983), in *Activity in Red Dwarf Stars,* IAU Colloq. 71, ed. P.B. Byrne & M. Rodonò (Reidel, Dordrecht), p. 343

Chiuderi Drago, F., & Franciosini, E. (1993), *ApJ,* **410**, 301

Dempsey, R.C., Linsky, J.L., Schmitt, J.H.M.M., & Fleming, T.A. (1993), *ApJ,* **413**, 333

Donati, J.-F., Brown, S.F., Semel, M., Rees, D.E., Dempsey, R.C., Matthews, J.M., Henry, G.W., & Hall, D.S. (1992), *A&A,* **265**, 682

Donati, J.-F., Semel, M., Rees, D.E., Taylor, K., & Robinson, R.D. (1990), *A&A,* **232**, L1

Dorren, J.D., Siah, M.J., Guinan, E.F., & McCook, G.P. (1981), *AJ,* **86**, 572

Drake, J.J., Brown, A., Patterer, R.J., Vedder, P.W., Bowyer, S., & Guinan, E.F. (1995), *ApJ,* **421**, L43

Drake, S.A., Abbott, D.C., Bastian, T.S., Bieging, J.H., Churchwell, E., Dulk, G., & Linsky, J.L. (1987), *ApJ,* **322**, 902

Drake, S.A., Simon, T., & Linsky, J.L. (1989), *ApJS,* **71**, 905

Drake, S.A., Simon, T., & Linsky, J.L. (1992), *ApJS,* **82**, 311

Dulk, G.A. (1985), *ARA&A,* **23**, 169

Dulk, G.A., & Marsh, K.A. (1982), *ApJ,* **259**, 350

Elias, N.M. II, Quirrenbach, A., Witzel, A., Naundorf, C., Wegner, R., Guinan, E.F., & McCook, G.P. (1995), *ApJ,* **439**, 983

Feldman, P.A., Taylor, A.R., Gregory, P.C., Seaquist, E.R., Balonek, T.J., & Cohen, N.L. (1978), *AJ,* **83**, 1471

Fix, J.D., Claussen, M.J., & Doiron, D.J. (1980), *AJ,* **85**, 1238

Fox, D.C., Linsky, J.L., Veale, A., Dempsey, R.C., Brown, A., Neff, J.E., Pagano, I., Rodonò, M., Bromage, G.E., Kürster, M., & Schmitt, J.H.M.M. (1994), *A&A,* **284**, 91

Giampapa, M.S., Golub, L., & Worden, S.P. (1983), *ApJ,* **268**, L121

Gibson, D.M., Hicks, P.D., & Owen, F.N. (1978), *AJ,* **83**, 1495

Gondoin, P. (1986), *A&A,* **160**, 73

Gondoin, P., Giampapa, M.S., & Bookbinder, J.A. (1985), *ApJ,* **297**, 710

Güdel, M., & Benz, A.O. (1993), *ApJ,* **405**, L63

Guinan, E.F., & Giménez, A. (1993), in *The Realm of Interacting Binary Stars,* ed. J. Sahade et al. (Kluwer, Dordrecht), p. 51

Hall, D.S. (1976), in *Multiple Periodic Variable Stars,* IAU Colloq. 29, ed. W.S. Fitch (Reidel, Dordrecht), p. 287

Hall, D.S. (1989), *Space Scie. Rev.,* **50**, 219

Huenemorder, D.P., Ramsey, L.W., & Busazi, D.L. (1990), *ApJ,* **350**, 763

Jones, K.L., Stewart, R.T., Nelson, G.J., & Duncan, A.R. (1994), *MNRAS,* **269**, 1145

Kai, K., Melrose, D.B., & Suzuki, S. (1985), in *Solar Radiophysics,* ed. D.J. McLean & N.R. Labrum (Cambridge Univ. Press, Cambridge), p. 415

Klein, K.-L. (1987), *A&A,* **183**, 341

Klein, K.-L., & Chiuderi Drago, F. (1987), *A&A,* **175**, 179

Kuijpers, J., & van der Hulst, J.M. (1985), *A&A,* **149**, 343

Lefèvre, E., Klein, K.-L., & Lestrade, J.-F. (1994), *A&A,* **283**, 483

Lestrade, J.-F., Mutel, R.L., Phillips, R.B., Webber, J.C., Niell, A.E., & Preston, R.A. (1984a), *ApJ,* **282**, L23

Lestrade, J.-F., Mutel, R.L., Preston, R.A., & Phillips, R.B. (1988), *ApJ,* **328**, 232

Lestrade, J.-F., Mutel, R.L., Preston, R.A., Scheid, J.A., & Phillips, R.B.

(1984b), *ApJ,* **279**, 184

Lim, J., Nelson, G.J., Castro, C., Kilkenny, D., & van Wyk, F. (1992), *ApJ,* **388**, L27

Lim, J., White, S.M., Nelson, G.J., & Benz, A.O. (1994), *ApJ,* **430**, 332

Linsky, J.L. (1984), in *Cool Stars, Stellar Systems and the Sun: 3rd Cambridge Workshop,* ed. S.L. Baliunas & L. Hartmann (Springer, Berlin), p. 244

Little-Marenin, I.R., Simon, T., Ayres, T.R., Cohen, N.L., Feldman, P.A., Linsky, J.L., Little, S.J., & Lyons, R. (1986), *ApJ,* **303**, 780

Massi, M., & Chiuderi Drago, F. (1992), *A&A,* **253**, 403

Massi, M., Felli, M., Pallavicini, R., Tofani, G., Palagi, F., & Catarzi, M. (1988), *A&A,* **197**, 200

Massi, M., Neidhöfer, J., Torricelli Ciamponi, G., & Chiuderi Drago, F. (1996), in *Radio Emission from the Stars and the Sun,* in press

Melrose, D.B. (1980), *Plasma Astrophysics, Vol. 2* (Gordon & Breach, New York)

Melrose, D.B. (1991), *ARA&A,* **29**, 31

Melrose, D.B., & Brown, F.C. (1976), *MNRAS,* **176**, 15

Melrose, D.B., & Dulk, G.A. (1988), *Sol. Phys.,* **116**, 141

Morris, D.H., Mutel, R.L., & Su, B. (1990), *ApJ,* **362**, 299

Mutel, R.L., Doiron, D.J., Lestrade, J.-F., & Phillips, R.B. (1984), *ApJ,* **278**, 220

Mutel, R.L., Lestrade, J.-F., Preston, R.A., & Phillips, R.B. (1985), *ApJ,* **289**, 262

Mutel, R.L., & Morris, D.H. (1988), in *Activity in Cool Star Envelopes,* ed. O. Havnes et al. (Kluwer, Dordrecht), p. 283

Mutel, R.L., Morris, D.H., Doiron, D.J., & Lestrade, J.-F. (1987), *AJ,* **93**, 1220

Mutel, R.L., & Weisberg, J.M. (1978), *AJ,* **83**, 1499

Neidhöfer, J., Massi, M., & Chiuderi Drago, F. (1993), *A&A,* **278**, L51

Owen, F.N., Jones, T.W., & Gibson, D.M. (1976), *ApJ,* **210**, L27

Pacholczyk, A.G. (1970), *Radio Astrophysics* (Freeman, San Francisco)

Pallavicini, R. (1995), in *Flares and Flashes,* IAU Colloq. 151, ed. J. Greiner et al. (Springer, Berlin), p. 148

Pallavicini, R., Willson, R.F., & Lang, K.R. (1985), *A&A,* **149**, 95

Petrosian, V. (1981), *ApJ,* **251**, 727

Petrosian, V. (1985), *ApJ,* **299**, 987

Popper, D.M., & Ulrich, R.K. (1977), *ApJ,* **212**, L131

Ramaty, R. (1969), *ApJ,* **158**, 753

Richards, M.T. (1990), in *Cool Stars, Stellar Systems and the Sun: 6th Cambridge Workshop,* ed. G. Wallerstein (ASP, San Francisco), p. 221

Rodonò, M., Byrne, P.B., Neff, J.E., Linsky, J.L., Simon, T., Butler, C.J., Catalano, S., Cutispoto, G., Doyle, J.G., Andrews, A.D., & Gibson, D.M. (1987), *A&A,* **176**, 267

Rodonò, M., Cutispoto, G., Pazzani, V., Catalano, S., Byrne, P.B., Doyle, J.G., Butler, C.J., Andrews, A.D., Blanco, C., Marilli, E., Linsky, J.L., Scaltriti, F., Busso, M., Cellino, A., Hopkins, J.L., Okazaki, A., Hayashi, S.S., Zeilik, M., Helston, R., Henson, G., Smith, P., & Simon, T. (1986), *A&A,* **165**, 135

Rodonò, M., Lanza, A.F., & Catalano, S. (1995), *A&A,* **301**, 75

Simon, T., Fekel, F.C. Jr, & Gibson, D.M. (1985), *ApJ,* **295**, 153

Simon, T., Linsky, J.L., & Schiffer, F.H. (1980), *ApJ,* **239**, 911

Spitzer, L. (1962), *Physics of Fully Ionized Gases* (Wiley, New York)

Strassmeier, K.G., Rice, J.B., Wehlau, W.H., Vogt, S.S., Hatzes, A.P., Tuominen, I., Piskunov, N.E., Hackman, T., & Poutanen, M. (1991), *A&A,* **247**, 130

Su, B., Mutel, R.L., Li, Y., & Zhang, H. (1993), *Ap. and Sp. Scie.,* **200**, 211

Swank, J.H., White, N.E., Holt, S.S., & Becker, R.H. (1981), *ApJ,* **246**, 208

Torricelli Ciamponi, G., Neidhöfer, J., Massi, M., & Chiuderi Drago, F. (1995), in *Flares and Flashes,* IAU Colloq. 151, ed. J. Greiner et al. (Springer, Berlin), p. 42

Trigilio, C., Leto, P., & Umana, G. (1996), in *Radio Emission from the Stars and the Sun,* in press

Trigilio, C., Umana, G., & Migenes, V. (1993), *MNRAS,* **260**, 903

Trigilio, C., Umana, G., & Migenes, V. (1995), in *Flares and Flashes,* IAU Colloq. 151, ed. J. Greiner et al. (Springer, Berlin), p. 36

Uchida, Y., & Sakurai, T. (1983), in *Activity in Red Dwarf Stars,* IAU Colloq. 71, ed. P.B. Byrne, & M. Rodonò (Reidel, Dordrecht), p. 629

Umana, G., Trigilio, C., Hjellming, R.M., Catalano, S., & Rodonò, M. (1993), *A&A,* **267**, 126

Umana, G., Trigilio, C., Tumino, M., Catalano, S., & Rodonò, M. (1995), *A&A,* **298**, 143

van den Oord, G.H.J, & de Bruyn, A.G. (1994), *A&A,* **286**, 181

Vogt, S.S. (1983), in *Activity in Red Dwarf Stars,* IAU Colloq. 71, ed. P.B. Byrne & M. Rodonò (Reidel, Dordrecht), p. 137

Vogt, S.S., & Hatzes, A.P. (1991), in *The Sun and Cool Stars: Activity, Magnetism, Dynamos,* IAU Colloq. 130, ed. Tuominen et al. (Springer, Berlin), p. 297

Vogt, S.S., & Penrod, G.D. (1983), *PASP,* **95**, 565

Welty, A.D., & Ramsey, L.W. (1995), *AJ,* **109**, 2187

White, N.E., Shafer, R.A., Horne, K., Parmar, A.N., & Culhane, J.L. (1990a), *ApJ,* **350**, 776

White, S.M. (1996), in preparazione

White, S.M., & Franciosini, E. (1995), *ApJ,* **444**, 342

White, S.M., Kundu, M.R., & Jackson, P.D. (1989), *A&A,* **225**, 112

White, S.M., Kundu, M.R., Uchida, Y., & Nitta, N. (1990b), in *Cool Stars, Stellar Systems and the Sun: 6th Cambridge Workshop,* ed. G. Wallerstein (ASP, San Francisco), p. 239

Willson, R.F., & Lang, K.R. (1987), *ApJ,* **312**, 278

APPENDIX

PUBLICATIONS

§ A.1 Papers published on refereed journals

Chiuderi Drago, F., & Franciosini, E. (1993), **Flaring and quiescent radio emission of UX Arietis: a time-dependent model**, *Astroph. J.*, **410**, 301

Franciosini, E., & Chiuderi Drago, F. (1995), **Radio and X-ray emission in stellar magnetic loops**, *Astron. & Astroph.*, **297**, 535

White, S.M., & Franciosini, E. (1995), **Circular polarization in the radio emission of RS Canum Venaticorum binaries**, *Astroph. J.*, **444**, 342

§ A.2 Presentations at international meetings

Chiuderi Drago, F., & Franciosini, E. (1993), **Radio and X-ray luminosity of RS CVn binary systems**, in *Physics of Solar and Stellar Coronae*, ed. J.F. Linsky and S. Serio (Kluwer, Dordrecht), p. 405

Franciosini, E. (1993), **Flaring and quiescent radio emission of RS CVn stars**, *Mem. Soc. Astron. It.*, **64**, 688

Franciosini, E., & Chiuderi Drago, F. (1993), **Radio emission from stellar active regions**, in *International Summer School on Space Plasma Physics*, Russia May 31 – June 11, 1993, in press

Franciosini, E. (1993), **Time evolution of an ensemble of relativistic electrons in a non homogeneous atmosphere**, in *International Summer School on Space Plasma Physics*, Russia May 31 – June 11, 1993, in press

Chiuderi Drago, F., & Franciosini, E. (1993), **Time evolution of the radio emission in a stellar active region**, in *Magnétisme dans les Étoiles de Type Solaire*, Réunion Biennale CNRS, Paris, November 8 – 10, 1993, p. 174

Franciosini, E., & White, S.M. (1995), **Coherent radio bursts from RS CVn binaries**, in *Flares and Flashes*, IAU Colloq. 151, ed. J. Greiner et al. (Springer, Berlin), p. 40

Franciosini, E., & Chiuderi Drago, F. (1995), **Radio and X-ray emission in stellar magnetic loops**, in *Magnetodynamic Phenomena in the Solar Atmosphere - Prototypes of Stellar Magnetic Activity*, IAU Colloq. 153, in press

Franciosini, E., & Chiuderi Drago, F. (1995), **Rotational modulation of the radio emission from active stars**, in *Radio emission from the stars and the sun*, Barcelona July 3 – 7, 1995, in press

Torricelli Ciamponi, G., Franciosini, E., Massi, M., & Neidhöfer, J. (1995), **Rising phase in UX Arietis radio flares**, in *Radio emission from the stars and the sun*, Barcelona July 3 – 7, 1995, in press

Franciosini, E. (1995), **Interpretation of the October 1992 radio light curve of UX Ari**, in *Cool Stars, Stellar Systems, and the Sun: 9th Cambridge Workshop*, Florence October 3 – 6, 1995, in press